ANGLE SENSITIVE PIXELS FOR INTEGRATED LIGHT FIELD SENSING

A Dissertation

Presented to the Faculty of the Graduate School

of Cornell University

in Partial Fulfillment of the Requirements for the Degree of

Doctor of Philosophy

by

Albert Wang

May 2012

ABSTRACT

Albert Wang, Ph.D.

Cornell University 2012

Angle-sensitive pixels are micro-scale devices which capture information about both the intensity and incident angle of the light they see. Using pairs of local diffraction gratings above a photodiode, these pixels employ the Talbot effect to detect incident angle. The gratings are implemented with the metal interconnect layers of CMOS manufacturing technology and therefore require no post-processing or external optics. Altering layout geometries for different angle-sensitive pixels generates a distinct angular response with a characteristic frequency and orientation. To function effectively, image sensors need to employ a diverse set of angle-sensitive pixels whose responses, taken together, forms a complete basis similar to a non-separable low-order 2D Hartley transform of local incident angle. As 2D frequency-domain transforms play an important role in image processing, these devices are useful for a variety of imaging tasks. This thesis demonstrates several CMOS image sensors utilizing these devices to perform different functions, such as lensless 3D object localization, single-shot light-field capture, and optoelectronic image compression. The algorithms used for these tasks are simple and take advantage of the transform-based nature of angle-sensitive pixel based image capture.

BIOGRAPHICAL SKETCH

The author received his B.A. in chemistry and physics from Harvard University in 2005. After spending two years away from his studies, he began his graduate work in electrical engineering at Cornell in 2007.

This thesis is dedicated to my father, who introduced me to engineering.

ACKNOWLEDGEMENTS

The author would like to acknowledge the support and contributions of his thesis advisor, Prof. Alyosha Molnar, over the course of this project and the advice and suggestions of special committee members Prof. Alyssa Apsel and Prof. Chris Schaffer. Additionally, the author is grateful for the helpful consultations with Prof. Sheila Hemami and Prof. Clif Pollock, as well as the comments of Weiyu Xu, Meng Wang and Prof. A. Kevin Tang on the in-crowd algorithm. Finally, the author would like to thank the NIH and DARPA for funding this research.

TABLE OF CONTENTS

LIST OF TABLES

LIST OF FIGURES

Chapter 1
Introduction

1.1 Overview

This thesis charts the development of optoelectronic imaging systems which acquire and process incident angle information for imaging tasks in 2D and 3D space. The "angle-sensitive pixel" device responsible for measuring angle has been integrated with conventional mixed-signal circuits in standalone CMOS chips. These chips encode both local light brightness and direction of arrival in an image format which is suitable for efficient processing and does not need controlled illumination conditions. The captured images have been used in a wide variety of tasks such as the generation of 3D range maps, object localization, and motion measurement. As a result, this work provides a framework for expanding the capabilities of digital imaging at no additional cost or complexity.

The design and analysis of this imaging system for incident angle draws on three distinct concepts: the "light field", frequency domain image processing, and CMOS sensor/circuit integration. First, the "light field" provides a mathematical framework for analyzing the light reflected from an arbitrary 3D visual scene, and identifies incident angle information as a necessary component of a complete characterization of this reflected light. Second, frequency-domain image processing techniques enable computationally efficient characterization and discrimination of visual scene features. Finally, the CMOS manufacturing platform provides a well-developed, mature manufacturing technology to design incident angle sensors which are small, cheap, and reliable silicon chips.

1.1.1 The light field

To design an image sensor suitable for both 2D and 3D imaging tasks, understanding the signals generated by a typical scene composed of 3D objects is critical. In 1939, Gershun developed the theory of the *light field* [1] to predict illumination patterns on surfaces in response to different lighting conditions. He characterized the light field as a vector field in 3D space, describing the light arriving at a given point (x, y, z) with an infinite set of vectors. Each vector has a direction in two solid angles θ and ϕ, corresponding to the direction of light arriving at (x, y, z) from a given point in the illuminating source, and a magnitude L representing the brightness of arriving light.

A more recent formulation of the concept of the light field reparameterizes the distribution of light rays in 3D space as a scalar-valued 5-dimensional function, known as the plenoptic function [2]. This function was developed as a framework to analyze problems relating to the imaging, rather than illumination, of 3D visual scenes, and represents the light arriving from the scene with direction (θ, ϕ) to an observer located at a point (x, y, z) with an intensity $L(x, y, z, \theta, \phi)$. Complete description of this function therefore encodes all possible views of the scene from any observing location.

For most imaging problems, however, a complete representation of the plenoptic function is usually not necessary. Full knowledge of $L(x, y, z, \theta, \phi)$ generated by a visual scene would, for example, include knowledge of how the scene would appear to an observer behind occluding objects and inside completely enclosed surfaces, as no restrictions are placed on observer location. This knowledge equates to *true* 3D imaging, but the conventional concept of "3D" imaging does not include the ability to see through walls and around corners. Furthermore, the complete measurement of the plenoptic function requires an observer to determine the intensity of every

light ray generated from every point on a visual scene, at every point in space. For any practical scene with complexity, this is an impossible task.

Making reasonable assumptions on observer location for typical imaging problems reduces the difficulty of this general imaging problem. If the observer is restricted to a position in space sufficiently far from the visual scene, such that no objects in the scene or in intervening space affect the passage of light rays, the plenoptic function is actually a 4-dimensional function, $L(x, y, \theta, \phi)$. This dimensionality reduction is a consequence of the linear propagation of light rays in empty space, in the absence of occlusions and obstructions. With knowledge of the full plenoptic function $L(x, y, \theta, \phi)$ for some z coordinate z_0, the value of $L(x, y, \theta, \phi)$ for an arbitrary z can be determined with simple linear projection. This 4D representation of a visual scene is also known as the *photic field* [3], the *4D light field* [4], or the *Lumigraph* [5].

With this complete 4D representation of a visual scene, an observer can synthetically render an accurate view of the original scene as seen from any point in space which satisfies the "no occlusion" assumption [4,5]. Consequently, capturing the 4D light field is the fundamental problem posed in imaging a 3D scene, and the data recovered by an image sensor which extracts a full representation of the 4D light field enables the reconstruction of the original scene after capture. While a complete characterization of even this continuous 4D plenoptic function remains impossible, sampling the distribution of light rays provides sufficient information to provide a good approximation.

A conventional image sensor provides a 2D sampling of this 4D plenoptic function, in the form of a 2D array of data values which describe the intensity of light incident on each pixel in the sensor array. As this conventional sensor does not discriminate between rays arriving with different angles of incidence θ_1 and θ_2 or

ϕ_1 and ϕ_2, the samples acquired by each pixel have integrated out the two angular dimensions. Proper recovery and reconstruction of a visual scene thus is dependent on an image sensor which captures both spatial and angular variation in light brightness.

1.1.2 Frequency domain image processing

Although the pixels of a digital image sensor provide an image as 2D array of data values, subsequent image processing rarely uses the image directly as acquired. Typically, a 2D transform such as the Fast Fourier Transform (FFT) or Discrete Cosine Transform (DCT) is applied to the image to generate a frequency domain representation of the image. Downstream processing then can take advantage of transform properties when performing tasks such as edge detection [6], motion estimation [7], and data compression [8].

The problem of image registration provides a good illustration of the power inherent to transform-based image processing. Given a set of images for a particular visual scene taken from different viewpoints, image registration is the process of aligning these images to a single viewpoint. To determine the shift between two images in the set, one possible approach is to search for the maximum correlation between the two images over the space of image offsets in the xy image plane. For two images that are $N \times N$ in size, the total computations required to search the possible positions is $O(N^4)$.

An alternative approach to the same problem relies on the well-known shift property of the Fourier transform, where a position shift in a 2D image corresponds to a phase rotation in the transformed image in the frequency domain [9]. To determine the position offset between two images with the shift property, both images are first translated to the Fourier domain. Matrix multiplication between

the two transformed images extracts the phase shift, and thus the spatial distance between the two images. With efficient Fourier transform computation and matrix multiplication algorithms [10], the required computation is less than $O(N^3)$, a significant savings over the correlation matching approach.

An additional important feature of frequency domain image transforms is their ability to concentrate image information in a few strong coefficients [11]. An image with N^2 pixel values frequently has only M significant coefficients in the transform domain, where $M \ll N^2$, and this *energy compaction* property proves extremely useful for image compression and noise reduction [12]. For compression, only the M transform coefficients of an image must be stored to provide an accurate representation of the original image, as the other, unspecified coefficients can be assumed to be zero. In noise reduction, only the M transform coefficients contain relevant image signal power, while the other coefficients are simply contaminated with additive noise and can be discarded to improve the image signal-to-noise power ratio on image reconstruction.

Frequency domain spectral processing therefore is a powerful, efficient approach to image processing problems, but most imaging systems today directly capture a 2D image array and rely on subsequent digital hardware and software to perform the transform calculations. Ideally, an image sensor is aware of these downstream operations and captures images directly in a suitable format to conserve computational resources. Although sensor chips which integrate image transform computations have been demonstrated [13–15], integrating this processing with incident angle sensitivity poses a unique challenge.

1.1.3 CMOS image sensors

The development of the first commercially viable digital image sensors began with work at Bell Labs on semiconductor charge-coupled devices (CCDs) [16]. Although the CCD was initially intended as a memory device, researchers quickly realized that they also were effective at detecting free charge carriers generated by photons striking the wafer substrates [17]. The charge transfer principle at the heart of the CCD was quickly adopted for solid-state image sensor arrays, and Eastman-Kodak demonstrated the first digital camera using such an device in 1973. The addition of color filters to the CCD array [18] subsequently enabled color photographs and established the basis for today's ubiquitous digital cameras.

Work on *active* pixel sensors incorporating on-chip amplification and buffering in complementary metal-oxide semiconductor (CMOS) manufacturing processes predates the charge-coupled device. As a result of their low On-resistance, coupled with high Off-resistance and zero gate current, MOS transistors are ideal detection and interface devices for manipulating photo-generated charge from phototransistor [19] and photodiode detectors [20, 21]. Although the passive charge detectors used in CCDs have superior performance to the active photodiodes of CMOS pixel arrays, the benefits of system design flexibility, low cost, and high readout speed, have made CMOS the dominant image sensor technology today.

Image sensors have seen significant advances in the quest for further improvement since their invention. Optical components such as microlenses [22, 23] have been integrated to increase effective optical fill factor otherwise lost to routing lanes and pixel control switches and to improve sensitivity. Imaging system complexity has also exploded with the inclusion of on-chip buffer amplifiers and correlated-double sampling for offset correction with [24, 25] and analog-to-digital converters [26, 27] to enable true camera-on-a-chip integrated systems.

With the backing of 50 years of continued development, CMOS image sensor technology provides a powerful, robust optoelectronic manufacturing platform for new sensing devices. In particular, the precision lithography of modern CMOS manufacturing processes and submicron geometry scaling provide opportunities to provide new functionality to image sensors through the capture of incident angle information.

1.2 Organization of this text

Section 2, drawn from [28], describes the physical structure of the angle-sensitive pixel, a pixel-scale device manufactured in CMOS and possessing sensitivity to the angle and intensity of incident light. The following two sections, from [29] and [30], demonstrate using small arrays of these pixels to perform lensless 3D localization of luminous objects and an algorithm devised to accelerate the localization task by over a factor of 10 compared to existing methods without sacrificing accuracy. Section 5, from [31], explores the implications of a complete, integrated CMOS light-field image sensor composed of angle-sensitive pixels, showing that single captured images can be directly used for computational refocus and 3D depth mapping. The next section, taken from [32], illustrates how the same image sensor, with different back-end processing, functions as a sensor for object motion. Finally, the last two sections provide a theoretical framework [33] for understanding angle-sensitive pixels as angular bandpass filters with characteristic center frequencies and a second image sensor which uses these pixel-based bandpass filters to perform image compression in the *optical* domain.

Chapter 2
Angle sensitivity and the Talbot effect

2.1 Introduction

Conventional imaging uses a large array of light sensors to create a map of light intensity at an image plane. However, this intensity map fails to capture incident angle, polarization angle, and other properties of light rays passing through the image plane. A complete description of these additional parameters defines the light field [1, 3], or flow of light, at the image plane. Applications of light fields include 3D rendering [4] and computational refocus of images [34].

We present a method of measuring the light field at a given image plane. In contrast to a conventional solid state image sensor with sites sensitive only to light intensity, our image sensor has sites which are sensitive to both the intensity and the incident angle of light striking them. Our technique exploits Fresnel diffraction patterns of periodic gratings (the Talbot effect [35]), to characterize incident light by its magnitude and direction. Specifically, we employ local, micron-scale diffraction gratings at each of a large number of sensor sites to capture this information. To distinguish these devices from the typical pixels of digital image sensors, we call them angle-sensitive pixels (ASPs).

In the following two sections, we provide background information on light fields and the Talbot effect. We then present the design principles of the angle-sensitive pixel followed by experimental results from prototypes of small light-field image sensors composed of our ASPs. Finally, we discuss implications and future directions for this work.

2.2 The light field

In an 1846 lecture, Michael Faraday first proposed the concept of light as a field [36]. This concept was expanded by Gershun, who developed the theory of a "light field" in three-dimensional space [1]. At a given point, the light field is defined by the infinite collection of vectors which represent the light arriving at the point from all angles. The light field can be formally defined by a "plenoptic function" [2] of multiple variables. The plenoptic function parameterizes the light rays passing through all space in terms of intensity, I, which is dependent on position in space (x, y, and z), direction (θ, ϕ), wavelength (λ), time (t), and polarization angle (ψ). Hence, $I(x, y, z, \theta, \phi, \lambda, t, \psi)$ is the complete representation of a visual scene and contains all possible views of the scene.

Measuring the plenoptic function would require an observer able to determine the intensity of every ray, for every wavelength and polarization, at all instants in time and at every point in space. Clearly, perfect determination of the plenoptic function for any practical scene is impossible. However, a number of techniques, collectively known as light-field imaging, have been devised which let us record aspects of the plenoptic function beyond simple intensity at a plane. The simplest method is to use an array of pinhole cameras, as proposed by Adelson and Wang [37], where each camera captures the incident angle-dependent intensity I(θ, ϕ) at a particular location, (x_0, y_0). Cameras at different positions (x_i, y_i) capture a slice of the plenoptic function, $I(x, y, \theta, \phi)$. Arrays of conventional cameras can also be used [38, 39], as can camera scanning [40] or multiple masks [41]. Small-scale solutions have used micro-lenses to emulate camera arrays [37, 42]. However, all of these approaches require a significant number of parallel or moveable optical components to capture information about the light field beyond a simple intensity map.

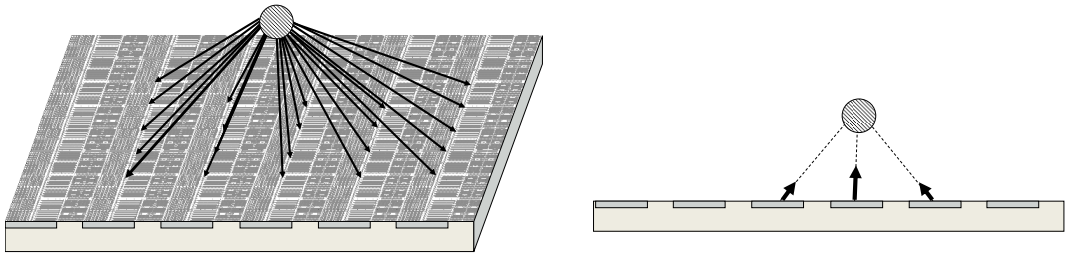

(a) (b)

Figure 2.1: Example of light-field imaging: (a) Light from a source strikes each pixel of an array with a distinct incident angle. (b) If each pixel in an array can determine the incident angle as well as the intensity of the light it detects, then array is able to localize a light source in three dimensions.

Recording information about the light field of a scene provides a more complete description of that scene than a conventional photograph or movie, and is useful for a number of applications. The light field allows prediction of illumination patterns on a surface given known sources and the three-dimensional reconstruction of scenes (light-field rendering [4] or three-dimensional shape approximation [5]). Figure 2.1 shows how one aspect of the light field, incident angle, can be used to localize a light source in three-dimensional space. Capturing the light field also permits construction of images with an arbitrary focal plane and aperture [34, 40]. This capability is useful in both photography and in microscopy for obtaining multiple focal planes without moving any optics [43].

As schematically shown in Fig. 2.1, we present a method to perform light-field imaging by directly measuring incident intensity and angle of light. Using a large number of pixels, each containing a micron-scale diffraction grating, our sensor directly measures light vector information at many distinct points in space. In contrast to other approaches which require multiple lenses and/or moving parts, our device is monolithic, requires no optical components aside from the sensor itself and can be manufactured in a standard planar microfabrication process. The key

to our approach is to exploit the Talbot effect.

2.3 The Talbot effect

The Talbot effect, or the self-imaging property of periodic objects such as diffraction gratings, was first discovered by Henry Fox Talbot in 1836 [35]. When an infinite diffraction grating (shown in Fig. 2.2(a)) is illuminated by a plane wave normal to its surface, identical images of the grating are formed at certain equally spaced distances behind the grating as in Fig. 2.2(b). Lord Raleigh explained this effect as a consequence of Fresnel diffraction [44], and showed that the images form at integer multiples of the Talbot distance $z_t = 2d^2/\lambda$. where d is the period of the grating and is the wavelength of incident light. Subsequent work showed that additional, more complex sub-images can be observed at the fractional Talbot distances $z = (m/n)z_t$, where m and n are positive integers [45–47].

The Talbot effect is exploited in a wide variety of macro-scale applications. The basic self-imaging phenomenon has been used in interferometry [48], image processing [49], and coherent array illumination [50]. It has also been used to measure wavefront distortion introduced by optical elements [51, 52]. Others have applied the Talbot effect to perform ranging and depth measurement [53–55].

Existing depth estimation work employing the Talbot effect relies on direct characterization of the response of the Talbot self-images to different depths. Early work measuring the contrast of self images reflecting from an object was limited to range measurements within a single Talbot distance [51]. Later research with modulated gratings enabled greater depth measurement [52]. A more recent technique uses a lens to focus light from a scene in front of a diffraction grating [55]. In this arrangement, the convergent Talbot effect results in self-images of the grating at all depths behind the grating. The line width of the self-images observed in a

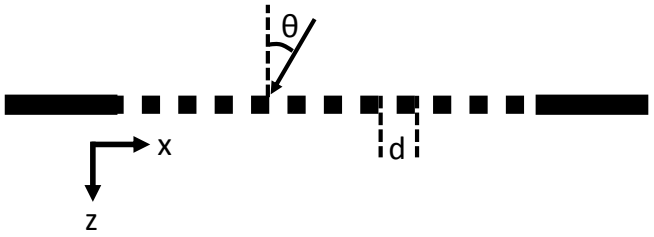

(a)

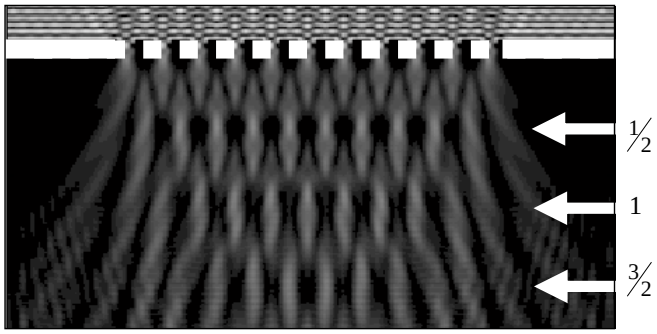

(b)

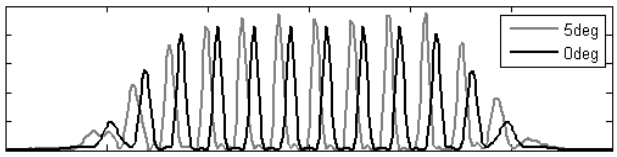

(c)

Figure 2.2: Illustration of self imaging property of nanoscale diffraction gratings. (a) Definition of scale and dimensions. b) FDTD simulations of the Talbot effect at the nanoscale: d = 800nm, $\lambda = 375$nm in SiO_2 (equivalent to 525nm in vacuum), $\theta = 0$. Note self-images at multiples of the half Talbot depth. (c) FDTD simulation showing lateral shift of the self image at the half Talbot depth with shifting incident angle from $\theta = 0°$to $5°$.

particular area determines the depth of the corresponding region in the scene.

While the previously described depth mapping techniques are capable of recovering information from the light field, they do so at a macroscopic scale. A monolithic light field image sensor based on these methods requires the integration of the dedicated optics with a conventional image sensor. Moreover, significant computation is required to translate the imaged Talbot patterns into light field information. For the light field imaging technique we propose here, we do not rely on direct imaging and characterization of the Talbot self-images.

Instead, our light field image sensor indirectly extracts 3D structure information by taking advantage of the sensitivity of the Talbot effect to incident angle. This sensitivity is known as the off-axis Talbot effect. This sensitivity is known as the off-axis Talbot effect. Existing work has shown that for macroscopic ($d \gg \lambda$) linear gratings illuminated by an off-axis plane wave incident at angle θ, self-imaging is observed at multiples of the distance $z = 2\cos^3(\theta)d^2/\lambda$ [56]. Furthermore, the images exhibit a lateral shift $\Delta x = z\tan(\theta)$ perpendicular to the grating lines as a result of the off-axis wave propagation.

Multiple sources of off-axis illumination each generate their own set of laterally shifted grating self-images, and these self-images superpose. For small angles, these self-images all form at approximately the same distances, and the superimposed image informs us about the magnitude of illumination as well as direction. Hence, measuring the shift in Talbot self-images of a grating lets us recover the incident angles of light rays striking the grating.

Since diffraction gratings are easily manufactured using standard planar microfabrication techniques, we can construct a micron-scale, easily tiled structure which contains a grating and measures shifts in the resultant self-images. An array of such structures provides many simultaneous measurements at many adjacent

points creating a map of incident angle at the plane of the array. Such an array would be a stand-alone light-field image sensor.

2.4 Design

The proposed micron-scale sensor requires both a diffraction grating to generate Talbot self-images and a means of analyzing these self-images. In order to achieve spatial resolution comparable with existing image sensors, the entire sensor structure must fit within an area at most tens of microns on a side. To produce a reasonably periodic self-image, the grating must have several periods within this area. Together these two constraints restrict us to gratings with a period of only a few wavelengths. Contemporary planar photolithography techniques can easily achieve the resolution required to generate appropriate diffraction gratings. As with previous work [57], we have relied on numerical modeling and simulation to accurately predict behavior for finite gratings built on a single-micron scale.

The Talbot effect has been observed empirically for high-density gratings with a period of approximately 3λ [58]. Recent numerical treatments show that as long as the period is greater than the wavelength of incident light, Talbot-like self-images can be observed in close proximity to the diffraction grating [57]. We have performed our own simulations using the finite-difference time domain (FDTD) technique and observed similar patterns, as shown in Fig. 2.2(b) and 2.2(c). In particular, starting from the half Talbot distance, we observe strong intensity patterns with periodicity identical to the diffraction grating. Furthermore, additional simulations show that under off-axis illumination, the intensity patterns generated by high-density gratings shift laterally. This behavior is identical to the behavior of Talbot self-images generated by conventional, macroscale diffraction gratings. The primary effect of moving to wavelength-scale diffraction gratings is to suppress

higher-order fractional Talbot images.

To extract incident angle information about the Talbot pattern we need a means to characterize the horizontal offset of the self-images. A straightforward solution, previously employed in macroscopic wavefront sensors, was to place an array of CCD or CMOS image sensors at one of the self-image planes [53, 54]. This previous work used gratings (and self images) that were significantly larger (pitch of d=250μm) than the pixels of the image sensor itself. Thus, the image sensor array could directly capture the self-image as a set of electrical signals. However, in our application, this approach would require manufacturing a very high density imager array. The array would need a pixel pitch of 1/4 the grating pitch (in our case, on the order of 200 nm) to effectively resolve the features of the Talbot image. Imager arrays with sub-micron resolution are extremely difficult to manufacture: although sub-micron photosensors can be built, the images they capture tend to be blurred by diffusion effects, limiting their actual resolution to 1μm or worse [59].

Rather than placing a complete imager behind each sensors grating, we add a second parallel analyzer grating at the self-image plane (Fig. 2.3) of identical period to the first grating. This second grating uses the moir effect to filter the Talbot image. When the intensity peaks align with gaps in the second grating (Fig. 2.3(b)), light passes through the analyzer grating. When the intensity peaks are out of alignment (Fig. 2.3(b)), the bars of the analyzer grating block the light. This technique is similar to one used in experiments involving the diffraction of atoms [60]. By placing a single large photosensor under the analyzer grating and measuring the total light flux, we extract the alignment of the self-image with the analyzer grating (Fig. 2.3(c)).

The total light flux detected is dependent on both the overall source brightness and the incident angle. This leads to an ambiguity between intensity and angle in

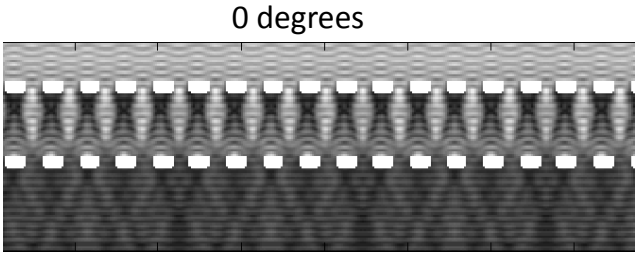

(a)

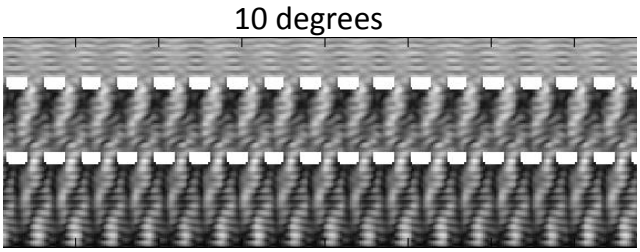

(b)

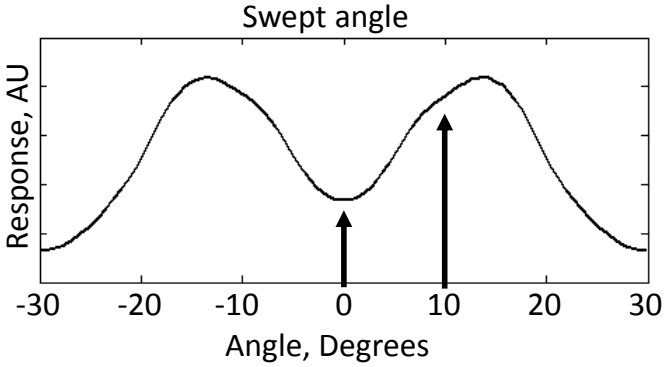

(c)

Figure 2.3: FDTD simulations illustrating the effect of including an analyzer grating at the half Talbot depth. (a) When the peaks of the self-image align with the bars of the analyzer grating, little light passes through to a light detector below. (b) When the incident angle is shifted so that the peaks align with gaps in the analyzer grating, much more light passes to the detector. (c) Intensity of detected light changes periodically with swept incident angle.

the sensor output, since a bright source at a blocked angle yields the same sensor output as a dimmer source at an angle passed by the analyzer grating. To disambiguate angle and intensity, we have placed multiple sensors (each with two stacked gratings and a photodiode) in close proximity so that they see approximately the same light field (Fig. 2.4). Each sensor has a different relative offset between the analyzer grating and the image-generating grating. Using the unique signals produced by each of the set of sensors, we can recover intensity and incident angle.

Because the lateral shift of the Talbot images is observed only for off-axis illumination at angles perpendicular to the grating lines, our sensors are responsive only to angles in one direction. In order to obtain full illumination angle information, we must place a second set of identical sensors with gratings rotated by 90 degrees, in close proximity to the first. This set is responsible for measuring the angle information ignored by the first set of sensors.

Our complete angle-sensitive pixel is composed of eight different sensors placed in close proximity. Four sensors are responsible for the angle in the xz plane; four more are needed for the angle in the yz plane. For both xz and yz gratings, we manufactured diffraction-analyzer offsets of 0, $d/4$, $d/2$ and $3d/4$. We placed the analyzer gratings at the half Talbot distance, the smallest distance where self-images with periodicity identical to the diffraction grating can be found.

Simulated responses for one set of four sensors under plane illumination of different angles are shown in Fig. 2.4(b). We observe that the transmission through the analyzer grating is periodic in incident angle, due to the lateral shift of the periodic self-images. The responses of these sensors can be approximately modeled

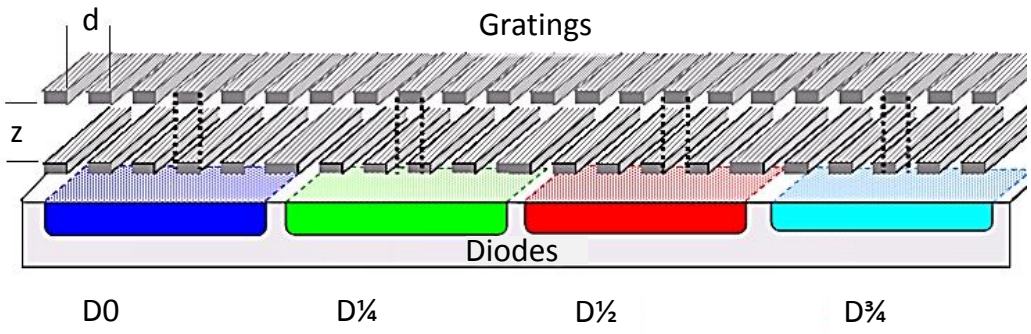

(a)

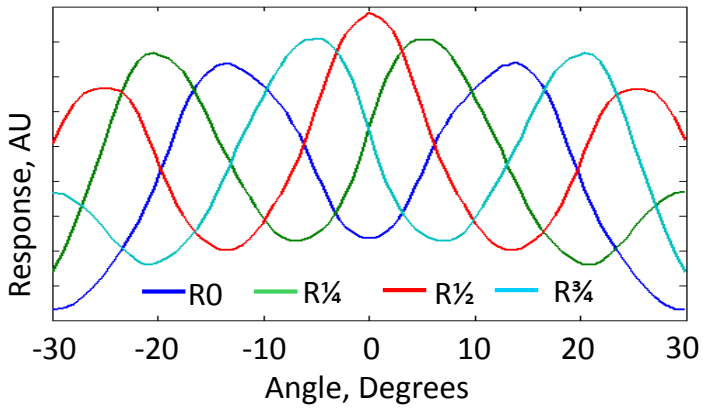

(b)

Figure 2.4: (a) Illustration of multiple, adjacent sensors, with stacked gratings at different offset above distinct photodiodes: black dotted lines illustrate relative alignment of the gratings. (b) Simulation results, similar to Fig. 2.3(c), but for various offsets: note that the incident angles that generate peak responses shift proportionally with the offset of the grating.

by the equations:

$$R_0 = I_0(1 - m\cos(\beta\theta)A(\theta) \tag{2.1}$$

$$R_{1/4} = I_0(1 + m\sin(\beta\theta)A(\theta) \tag{2.2}$$

$$R_{1/2} = I_0(1 + m\cos(\beta\theta)A(\theta) \tag{2.3}$$

$$R_{3/4} = I_0(1 - m\sin(\beta\theta)A(\theta) \tag{2.4}$$

I_0 is proportional to incident intensity, θ is incident angle, m is a measure of the modulation depth, and β is a measure of angular sensitivity. $A(\theta)$ is an even-symmetric function included to account for surface reflections and other effects that reduce responses to high angle incident light independent of angular sensitivity.

From the four outputs of equations 2.2–2.4, it is possible to determine the intensity and incident angle (in the xz plane) of light. Summing the ASP responses R_0 and $R_{1/2}$ (or $R_{1/4}$ and $R_{3/4}$) removes the modulation produced by incident angle and provides information on overall intensity.

$$I_0 A(\theta) = \frac{1}{2}\left(R_0 + R_{1/2}\right) = \frac{1}{2}\left(R_{1/4} + R_{3/4}\right) \tag{2.5}$$

Meanwhile, incident angle can be extracted as:

$$\theta = \frac{1}{b}\arctan\left(\frac{R_{1/4} - R_{3/4}}{R_0 + R_{1/2}}\right) \tag{2.6}$$

The second set of four sensors in the ASP has an identical model and extracts an intensity as well as incident angle, only in the yz plane. Hence, the ASP as a whole measures the intensity and average incident angle of the light striking it. Tiling such ASPs into arrays, we have an image sensor which creates a map of the light field at many points in the xy plane. This device is a light field image sensor.

2.5 Results

Small (8x8) arrays of the ASP described above were designed and manufactured using existing planar microfabrication techniques (Fig 2.5). We used the layers available in a standard complementary metal-oxide semiconductor (CMOS) fabrication process to integrate the multiple gratings and photosensors into one structure. While such manufacturing processes are typically used for integrated circuits, the availability of fine resolution metal interconnect wire layers with light-sensitive semiconductor devices is ideal for our structure.

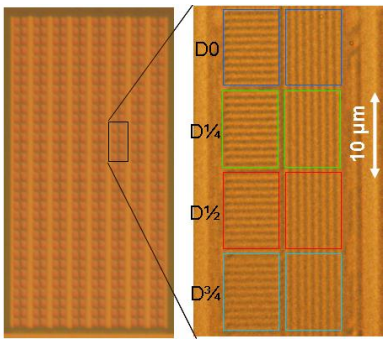

Figure 2.5: Microphotographs of 8x8 ASP array (left) and single group of 8 ASPs (right) manufactured in 130nm CMOS.

A single prototype ASP structure is shown in Fig. 2.5. The overall size is 20μm by 40μm, with each individual sensor being 10μm square. We designed the diffraction grating and analyzer grating in each of the eight sensors to be Ronchi rulings (equal width bars and gaps) using copper bars, with a period of 880nm. All other space was filled with silicon dioxide. Empirical simulations for green (λ=525 nm in vacuum) light determined the half Talbot distance in silicon dioxide to be 2 μm, and we selected the analyzer grating depth accordingly. A single p-n photodiode in each of the eight sensors measured the total light flux through the stacked gratings.

To test our ASP, a light source (commercial green LED, with center wavelength of 525 nm and spectral width of 32 nm) was mounted on a variable angle arm at a fixed distance from the fabricated arrays. We performed no additional collimation or filtering, as a non-ideal illumination source better approximates real-world imaging applications. When a range of wavelengths are present, the self-images observed are a superposition of the intensity patterns produced by each wavelength [61]. The spectral width of the source is relatively narrow and the path length differences which make the Talbot patterns are shorter than the sources

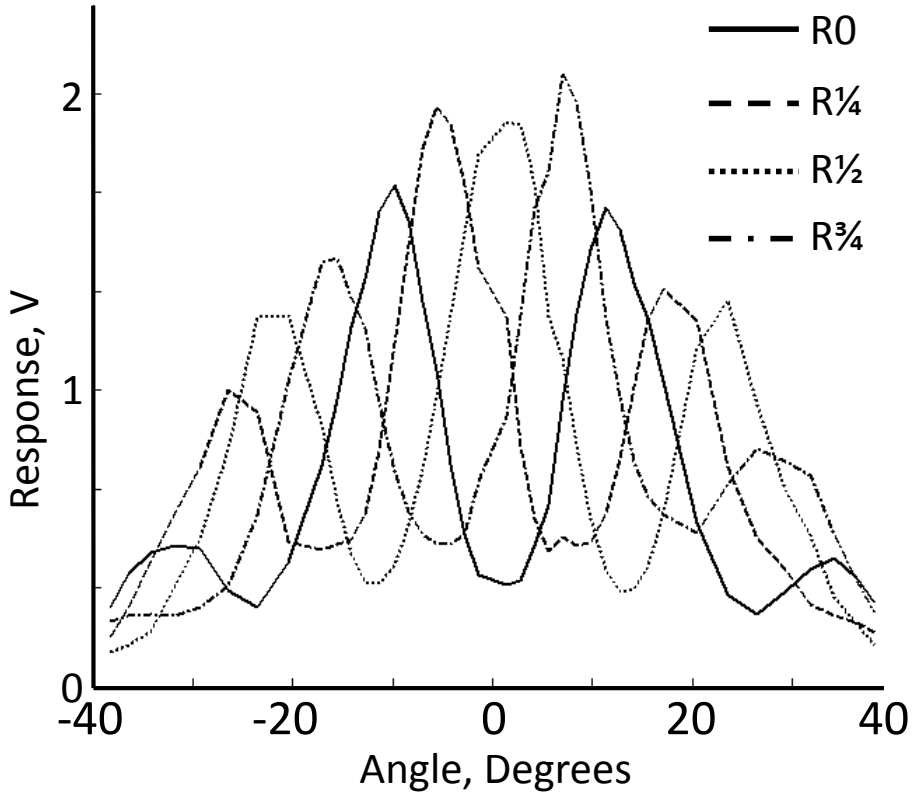

Figure 2.6: Measured responses of an ASP as incident angle is swept.

coherence length, so we did not expect significant deviation in performance from our monochromatic, coherent simulations.

We recorded the outputs of a single ASP for each angle as the source was moved. The outputs corresponding to one set of four sensors in the ASP are shown in Fig. 2.6. Reasonable agreement was obtained between measured results and those predicted by simulation. Fitting the curves in Fig. 2.6 with the model in equations 2.2–2.4: gives $\beta = 15$ and $m = 0.7$, with a root-mean-squared error of 9. The second set of four sensors (for characterizing angles in the yz plane) produced similar curves in response to changes in incident angle. Differences observed between measurement and idealized simulations such as those in Fig. 2.3 and 2.4 are due to reflection off the silicon dioxide surface, manufacturing variation, and the finite

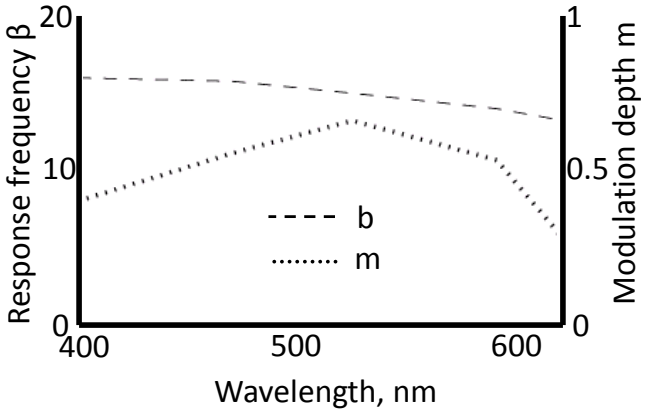

Figure 2.7: Measured responses of an ASP as incident angle is swept.

gratings actually used. However, our simulations reasonably characterized the angular sensitivity and modulation depth of the ASP.

Fine-pitch gratings are known to polarize the light they transmit. A recent study [62] on the polarization-dependent Talbot effect in high-density gratings predicts that the gratings we used, with period of approximately 2.5λ, should show significant polarization sensitivity. Specifically, the Talbot self-images formed at the half Talbot distance by TE (electric field parallel to the grating lines) polarized light should be approximately twice as bright as those formed by TM (magnetic field parallel to the grating lines) polarized light. Our observations are in good agreement with this prediction: when we rotated the polarization of the incident light on our ASP from TE to TM, the overall observed intensity decreased by a factor of 2.05. However, both angular sensitivity b and modulation depth m changed by less than 10%. These characteristics indicate that the TM-polarized Talbot self-images are weaker than the TE-polarized self-images, but otherwise behave similarly in their encoding of angle and intensity information.

The design was optimized for λ=525 nm, but we tested it across a range of wavelengths from 400 nm to 620 nm. We expected little change in angle sensitivity

b in response to changes in wavelength, as the Talbot self-images do not change in periodicity with changes in λ. This prediction was borne out by measurement, as can be seen in Fig. 2.7: β was only weakly sensitive to λ over the range 400nm to 620nm. However, changes in wavelength significantly change the Talbot distances. The analyzer grating was not optimally positioned when $\lambda \neq 525$ nm, so the observed self-images were blurred, and modulation depth, m, degraded. Over this range of wavelengths, we recover angle information less efficiently, but the angle sensitive function does not vanish. The fact that the ASP works across such a range of wavelengths is a direct consequence of analyzing the self-image at the half Talbot distance, where the relative depth of the Talbot pattern is least sensitive to λ.

To confirm the light-field imaging capability of our sensors, we placed a multi-mode fiber tip 500μm directly above the ASP array. After coupling light from a light emitting diode (identical to the one used in single ASP tests) into the fiber, light exiting the fiber will have a conical profile, and thus a simple divergent light field at the plane of the array. We recorded from all 64 sites on the ASP array and measured the output of each sensor, as shown in Fig. 2.8(a). As can be seen, adjacent sensors tuned to different angles responded very differently, and their relative responses depend upon their overall location relative to the light source. Applying equation 2.6 and the angle response data shown in Fig. 2.6, we reconstructed the light vectors for each ASP, as shown in Fig. 2.8(b).

To further confirm the capabilities of our array, we moved the light source to various locations in 3-dimensional space above the array. At each position we recorded the sensors responses and reconstructed the incident angle of light coming from the fiber. The array could be used to accurately reconstruct the location of the light source in two dimensions, as shown in Fig 2.9(a), where the

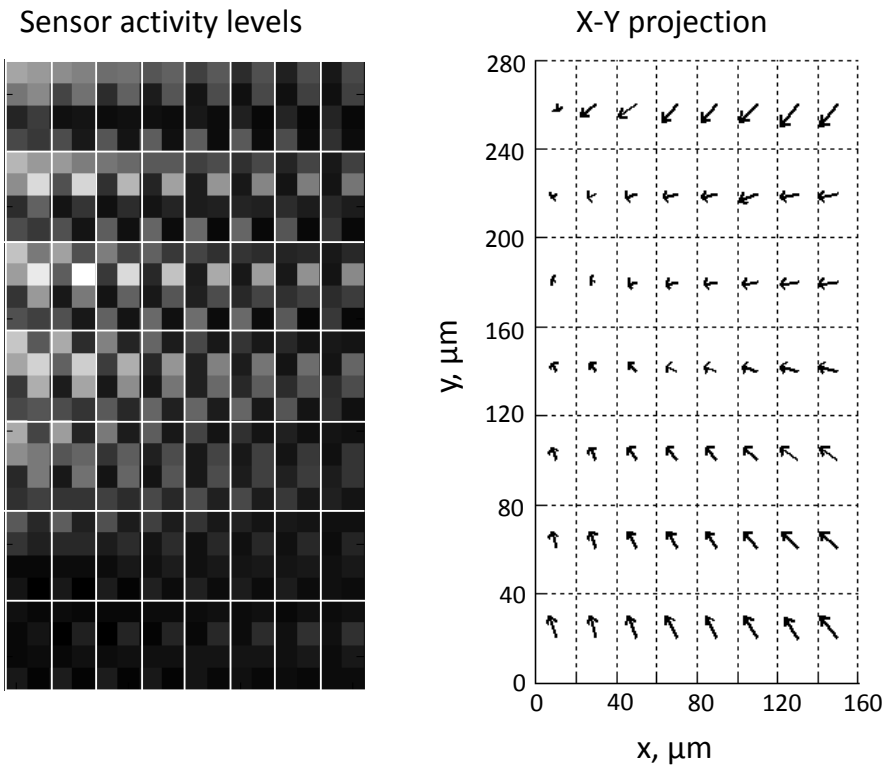

(a) (b)

Figure 2.8: Measured ASP array response to a light source held 500 μm above the array and slightly to the left. (a) Responses of individual sensors, where brighter squares represent more heavily illuminated sensors and white lines delimit individual ASPs. (b) Computed incident angle for each ASP (projected into the xy plane).

source was moved by 100 μm in the x-direction, and the computed incident angles reflect this. More strikingly, the array could be used to accurately localize the light source in the third, z direction, accurately capturing a 50 μm shift in the height of the source above the array, as shown in Fig. 2.9(b). Thus, an array of ASPs is able to accurately reconstruct the 3-dimensional structure of simple light sources, providing information beyond what is available from the intensity map of a standard image sensor.

For a single source, this extra information permits significantly more accurate

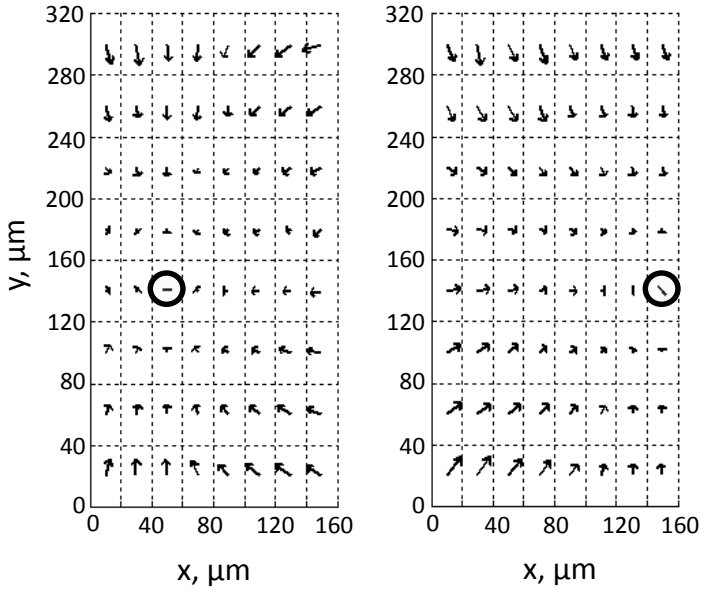

(a)

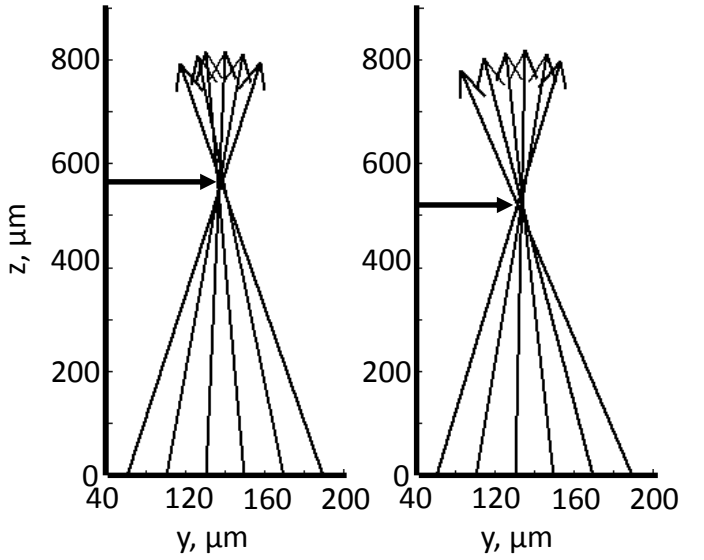

(b)

Figure 2.9: An 8x8 ASP array accurately resolves light source locations in 3D space. a) The measured light-vector field due to a source 550μm above the array can clearly reconstruct lateral shifts in location (in this case by 100μm). b) The measured light-vector field can also be used to reconstruct changes in depth (z) of a light source, in this case by 50μm.

localization than that shown in Fig. 2.9. Considering a single ASP located directly below the source, we find that the uncertainty in incident angle, σ_θ is ultimately limited by the uncertainty of individual sensor outputs, such that:

$$\sigma_\theta = \frac{\sqrt{2}}{m\beta}\frac{\sigma_R}{R} \tag{2.7}$$

Where m and b are the modulation depth and angular gain of the ASP, as in equation 2.2, and σ_R/R is the coefficient of variance of our measurements. This uncertainty corresponds to an uncertainty in lateral localization σ_x of

$$\sigma_x = z\sigma_\theta = \frac{z\sqrt{2}}{m\beta}\frac{\sigma_R}{R} \tag{2.8}$$

Where z is the axial height of the source. Along the z-axis, assuming the source is equidistant from two ASPs separated by distance l, we find that the uncertainty is

$$\sigma_z = \sigma_x 2\csc 2\theta = \frac{z\sqrt{2}}{m\beta}\frac{\sigma_R}{R}2\csc 2\theta \tag{2.9}$$

where z, m, β, σ_R/R are all as before, and θ is the angle of the source from normal. These uncertainties are upper bounds, since using all of the outputs of an ASP array provides more information about the sources location and results in reduced uncertainty.

For both lateral and axial localization, uncertainty in the location of a single point source is proportional to the vertical distance between source and sensor, and inversely proportional to the product of angular gain and modulation depth (m and β). This implies that resolution can be improved by increasing both m and β. The axial uncertainty is proportional to but always greater than lateral uncertainty and depends strongly on the maximum measurable angle. Therefore, to achieve optimal axial resolution, ASPs and arrays should be made able to detect large incident angles.

We performed a second set of measurements using the multimode fiber tip as a point source above the array. To examine the arrays ability to accurately localize

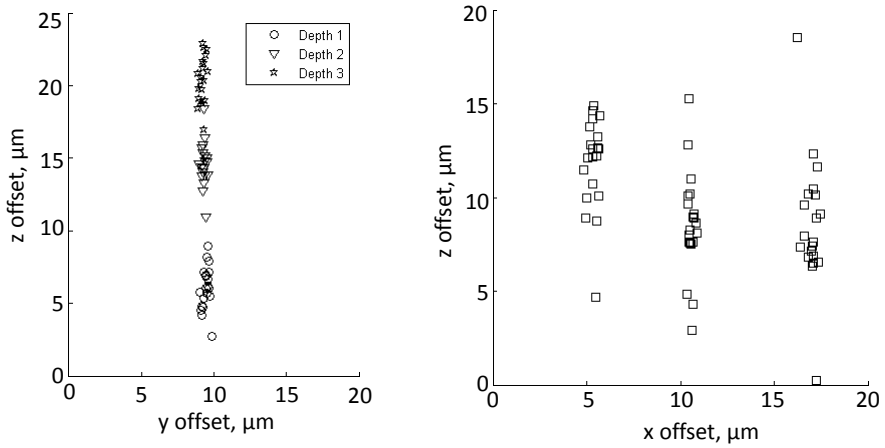

(a) (b)

Figure 2.10: An 8x8 ASP array resolves light source locations with high resolution. All measurements were taken at a height of 550μm. (a) Reconstructed locations of a source at three different depths separated by approximately 5μm are clearly distinct: $\sigma_y = 0.19\mu$m and $\sigma_z = 1.74\mu$m. (b) Reconstruction precision is much higher in the lateral (x) direction than in the axial (z) direction: observed $\sigma_x = 0.14\mu$m. Three different lateral positions are shown.

the centroid of the source in three dimensions, we moved the source in the smallest steps available, approximately 5 microns. At each location, we recorded multiple measurements (1kHz frame rate) from the array and independently rec onstructed the source location using each measurement. Each reconstructed location is shown as a point in the scatterplots of Fig. 2.10. For the experiment performed, the coefficient of variance of our measurements was 0.007 and the source was placed 550 microns from the imager. The predicted upper bound, based upon equations 2.8 and 2.9, was 0.5 microns for lateral uncertainty and 3 microns for axial uncertainty. Using the entire array, the observed standard deviations of $\sigma_x = 0.14\mu$m, $\sigma_y = 0.19\mu$m, and $\sigma_z = 1.74\mu$m are well below these bounds.

2.6 Discussion

We have demonstrated a structure that makes use of the Talbot effect on the microscale to perform light field imaging. By stacking two gratings separated by the half Talbot depth, we create a filter that selectively passes light from some incident angles and rejects others. Shifting the relative lateral offset of the gratings provides selectivity for different angles. A collection of several such filters each with a light sensor beneath forms a pixel-scale sensor that captures both incident angle and intensity. We have further demonstrated that arrays of such angle-sensitive pixels are capable of localizing light sources in 3-dimensional space.

The ASP structure we have demonstrated has several intrinsic benefits. All elements of the structure can be constructed using standard planar photolithography techniques, implying ease of scaling to large arrays. In fact, all of the elements of the design can be (and in this case were) constructed using the layers available in a standard integrated circuit manufacturing process. As a result, circuits typically found in digital image sensors can also be included in light-field imagers based upon this work. Implementing the proposed ASP in a standard integrated circuit design flow allows us to take advantage of the low cost and high reliability that comes with a fully developed manufacturing process.

ASP arrays also have a number of advantages over current methods for light-field imaging. In contrast to existing small-scale camera arrays employing microlenses [63], monolithic ASP arrays need no high precision alignment or post-processing. They are also cheaper and easier to manufacture than microlens-based solutions. Compared to large macroscopic camera arrays or scanning platforms [38–41], ASP arrays offer a compact, robust, easily deployed platform for capturing similar information. Because ASP arrays can be constructed using the same technology as high speed CMOS imagers, they are capable of high frame

rates which scanning techniques or CCD based sensors cannot achieve. Furthermore, ASP arrays directly capture incident angle and intensity information, which significantly reduces the computational effort required to determine the captured light field.

We anticipate a number of potential improvements to our current design. At the sensor level, the approach demonstrated places fairly minor restrictions on the size of the photodetector used, so more exotic sensors, such as single-photon avalanche diodes, could be used in place of simple photodiodes. At the ASP level, the demonstrated structure encodes angle with some ambiguity due to the periodic nature of equation (1) (see Figs. 4, 6). By using adjacent ASPs with different angular sensitivity, this ambiguity could be eliminated. Larger arrays of ASPs could be developed to explore this structures capabilities in real imaging applications while the size of individual ASPs can be reduced. Although the grating pitch is limited to be greater than wavelength, fewer periods of the grating could be used. In the design presented here between 8 and 11 periods were used, but fewer would also work, though with increased edge effects. Finally, when multiple light sources are present, there is no unique incident angle that describes the light field generated, and other algorithms must be developed to make full use of the information provided by our sensors under multi-source situations.

The structure we have demonstrated could find deployment in a variety of applications. Large arrays of ASPs, combined with typical lens systems, could be used in photography and microscopy applications to provide additional information about out-of-focus images for after-the fact computational refocus and range-finding. Alternately, deployed entirely without lenses, an array of ASPs could be used to capture the 3-dimensional structure of microscopic samples placed directly above the array. This lensless arrangement could find use in a variety of applications,

such as enhanced flow cytometry, and low-cost, field-deployable characterization of tissue samples.

In summary, this work provides a starting point for a more general exploration into micro-scale uses of the Talbot effect for light field imaging.

Chapter 3
Lensless fluorescent localization

3.1 Introduction

Determining the microstructure of a sample of interest is an important step in many biological assays. Typically, this task is performed optically, using focusing optics to form an image which falls on an array of photosensors (photodiodes or CCDs). These photosensors then convert the image into electrical signals for further analysis and processing. To acquire three-dimensional structure, the focusing optics must furthermore have scanning capabilities. To date, the external optics necessary for structure-aware sensors has made on-chip integration difficult, and all existing single-chip sensors perform measurements of total fluorescence while ignoring structure [64].

Here we present an image sensor, implemented in a standard 130nm CMOS process, which captures significantly richer information about the light it detects than typical photosensors. This additional information permits localization of multiple fluorescent sources in three-dimensional space. The sensor captures structural information without external optics or post-processing. Existing assays reliant on identifying micro-scale structure, such as clumps of beads in latex fixation tests [65] used to identify pathogens (Fig. 3.1) [66] or antibodies indicating exposure to pathogens [67], can take advantage of the simplicity of these sensors.

3.2 Background

In previous work, we demonstrated an angle sensitive pixel (ASP) [68], a micro-scale device manufactured in standard CMOS which responds to both the intensity

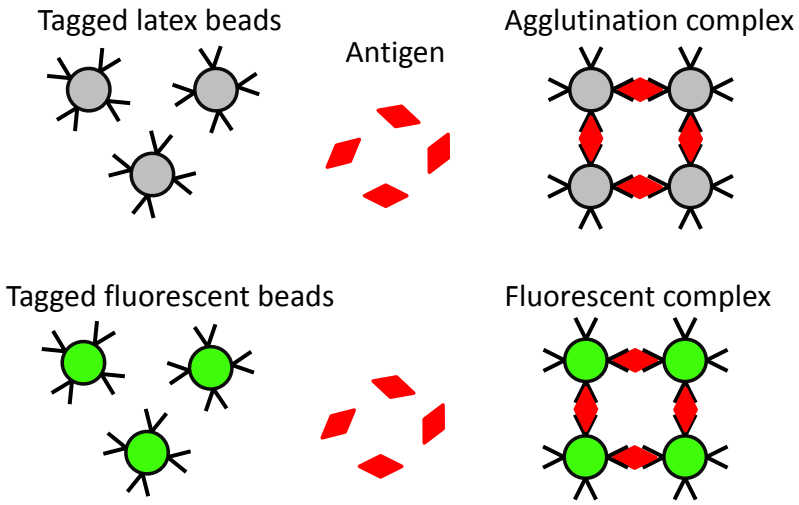

Figure 3.1: Latex fixation test. In both fluorescent and nonfluorescent cases, clumping of the individual beads is used to detect a specific antigen. Fluorescence structure, rather than intensity, determines the presence or absence of the assay target.

and incident angle of the light striking it. These structures employ two local diffraction gratings stacked on top of a photodetector to determine incident angle (Fig. 3.2(a)). Incident light striking the first diffraction grating generates periodic intensity patterns, called Talbot self-images, at specific depths below the grating. As incident angle changes, these intensity patterns shift laterally with little change in depth. The second grating lies directly above the photodetector and alternately blocks or passes the bulk of the light in the pattern. The detector responds strongly when intensity maxima align with the gaps of the second grating (Fig. 3.2(b)), and weakly when intensity minima align with the gaps of the second grating (Fig. 3.2(a)). Therefore, the photodetector measures a periodic function of incident angle, as shown in Fig. 3.2(c).

To distinguish the difference between change in incident angle and intensity, a single ASP employs eight such grating-detector units, each with distinct orientations and lateral offsets in the local gratings (Fig. 3.2(d). Each unit has a response

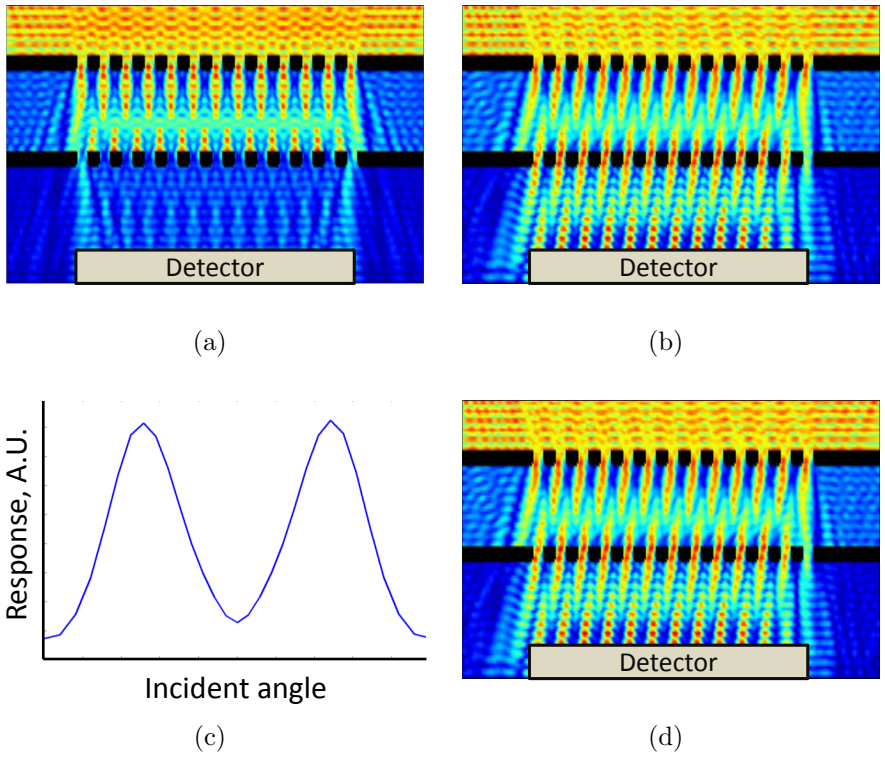

Figure 3.2: Angle sensitive pixels and the Talbot effect: (a) Zero degree incident angle; (b) 15 degree incident angle; (c) Simulated response of detector to incident angle; (d) Layout of typical angle sensitive pixel showing 8 distinct sensors

I which follows the form:

$$I = I_o A(\theta)(1 - m\cos(\beta\theta + \alpha)) \tag{3.1}$$

Where I_o is incident intensity, θ is incident angle (swept orthogonal to the gratings), $A(\theta)$ is a symmetric windowing function that captures reflection effects, and m, α and β are parameters that depend on the geometry of the ASP gratings.

Compared to the typical pixels employed in CMOS and CCD imager chips, angle sensitive pixels (ASPs) extract significantly more information about the light they see. Furthermore, acquiring this additional information does not require any additional post-processing or fabrication as ASPs can be directly manufactured in commodity CMOS processes. Interconnect metal layers form the micro-scale

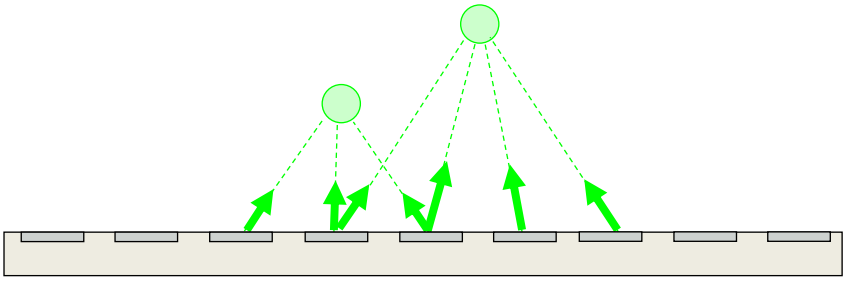

Figure 3.3: Ambiguity of incident angle with multiple sources. For either left or right source, incident angle informs location. With multiple sources, incident angle is unclear.

diffraction gratings, while doped semiconductor regions form p-n photodiodes. The simplicity and scale of individual ASPs allows arrays to be manufactured easily.

3.3 Motivation

In previous work, the information obtained from existing small (8x8) ASP arrays was sufficient to localize the three-dimensional position of a single point source with high precision [28]. The information in each ASP was converted to a vector representing the intensity and incident angle observed by a given pixel (composed of 8 sensors with responses of the form in Eq. 3.1). Simple triangulation of these vectors was sufficient to determine a three-dimensional location for the source. However, multiple sources, such as those in Fig. 3.3, generate responses that cannot be well described with a single angle. In addition, the periodic nature of an ASP's response leads to ambiguity that is difficult to resolve when multiple sources are present. Additional information is needed to find the position of multiple sources.

The key to localizing multiple sources is to rely on diversity in angle-sensitive pixels, in particular, by varying α and β in adjacent pixels. If adjacent ASPs have distinct angular sensitivities, their responses will be less correlated, recovering

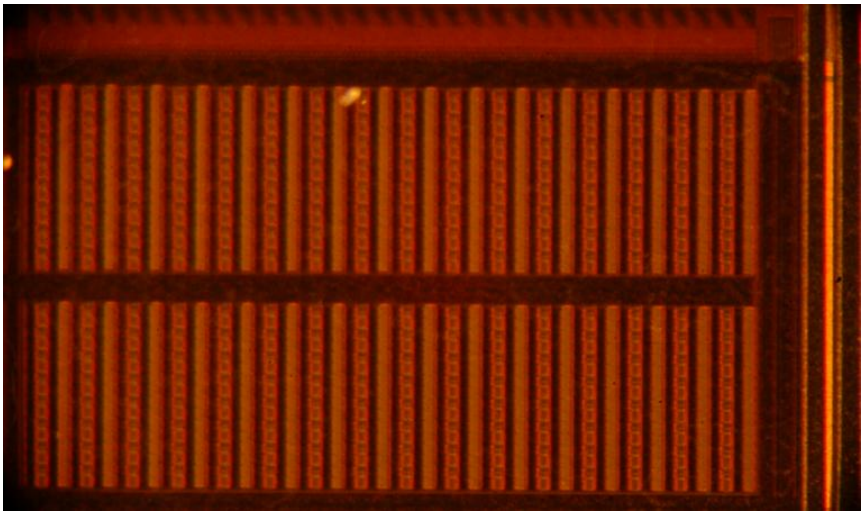

Figure 3.4: 32x32 array of angle sensitive pixels (8192 individual sensors) manufactured in 130nm standard CMOS process. Approximate dimensions: 700 microns wide, 1200 microns long.

more information about the available incident light, aiding in the localization of multiple sources. For the manufacturing process used here, four ASP designs, two with small vertical inter-grating spacing and two with large vertical inter-grating spacing, provided good performance. Based on simulation, the ASPs with small inter-grating spacing are predicted to have a low periodicity response (small β) to incident angle; large inter-grating spacing results in an ASP with a high periodicity response to incident angle (large β).

3.4 Results

We manufactured a 32x32 array of ASPs using all four designs in an IBM analog/mixed mode 130nm CMOS process. Figure 3.4 shows a photo of the entire array. All measurements were taken with bare dies as received from the foundry. We did not perform any post-processing or modification on the dies. To confirm angle sensitivity, we fixed packaged dies to a freely rotating mount facing a col-

limated beam of light generated by a green LED (center wavelength 532nm and spectral width 25nm). As the chip rotated, we measured the response of each of the four ASP designs to changes in incident angle. The observed responses are very similar to the predicted ASP responses. Two measured responses from particular ASPs, one low periodicity (small inter-grating spacing) and one high periodicity (large inter-grating spacing), are shown in Fig. 3.5(a) and 3.5(b).

These directly measured responses contain both intensity as well as incident angle information. To extract the structure-dependent response of the two different ASPs, we subtracted complementary sensory outputs (those with identical β but with α's different by π) to obtain the curves of Fig. 3.5(c) and 3.5(d). If we normalize by the sum of the same pair of outputs, Eq. 3.1 predicts the result to have a sinusoidal response of the form

$$I = I_o m \cos(\beta\theta + \alpha) \tag{3.2}$$

Figures 3.5(e) and 3.5(f)demonstrate the periodic response to incident angle for two phases (α=0, $\pi/2$) and two periodicities (β = 12, 20). The measured incident angle dependent curves closely follow the sinusoidal model of Eq. 3.2.

Localization was performed using the difference-and-normalize approach used to generate Eq. 3.2. As overall intensity information is normalized, all of our results rely exclusively on the measured angular information. Suppressing intensity information provides better insensitivity to measurement artifacts such as fixed pattern noise. Furthermore, the fact that ignoring intensity information does not degrade our ability to localize sources indicates that there is far more useful information in local angular information than in intensity.

For multiple source localization, we placed two fluorescent clumps (irregularly shaped, approximately 100 microns in size, and composed of Invitrogen FluoSpheres with 510nm emission peak) at a height of approximately 1.5mm above

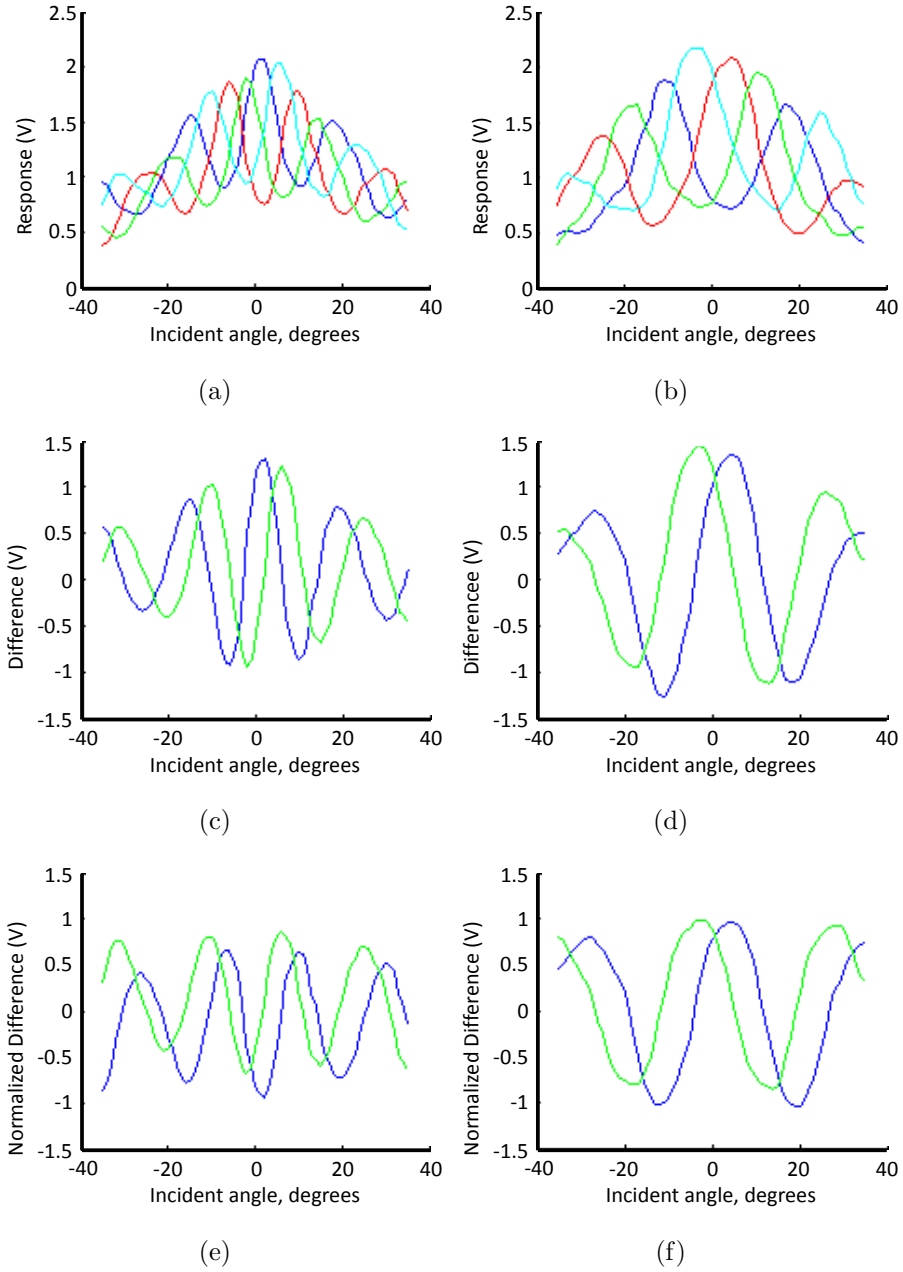

Figure 3.5: Representative ASP outputs: (a) and (b), response to incident angle for the four different offsets α in one orientation for two ASPs with different βs; (c) and (d), difference between responses of complementary offsets (pairs where α's are different by π); (e) and (f), difference between responses of complementary offsets normalized by their respective sums. These two normalized outputs are sinusoidal in nature and exhibit a phase shift of $\pi/2$.

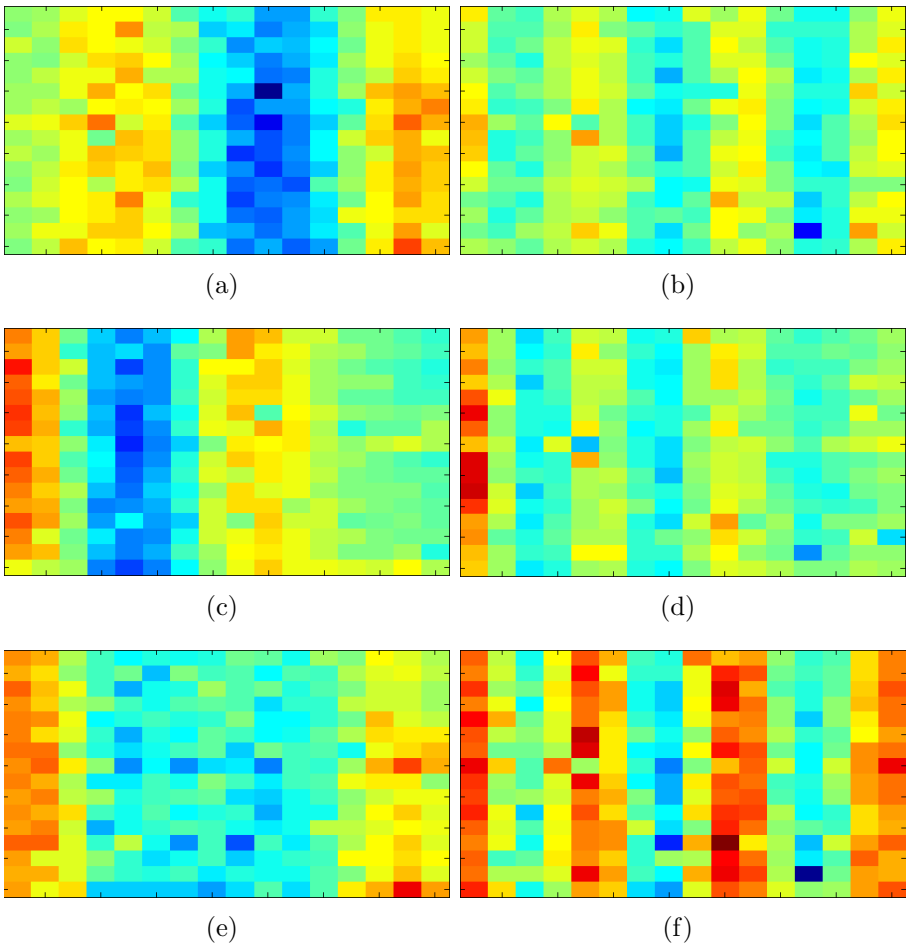

Figure 3.6: Example array outputs for different source configurations. (a) and (b), one fluorescent source for two sensors with different β values; (c) and (d), different fluorescent source at another location for same types of sensor; (e) and (f), both sources simultaneously illuminated. Responses in (e) suggest either single distant source or relatively uniform illumination. Responses in (f) suggest a single nearby source. Considering both (e) and (f) together suggests that the source arrangement is more complex (multiple sources).

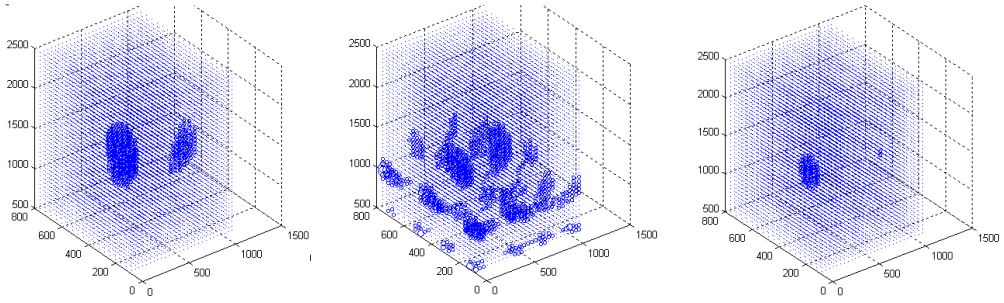

(a) (b) (c)

Figure 3.7: Estimated position of a single source based on correlations between predicted and observed sensor outputs: (a) estimate using only low periodicity ASPs, (b) estimate using only high periodicity ASPs, (c) estimate using both types of ASP.

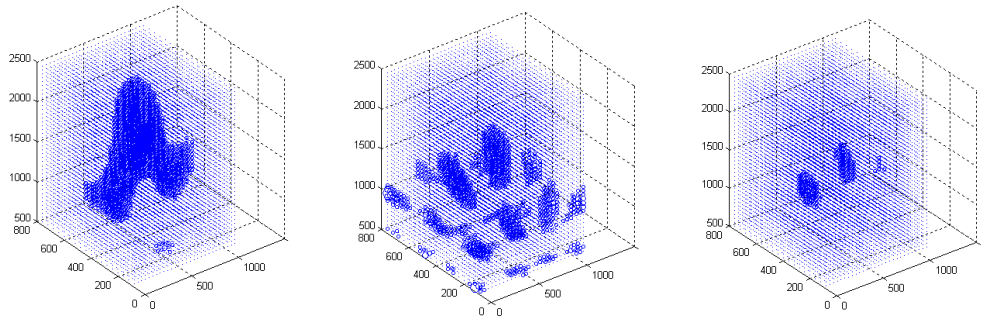

(a) (b) (c)

Figure 3.8: Estimated position of two sources based on correlations between predicted and observed sensor outputs: a) estimate using only low periodicity ASPs, b) estimate using only high periodicity ASPs, c) estimate using both types of ASP.

the array. Figures 3.6(a)–3.6(d) show the fluorescence responses recorded for one orientation of two different ASP types with different β values when the two clumps were stimulated individually. The periodic nature is clearly apparent. Stimulating both clumps simultaneously and measuring from the same ASP types, we observe the responses in Figs. 3.6(e) and 3.6(f).

To determine the fluorescent source arrangement in three dimensions, we predicted the response of each sensor to a source at each location (using Eq. 3.2)

and correlated these predicted responses to the actual response to estimate the likelihood of a source at each location. First, this technique was used to attempt identification of a single source. Using only the responses of a single ASP type with low β, we observe a high likelihood for sources in two locations (Fig. 3.7(a)). If we use only the response of a single ASP type with high β, we observe many possible sources (Fig. 3.7(b)). When we use the predictions both sensor types provide, we find the more precise position of a single source (Fig. 3.7(c)).

We observe similar results in the presence of two sources. Figures 3.8(a) and 3.8(b) illustrate ambiguous source location estimates when using only a single ASP type. However, the combination of both low β and high β ASPs permits not only determination of the presence of two sources but also localization of their position (Fig. 3.8(c)).

3.5 Conclusion

We have employed angle sensitive pixel arrays in the imaging and localization of multiple fluorescent sources in free space. These arrays can be implemented in commodity CMOS manufacturing processes and require no further modification. In addition, they require no external optics to determine the presence and positions of multiple sources. Instead, these arrays rely on gathering a richer description of available light than the intensity maps provided by typical CMOS imager. In fact, as used here, pure intensity information, the only information a standard imager provides, has been entirely ignored while capturing three-dimensional structure. A key to capturing sufficiently rich information is to deploy a diverse set of angle sensitive pixels, each with different response properties. Going forward we see applications for this technology in biological assays like the latex fixation test where acquiring simple structural information about a sample is important.

Chapter 4
Basis pursuit denoising

4.1 Introduction

4.1.1 Basis Pursuit Denoising

Finding the best sparse representation for high-dimensional data is an important step for many applications in signal processing [69–71] and statistics [72,73]. Solving the underdetermined system of linear equations $\mathbf{y} = \mathbf{A}\mathbf{x}$ (where $\mathbf{A}$ is an $M \times N$ matrix and $M < N$) subject to a sparsifying regularizer is effective in identifying such representations. Regularization can be thought of as a mathematical implementation of Occam's Razor: in the face of many possibilities, all of which are plausible, favor the simplest candidate solutions. In this context, $\mathbf{y}$ is the $M \times 1$ vector of observed data, $\mathbf{A}$ is a transform matrix composed of N atoms, and $\mathbf{x}$ is the $N \times 1$ solution vector.

One way to ensure maximum sparsity in $\mathbf{x}$ is to solve the problem:

$$\min_{\mathbf{x}} \|\mathbf{x}\|_0 \quad \text{subject to} \quad \mathbf{y} = \mathbf{A}\mathbf{x} \tag{4.1}$$

where $\|\mathbf{x}\|_0$ is simply the number of nonzero components of $\mathbf{x}$. Unfortunately, solving Equation 4.1 usually involves a combinatorial search, making it computationally intractable. Minimization using the l_1 norm, which often delivers the same solution as the l_0 norm [74,75], is frequently substituted:

$$\min_{\mathbf{x}} \|\mathbf{x}\|_1 \quad \text{subject to} \quad \mathbf{y} = \mathbf{A}\mathbf{x}. \tag{4.2}$$

The above minimization problem is also known as basis pursuit [76]. Although the l_1 norm is weaker than l_0 in ensuring sparsity, l_1-regularized optimization is a convex problem and admits efficient solution via linear programming techniques.

In many applications (see Section 4.2) it is desirable to trade off exact congruence of $\mathbf{Ax}$ and $\mathbf{y}$ in exchange for a sparser $\mathbf{x}$. In these cases, a more appropriate formulation is basis pursuit denoising (BPDN) [71,77]. BPDN involves solving the following problem:

$$\min_{\mathbf{x}} \frac{1}{2}\|\mathbf{y} - \mathbf{Ax}\|_2^2 + \lambda\|\mathbf{x}\|_1. \tag{4.3}$$

BPDN (closely related to LASSO regression [72] and see Equation 4.6) is simply least-squares minimization with an l_1 regularizer to penalize complex solutions. The regularization parameter $\lambda > 0$ establishes the cost of complexity relative to the least-squares error $\frac{1}{2}\|\mathbf{y} - \mathbf{Ax}\|_2^2$ and is typically chosen to be large enough that $\|\mathbf{x}\|_0 \ll M$.

4.1.2 Notation

We introduce some notation for the problem in Equation 4.3 that will be useful later. Let $\mathbf{x}$ be candidate solutions of Equation 4.3. Let $\mathbf{r}$ be the residual $\mathbf{r} \equiv \mathbf{y} - \mathbf{Ax}$. $f(\mathbf{x})$ is the total error to minimize, such that $f(\mathbf{x}) = \frac{1}{2}\|\mathbf{r}\|_2^2 + \lambda\|\mathbf{x}\|_1$. This total error can be divided into a reconstruction imperfection term $\frac{1}{2}\|\mathbf{r}\|_2^2$ and the regularizer $\lambda\|\mathbf{x}\|_1$. The imperfection term $\frac{1}{2}\|\mathbf{r}\|_2^2$ penalizes the deviation of the expected observations $\mathbf{Ax}$ from the actual observations $\mathbf{y}$, while $\lambda\|\mathbf{x}\|_1$ penalizes solutions where the sum of $|x_k|$ is high. The dot product of two vectors is denoted with angle brackets $\langle\,,\rangle$ and element-by-element vector multiplication is $*$. Let p be the number of nonzero components of the $\mathbf{x}$ that solves Equation 4.3. We assume that the l_2 norm of the columns A_i of $\mathbf{A}$ is 1, and that $\mathbf{y}$ lies within the subspace spanned by these columns.

4.1.3 Organization of the Manuscript

In Section 4.2 we describe applications of BPDN, including the 3D imaging application [28,29] that motivates us to look for fast BPDN solvers. Section 4.3 outlines prior work towards obtaining solutions to Equation 4.3. The in-crowd algorithm is given in Section 4.4 along with convergence proofs (also see Appendix 4.10) and iteration bounds. Section 4.5 compares the accuracy of BPDN reconstructions to those of some alternative sparse solvers. Section 4.6 benchmarks the in-crowd algorithm against alternatives, and investigates the effect of changing λ. Section 4.7 investigates a regime of dense BPDN problems where alternative solvers are faster than the in-crowd algorithm. Finally, Section 4.8 derives an expression for the computational complexity of an iteration of the in-crowd algorithm and provides avenues of exploration that may yield faster variants of the in-crowd algorithm for different problem scales.

4.2 Motivation and Background

4.2.1 Applications of BPDN

There are two broad categories of application in which solving Equation 4.2 will not recover a useful, sparse $\mathbf{x}$; specifically:

Category 1: $\mathbf{y} = (\mathbf{A}\mathbf{x}) * (1+\eta)$ where $\mathbf{x}$ may be sparse, but η is $M \times 1$ noise with a large enough magnitude that solving Equation 4.2 exactly would constitute unacceptable overfitting. For these problems, λ is set to be high enough that the effect of the regularizer in Equation 4.3 is at least as large as the effect of η.

Category 2: $\mathbf{y}$ was not generated by the linear matrix multiplication of an $\mathbf{A}$

matrix with a sparse $\mathbf{x}$.

Problems falling into Category 1 include:

i: Computer vision and reconstruction problems [78]

ii: Recovering sparse, noisy signals or images [79, 80]

Problems falling into Category 2 include:

i: Lossy image or video compression or encoding with overcomplete dictionaries [81–83]

ii: Image deblurring [84, 85]

iii: Reconstructing the few sparse, strongest components of a dense $\mathbf{x}$, typical in compressed sensing [86] imaging applications

iv: Image denoising with an overcomplete basis [87].

The denoising form of basis pursuit is therefore used for many real-world problems.

4.2.2 Imaging with ASPs and BPDN

Finding fast solutions to large-scale, ill-conditioned BPDN problems is needed for a 3D imaging application described in the remainder of Section 4.2.

Determining the three-dimensional arrangement of light sources is an important component of many biological assays and studies [88, 89]. As static optical sensors can only measure information at a fixed two-dimensional plane, the recovery of three-dimensional structure is intrinsically an underdetermined problem. The majority of contemporary techniques rely on scanning or complex optical systems to overcome this measurement deficiency [89]. We have recently demonstrated a new class of angle sensitive pixel (ASP) based imager which directly recovers sufficient

information to permit 3D reconstructions of sparse light sources [28, 29]. An ASP observes a signal which follows the relation:

$$R = I_0(1 - m\cos(\beta\theta + \alpha))A(\theta)(1 + \eta), \tag{4.4}$$

where R is the readout of the ASP, I_0 is a constant proportional to the light flux at the ASP, θ is the incident angle along the optically-sensitive axis, β is the angular sensitivity (designed to be in the 7–50 range), m is the modulation depth of the ASPs (designed to be maximal; typical values of m are approximately 0.6), α is a designable phase offset, $A(\theta)$ is a slowly-varying aperture function and η is multiplicative noise. Compared to traditional intensity-sensitive pixels, the outputs of heterogeneous arrays of ASPs have a more independent output when exposed to out-of-focus light sources.

We search for a sparse set of candidate light sources that account for the observed signal by posing a BPDN problem that reconstructs the location and intensity of several nearby light sources, as follows. Assume that there is some volume of interest in which we wish to determine the location and magnitude of a variety of light sources. We parcel the volume into N individual subregions, and form the vector $\mathbf{x} = [x_1, x_2, \ldots x_N]^T$ where the i^{th} component x_i represents light source intensity at the i^{th} subregion. Using Equation 4.4, we determine the response of the M ASPs for unit intensity at each individual subregion. The normalized individual responses to light at one location define one column A_i of the matrix $\mathbf{A}$. The system is linear, so for a given arrangement of sources in space $\mathbf{x_0}$, the product $\mathbf{Ax_0}$ predicts the sensor outputs $\mathbf{y_0}$ we would observe. Therefore, for a given observed set of outputs $\mathbf{y}$, the solution to Equation 4.3 provides a reasonable guess at the true structure of the few luminous sources.

Two features that are readily apparent are the scale of the optimization problem and the ill-conditioned nature of the matrix $\mathbf{A}$. Dividing a volume of one cubic

millimeter into parcels 10 microns on a side results in an N of 10^6, while a small imager might have $M \approx 10^4$–10^5 sensors. Furthermore, spatially adjacent sources are likely to produce very similar responses. This results in a high mutual coherence [90] for $\mathbf{A}$ (see Figure 4.1 for the distribution of off-diagonal entries of $\mathbf{A}^T\mathbf{A}$ for a sample problem with 12500 spatial locations and 625 sensors). Therefore, any BPDN solver appropriate for this reconstruction problem must be able to handle poorly conditioned matrices and very large problem scales. These two requirements drove our development of the in-crowd algorithm.

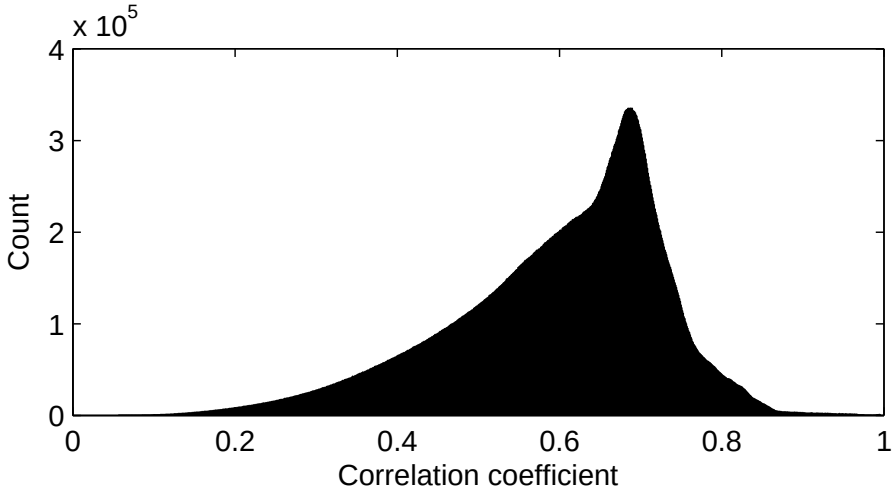

Figure 4.1: Distribution of correlation coefficients of the columns of $\mathbf{A}$ for a sample imaging problem with $N = 12500$ and $M = 625$.

4.3 Solving BPDN

In this Section we review established approaches to solving Equation 4.3 quickly for sparse $\mathbf{x}$. One popular approach to solving BPDN is based on homotopy [91]. Homotopy methods trace the global optimal solution path over changing λ. For $\lambda = \infty$ the optimal solution is trivial: $\mathbf{x} = \mathbf{0}$. Relaxing λ from ∞ causes the optimal solution path to leave the origin and introduce nonzero components. Further

decreases may introduce new nonzero components or drive existing components to zero; hence homotopy methods return not only a solution for a given λ, but also the solution trajectory $\mathbf{x}(\lambda)$ illustrating the optimal solution for a whole range of λ. By virtue of their reliance on the overall optimum solution as components enter and exit the active set, these optimizers are very efficient for sparse $\mathbf{x}$ (see [92] and the associated implementation at [93]). Homotopy is the fastest alternative to the in-crowd algorithm for solutions to Equation 4.3 on our imaging application (see Section 4.2.2), as will be shown in Section 4.6.2.

Another fast method which can be made to converge to the solution to Equation 4.3 is the spectral projected gradient for L1 minimization (SPGL1) [94, 95]. This method probes the shape of the trade-off curves between solutions of l_1 minimization of $\mathbf{x}$ for a constrained $\|\mathbf{r}\|_2^2$ (Equation 4.5) and l_2 minimization of $\mathbf{r}$ for a constrained $\|\mathbf{x}\|_1$ (Equation 4.6, also known as the LASSO problem [72]). This method is faster than homotopy for problems where columns of $\mathbf{A}$ are nearly orthogonal, as will be shown in Section 4.6.1.

Implementations of SPGL1 do not directly solve Equation 4.3, rather they solve either

$$\min_{\mathbf{x}} \|\mathbf{x}\|_1 \text{ subject to } \|\mathbf{y} - \mathbf{A}\mathbf{x}\|_2^2 \leq \sigma \tag{4.5}$$

or

$$\min_{\mathbf{x}} \|\mathbf{y} - \mathbf{A}\mathbf{x}\|_2^2 \text{ subject to } \|\mathbf{x}\|_1 \leq \tau. \tag{4.6}$$

For benchmarking purposes, in this paper we determine the time taken for SPGL1 to reach the exact solution of Equation 4.3 by first computing $\tau = \|\mathbf{x}\|_1$ where $\mathbf{x}$ is the homotopy BPDN solution, then solving Equation 4.6 with SPGL1.

Interior point methods solving Equation 4.3 as a general convex problem also solve BPDN. A method using the preconditioned conjugate gradients algorithm to compute a search direction has shown itself to perform well on large problems

[96]. However for the problems presented in this paper we found the homotopy implementation to be faster than these methods, so we will not cover them in detail.

Fixed-point continuation (FPC) [97], both using Barzilai-Borwein steps [98] and with an active set implementation [99], is also potentially an attractive BPDN solver. As will be shown in Section 4.6.1, for sparse problems the active set FPC method's run times compare with homotopy's and for more dense problems FPC is the fastest BPDN solver (see Section 4.7). However, FPC is known to produce incorrect solutions in some hard cases [97]. In fact, on the imaging problem (see Section 4.6.2), we will show active set FPC routinely fails to converge to a solution close to the correct $\mathbf{x}$ (see Figure 4.5).

For no problem was the speed of the Barzilai-Borwein FPC method [98] competitive, as will be shown in sections 4.6.1 and 4.6.2. FPC can take a value of λ as an input so that its target is to solve Equation 4.3; we have provided this λ as an input throughout the paper. One additional class of interest for smaller problems is gradient projection for sparse reconstruction (GPSR) [100]. Although we investigated this class of BPDN solver, under no circumstances did it deliver a solution faster than some alternative solver (be it homotopy, active set FPC or SPGL1), so we do not report its results.

4.4 In-Crowd Optimization

In this section, we introduce the in-crowd algorithm, an iterative method for solving BPDN that is effective especially for large scale sparse problems, and prove its convergence. The flavor of the in-crowd algorithm can be summarized as follows: *think globally, but not too often.* The computational complexity of solving Equation 4.3 with sufficiently large N and small p is often dominated by searching the

dictionary of N possible atoms for appropriate additions to the active set I. The in-crowd algorithm is partially insulated from the size of the global problem by consulting the full dictionary only rarely. Very often, candidates for additions to I remain viable even after adding other candidates. Performing an entirely new search over the N possible additions after each addition to I thus can be computationally wasteful. Instead, the in-crowd algorithm admits a whole group of L atoms to I, where L is a fixed small integer, before referring to the full $\mathbf{A}$ matrix again.

4.4.1 The In-Crowd Algorithm

Here is the procedure for in-crowd optimization.

Step 1: Declare $\mathbf{x}$ to be $\mathbf{0}$, so $\mathbf{r} = \mathbf{y}$.

Step 2: Declare the active set I to be the empty set.

Step 3: Calculate the "usefulness" $u_j \equiv |\langle \mathbf{r}, A_j \rangle| \, \forall \, j \in I^c$ where I^c denotes the complement of I.

Step 4: If on I^c no $u_j > \lambda$, then terminate.

Step 5: Otherwise, add the L components with the largest u_j to I, but do not add any component for which $u_j \leq \lambda$.

Step 6: Solve Equation 4.3 exactly on the subspace spanned by all of the components in I. Use current values of $\mathbf{x}$ to warm-start the solver. This subproblem is expected to be dense.

Step 7: Take any zero-valued members of the exact solution of Step 6 out of I.

Step 8: Set all components of $\mathbf{x}$ to be 0 except for the components in I; set these to the value found by the exact solution of Step 6.

Step 9: Update $\mathbf{r} = \mathbf{y} - \mathbf{A}\mathbf{x}$; n.b. $\mathbf{A}\mathbf{x}$ can be found during the subproblem of Step 6 since $\forall\, j \in I^c$, $x_j = 0$.

Step 10: Go to Step 3

In Step 5, the best choice of L depends on the relative speed of Steps 6 and 3 for a specific problem and computer architecture. We find $L = 25$ to be reasonable for most problems and we have used it exclusively throughout this paper. However, for different choices of matrix $\mathbf{A}$ or for problems (such as partial Fourier observations) with an implicit fast method for finding $\mathbf{A}\mathbf{x}$, other fixed or adaptive choices for L can provide advantages in computation time (see Section 4.8.5). We used MATLAB's built-in `quadprog` function [101, 102] for our subproblem solver (see Section 4.8.2) in Step 6 when the cardinality of I was $< M$ and an alternative quadratic programming solver[1] [103] when the cardinality of I was $\geq M$.

The stopping criterion in Step 4 is equivalent to terminating when I does not change from one iteration to the next. In practice, subproblem solvers may not fully optimize in Step 6, so this alternative stopping criterion can be more numerically robust.

4.4.2 Convergence of the Algorithm

To show that the in-crowd algorithm always terminates at the global optimum, it suffices to prove that:

Item 1: The error $f(\mathbf{x})$ calculated in Step 6 is completely specified by I.

Item 2: There are a finite number of possible sets I.

[1] MATLAB's built-in quadprog does not always respect the boundary conditions given when the cardinality of $I \geq M$, necessitating an alternative exact solver. In our benchmarks, this alternative solver was almost never used since the cardinality of I usually remained well below M, but was needed as a patch especially for larger problems with small λ.

Item 3: Step 6 will always decrease the error relative to the previous round; i.e. $f(\mathbf{x}_{t+1}) < f(\mathbf{x}_t)$.

Item 4: At termination, nonzero components x_k of $\mathbf{x}$ satisfy $\langle \mathbf{r}, A_k \rangle = \text{sgn}(x_k)\lambda$, and zero components x_j of $\mathbf{x}$ satisfy $|\langle \mathbf{r}, A_j \rangle| \leq \lambda$.

Items 1 and 2 are trivial, but items 3 and 4 are subtle enough to warrant a proof. Item 3 is proven in Theorem 4.10.1; moreover under certain circumstances the error $f(\mathbf{x})$ is proved to decay exponentially with iteration count (see Appendix 4.10). Step 6 will find the solution that minimizes $f(\mathbf{x})$ on I and may not end up assigning a nonzero value to all of the newly-added components, but the final error $f(\mathbf{x})$ is guaranteed by Theorem 4.10.1 to be lower than during the previous execution of Step 6.

The in-crowd algorithm therefore cannot retrace its own path, eliminating the potential for cycles. Moreover it makes use of the best possible choices for additions to I given local knowledge of $\mathbf{r}$ by adding components to I with the highest u. Since the in-crowd algorithm never retraces its path and traverses a finite number of elements, it must terminate. We now prove that the in-crowd algorithm terminates only at the exact BPDN solution (Item 4) by pointing out a feature of the in-crowd algorithm's stopping condition that we will tie to general convex optimization theory in Appendix 4.11.

Theorem 4.4.1 *When the in-crowd algorithm terminates, all components x_i of $\mathbf{x}$ are either equal to zero and $|\langle \mathbf{r}, A_i \rangle| \leq \lambda$, or alternatively are nonzero and satisfy $\langle \mathbf{r}, A_i \rangle = \text{sgn}(x_i)\lambda$.*

Proof By Step 4, the in-crowd algorithm does not terminate if for any $j \in I^c$, $u_j \equiv |\langle \mathbf{r}, A_j \rangle| > \lambda$. Regarding the non-zero components $\{x_k\}$, $k \in I$, their values have been optimized by the exact solver of Step 6. On $\{x_k\}$, the gradient of

$f(\mathbf{x})$ exists (since there are no discontinuities in the gradient of $f(\mathbf{x})$ except where $x_i = 0$), and (by force of the exact optimization) must equal $\mathbf{0}$, since any non-zero gradient would imply a better solution than the one found by the exact subproblem solver. By Equation 4.11 of Appendix 4.11, the gradient being $\mathbf{0}$ implies that $\langle \mathbf{r}, A_k \rangle = \text{sgn}(x_k)\lambda$.

As established by general convex optimization theory, the conditions established in Theorem 4.4.1 are both necessary and sufficient for the optimality of the solution $\mathbf{x}$ (see Appendix 4.11) generated by the in-crowd algorithm. Therefore the in-crowd algorithm halts only at the global minimizer to Equation 4.3.

4.4.3 Lower Iteration Bound

A lower bound on the iteration count, $\lceil \frac{p}{L} \rceil + 1$, is given by the fact that at least $\lceil \frac{p}{L} \rceil$ iterations are required increase the cardinality of I to p, and one partial iteration (terminating at Step 4) is required to confirm the optimality of $\mathbf{x}$ (i.e. to check that the subdifferential of f contains $\mathbf{0}$, see Appendix 4.11).

There is no guarantee that the same few elements will be not be added then pruned multiple times, however by Items 1 and 3 above we are guaranteed that each temporary addition to I must be made with distinct combinations of components in I, each with lower associated $f(\mathbf{x})$ than all previous combinations, limiting the number of possible cyclic additions and deletions of all atoms. As will be shown in Section 4.8.1 and the insets of Figures 4.3, 4.4, 4.6 and 4.7, the lower bound given here is in fact reasonably tight.

4.5 Greedy Solvers and BPDN

4.5.1 Greedy Solvers

As $f(\mathbf{x})$ is a convex function, improved solutions can be found using only local knowledge of f around $\mathbf{x}$. Several existing heuristics take advantage of this property to find sparse $\mathbf{x}$ where $\mathbf{y} \approx \mathbf{A}\mathbf{x}$. Examples include Orthogonal Matching Pursuit (OMP) [104], Stagewise OMP [105] and least angle regression (LARS) [106]. These approaches build their solution element by element, choosing the best available atoms at each iteration. Every iteration adds these selected A_i to an active set of columns.

Recent solutions in a similar spirit to the in-crowd algorithm are CoSaMP [90] and subspace pursuit [107]. Both of these add the ability to prune unnecessary elements from the current active set of columns, and both solve a least squares problem on their active sets at each iteration. Indeed, the primary difference between the in-crowd algorithm and these two procedures is that with the in-crowd algorithm, an l_1 regularizer (with a λ equal to that of the global problem) is included in the subproblem.

It should be noted that unlike the greedy solvers mentioned above, the in-crowd algorithm solves Equation 4.3 exactly.

4.5.2 BPDN Yields Better Imaging Reconstructions

For our imaging application, the accuracy of reconstructions is higher for BPDN than for the other sparse solutions found by OMP, CoSaMP and subspace pursuit. To quantify the benefit of BPDN, we took the imaging problem whose $\mathbf{A}$ matrix generated Figure 4.1 and judged reconstruction of sources based on a noisy signal. In more detail, S true sources with intensity in $[-1, 1]$ were chosen randomly to

generate $\mathbf{x}_{ideal}$, and noiseless data $\mathbf{y}_{ideal} = \mathbf{A}\mathbf{x}_{ideal}$ was generated. We presented the solvers with $\mathbf{y} = \mathbf{y}_{ideal} * (1 + \eta)$ where η is $M \times 1$ Gaussian noise such that the signal-to-noise ratio of $\mathbf{y}$ is 10. Figure 4.2 then plots the mean correlation coefficient between $\mathbf{x}$ and $\mathbf{x}_{ideal}$ over 100 runs for solutions of Equation 4.3 with $\lambda = 0.2$ along with those from OMP, subspace pursuit and CoSaMP.

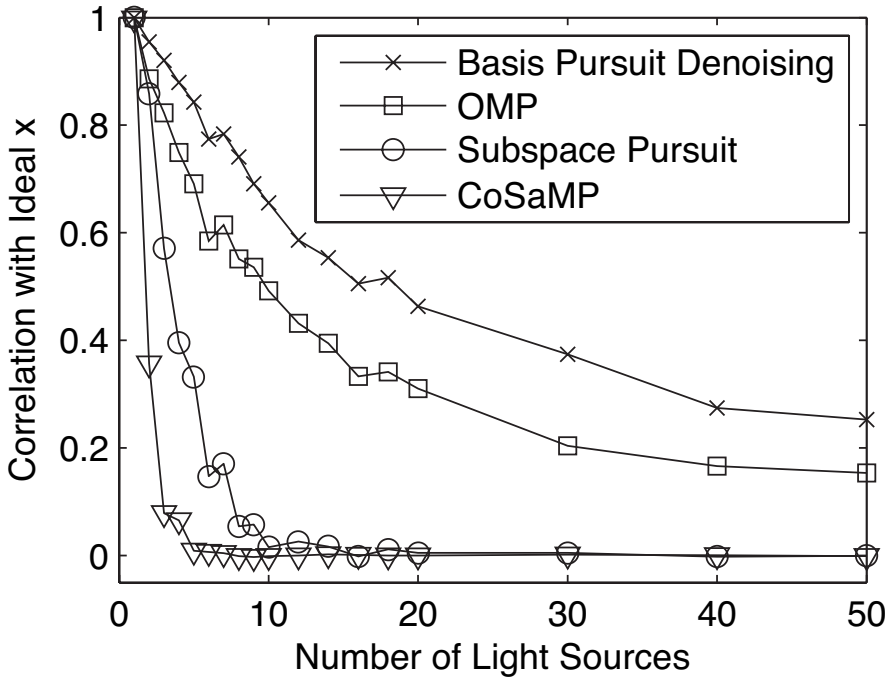

Figure 4.2: Accuracy of four reconstruction methods for the imaging problem with $M = 625$, $N = 12500$ and various numbers of light sources S.

Subspace pursuit and CoSaMP fare particularly poorly at this task, since the pseudoinverse computation these methods employ tends to partition power equally among components of $\mathbf{x}$ with highly correlated corresponding A_k (see Figure 4.1).

4.6 Observed Performance of the In-Crowd Algorithm

4.6.1 Matrices with Small Correlations

To the extent that it is possible to control $\mathbf{A}$, for nearly all applications it is advantageous to make the columns of $\mathbf{A}$ as orthogonal as possible. As a consequence, many applications that use BPDN employ $\mathbf{A}$ matrices with small-magnitude correlations between rows. Although when $M < N$ it is impossible to have columns totally orthogonal, by the central limit theorem the expected magnitude of correlation coefficients between columns of a random i.i.d. Gaussian $\mathbf{A}$ goes as $\frac{1}{\sqrt{M}}$. Benchmarking solutions to Equation 4.3 with a random $\mathbf{A}$ matrix therefore gives a reasonable approximation to the expected running times of applications where the columns of $\mathbf{A}$ are nearly orthogonal.

We generated a sequence of problems (see Table 4.1) defined by a spherical ($\|A_k\|_2 = 1$) Gaussian random matrix $\mathbf{A}$ with various M and N. We generated synthetic data $\mathbf{y}$ in a manner similar to that of Section 4.5.2, i.e. by starting with a vector $\mathbf{x}_{ideal}$ with S nonzero components pulled from a random uniform distribution over $[-1, 1]$, applying $\mathbf{A}$ and injecting multiplicative Gaussian noise to arrive at an SNR of 10.

Solving Equation 4.3 with $\lambda = 0.2$ results in a solution with a number of nonzeros p that may be greater or smaller than S, and the average p was also found to depend on the problem type (Gaussian p_G or Imaging p_I - see Section 4.6.2). To avoid favoring methods using MATLAB's built-in functions, we translated all methods into `c++` via MATLAB's `mcc` command and compiled the `c++` code with `gcc 4.1.1` with all optimizations possible. We timed the execution of 50 problems on a 2.4 GHz Core i7 system with turbo boost disabled to obtain the benchmarks for in-crowd, the fastest homotopy solver we found for these problems [92, 93],

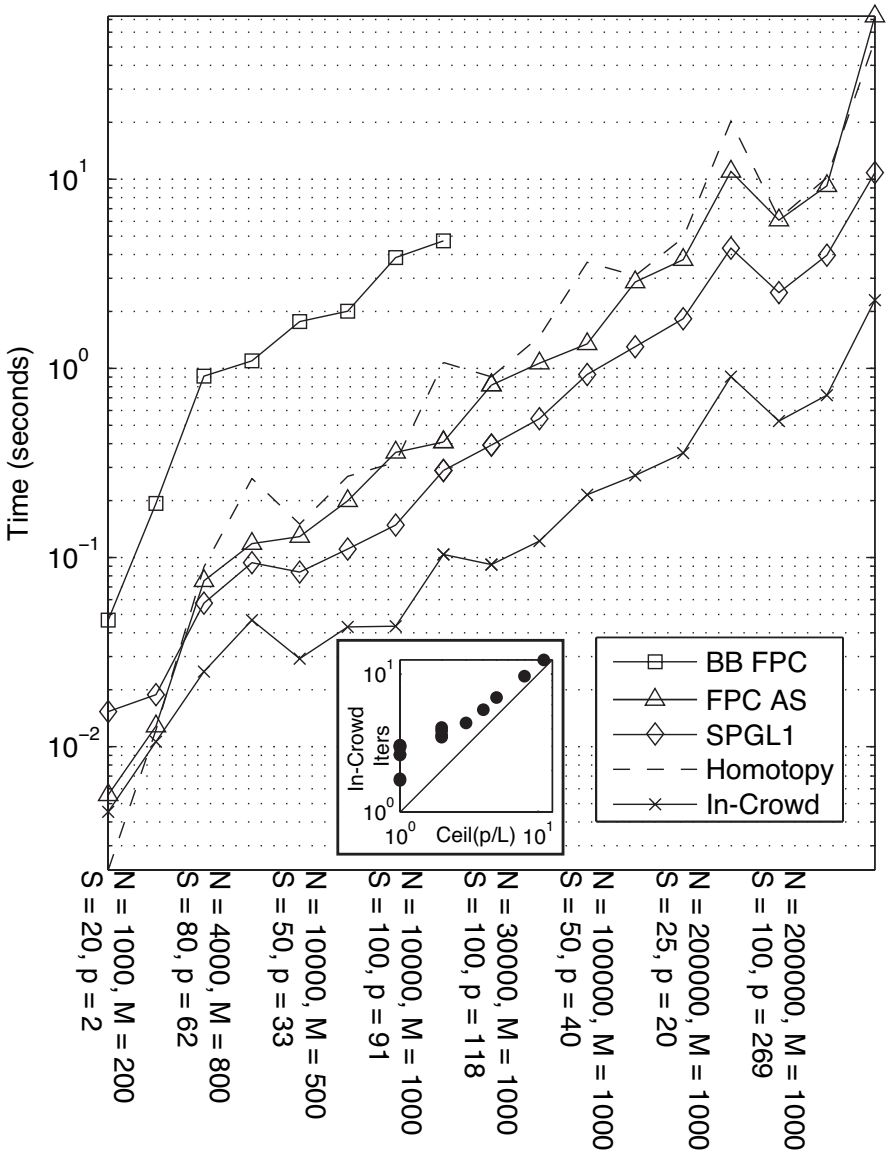

Figure 4.3: Running time for random Gaussian matrices. For clarity, every second problem size is labeled; for a full list of problem sizes see Table 4.1. Inset: mean in-crowd iteration count as a function of Ceil($\frac{\text{mean}(p)}{L}$); log scale used.

the spectral projected gradient for L1 minimization (SPGL1) [94, 95] and two implementations of FPC: Barzilai-Borwein FPC (BB FPC) [98] and active set FPC (FPC AS) [99]. Mean running times in seconds are plotted in Figure 4.3 and listed in Table 4.2. The inset of Figure 4.3 shows that the number of iterations

Table 4.1: Problem Definitions

Problem	N	M	S	p_G	p_I
1	1000	200	20	1.52	7.42
2	4000	200	20	1.48	8.02
3	4000	800	20	14.8	21.7
4	4000	800	80	61.9	46.1
5	10000	500	25	14.4	23.2
6	10000	500	50	32.7	30.9
7	10000	1000	25	20.1	30.0
8	10000	1000	100	91.4	69.1
9	30000	1000	25	19.3	35.3
10	30000	1000	50	39.6	54.1
11	30000	1000	100	118.2	77.1
12	100000	1000	25	20.1	35.6
13	100000	1000	50	39.7	61.1
14	100000	1000	100	196.1	80.5
15	200000	1000	25	19.8	38.1
16	200000	1000	50	41.4	56.7
17	200000	1000	100	269.1	82.0

the in-crowd algorithm takes is close to the lower bound derived in Section 4.4.3.

As can be seen in Figure 4.3 and Table 4.2, the in-crowd method is up to 5.5 times faster than all other solvers for $N \geq 4000$. Its closest rival (SPGL1) in fact solves LASSO (Equation 4.6) rather than BPDN; the fastest alternative BPDN solver of problem 17 (homotopy) is more than 23 times slower than the in-crowd algorithm.

The maximum l_1 deviation of the in-crowd and homotopy solutions (i.e. $\|\mathbf{x}_{in\,crowd} - \mathbf{x}_{homotopy}\|_1$) for any run was within the range of deviations entirely accountable by finite machine precision: $5 * 10^{-13}$. SPGL1 converges iteratively to the exact LASSO solution. Using the default SPGL1 stop criterion [94] (optimality tolerance = 10^{-4}), SPGL1 halted relatively close to the solution found by the other solvers. SPGL1's maximum l_1 deviation was 0.004, which, while larger than that of the solution delivered by homotopy, results in only a minuscule increase in

Table 4.2: Running Times in Seconds for Gaussian Random Problems

Problem	In-Crowd	Homotopy	SPGL1	FPC AS	BB FPC
1	0.00453	0.00223	0.0153	0.00557	0.0467
2	0.0106	0.0123	0.0189	0.0129	0.194
3	0.025	0.0893	0.0575	0.0753	0.911
4	0.0468	0.262	0.094	0.119	1.1
5	0.0292	0.15	0.0838	0.129	1.77
6	0.043	0.269	0.111	0.2	2.01
7	0.0434	0.32	0.149	0.36	3.86
8	0.104	1.07	0.289	0.408	4.72
9	0.0918	0.903	0.393	0.818	long
10	0.122	1.47	0.542	1.07	long
11	0.215	3.64	0.93	1.35	long
12	0.272	3.09	1.3	2.87	long
13	0.357	4.91	1.83	3.76	long
14	0.906	20.3	4.33	11.0	long
15	0.527	6.2	2.52	6.09	long
16	0.723	10.2	3.97	9.24	long
17	2.29	54.4	10.8	72.9	long

final $f(\mathbf{x})$.

4.6.2 3D ASP Imaging Application

We ran a suite of test problems similar to those of Section 4.6.1 but with $\mathbf{A}$ based on models of our imaging application (see Section 4.2.2); the timing results can be found in Figure 4.4 and Table 4.3 (n.b. the FPC variant mentioned here is Barzilai-Borwein, see below). The inset of Figure 4.4 shows that the number of iterations taken by the in-crowd algorithm is a factor of 2.56–6.86 greater than the lower iteration bound derived in Section 4.4.3. The increased number of iterations compared to the previous set of benchmarks is due to the difficulty selecting the appropriate atom out of a collection of atoms that are highly correlated. Still, the ratio of iterations taken by the in-crowd algorithm to the lower bound is small,

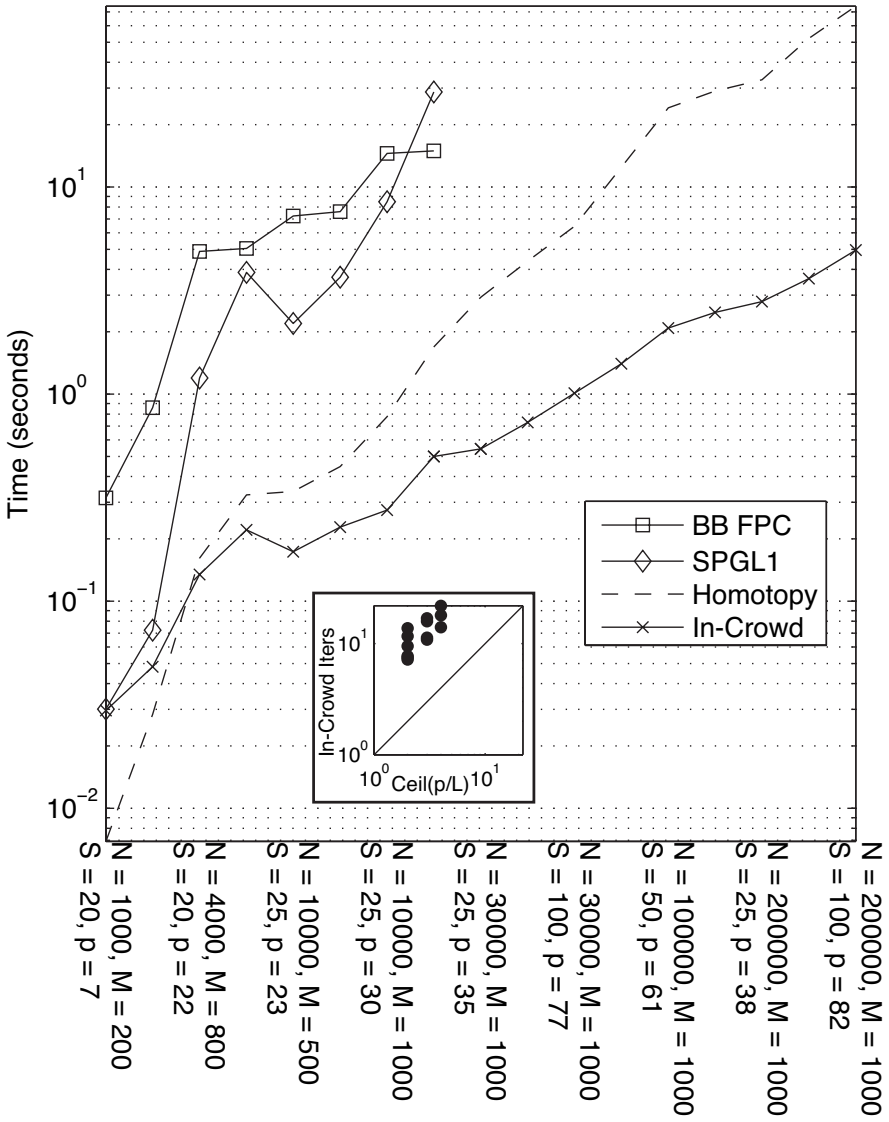

Figure 4.4: Running time for the imaging problem. For clarity, every second problem size is labeled; for a full list of problem sizes see Table 4.1. Inset: mean in-crowd iteration count as a function of Ceil($\frac{\text{mean}(p)}{L}$); log scale used.

indicating that the in-crowd algorithm is relatively robust in the face of poorly conditioned problems.

On these problems, we discovered that SPGL1, the fastest exact solver aside from the in-crowd for nearly-orthogonal $\mathbf{A}$ problems, does not converge quickly, so we ceased our benchmarks of this method for large-scale problems. SPGL1 still

Table 4.3: Running Times in Seconds for Imaging Problems

Problem	In-Crowd	Homotopy	SPGL1	BB FPC
1	0.0297	0.00692	0.0301	0.315
2	0.0482	0.0284	0.0725	0.859
3	0.134	0.161	1.2	4.88
4	0.221	0.326	3.87	5.05
5	0.173	0.338	2.19	7.25
6	0.228	0.446	3.67	7.6
7	0.275	0.778	8.48	14.5
8	0.5	1.69	28.7	14.9
9	0.543	2.94	long	long
10	0.729	4.38	long	long
11	1.01	6.45	long	long
12	1.4	12.5	long	long
13	2.08	24.1	long	long
14	2.48	29.1	long	long
15	2.8	32.9	long	long
16	3.61	52.3	long	long
17	4.96	74.8	long	long

seems to converge exponentially, but the exponential constant is small.

We found the active set implementation of FPC [99] did not converge well even for our smallest problems. In the cases where the active set method did converge to the correct solution, the discrepancy between its solution and that of other BPDN solvers was of the order expected by finite machine precision; however especially for problems larger than problem 2, for the large majority of problems the active set method had a catastrophically-large terminal $f(\mathbf{x})$: more than twice that of the other solvers (see Figure 4.5). In general, FPC is known to fail to converge for some difficult problems [97], although solutions delivered by Barzilai-Borwein FPC were more reasonable. As such we benchmarked only the Barzilai-Borwein FPC variant.

Although the l_1 divergence between homotopy and the in-crowd solutions was higher than for the Gaussian case ($3 * 10^{-7}$ for problem 17), the corresponding

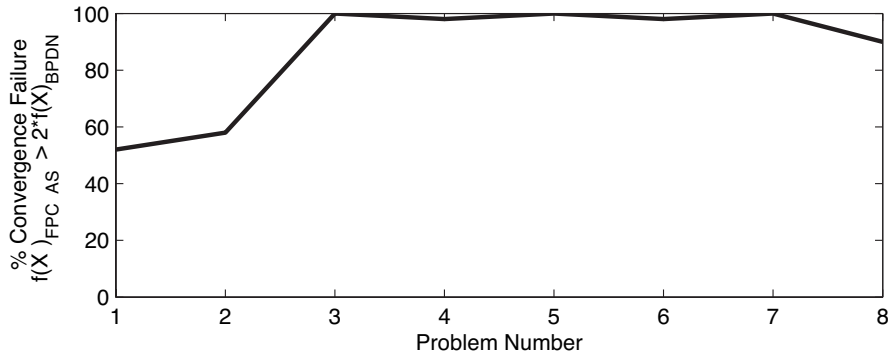

Figure 4.5: Proportion of problems where active set FPC failed to discover a solution with an $f(\mathbf{x})$ within a factor of 2 of the correct BPDN solution as a function of problem number (see Table 4.1).

median difference in $f(\mathbf{x})$ was within machine precision: $2{*}10^{-14}$. This discrepancy is possible because level surfaces of $f(\mathbf{x})$ around the minimum will be elongated whenever two nonzero, nearly-parallel atoms exist as part of the true solution. As before, for this problem type the in-crowd algorithm was the fastest solver by a factor of 15 for the largest-scale problems.

As is evident from p_I shown in Table 4.1, BPDN did not in general return the solution corresponding to the exact light source locations. From Figure 4.2, we see reconstruction accuracy is approximately 40% when $\frac{M}{S}$ is 20. However, due to the high correlations of the columns representing adjacent spatial locations, often the discrepancy between ideal and observed $\mathbf{x}$ corresponded to blurring, omitting dim sources or small shifts in the inferred source location, and the reconstructed sources are overall in a configuration similar to their actual locations. Our imaging application [28,29] introduced in Section 4.2.2 motivates our interest in high-noise, very sparse, very underdetermined, ill-conditioned problems; the in-crowd algorithm excels in this regime.

4.6.3 Changing λ and Noise Levels

Thus far, all benchmarks discussed were run with $\lambda = 0.2$ and SNR $= 10$, meaning that the average influence of noise on the observed $\mathbf{y}$ is relatively large and the strength of the regularizer is about twice the strength of the noise. With a large enough λ, the cardinality of I never grows to be too large, so the dense subproblem of Step 6 can be solved relatively quickly. With a smaller λ it is possible that not only more components will be involved with every subproblem (making individual iterations slower), but also that the total number of iterations taken by the in-crowd algorithm increases as the residual becomes more influenced by noise than by correct choices for additions to I.

To observe the effect of decreasing λ we performed two numerical experiments[2], both based on Gaussian problem 14 of Table 4.1. In one, noise and λ are scaled down together (Figure 4.6(a)) and in the other, noise is held with a constant SNR of 10 while λ is scaled down (Figure 4.6(b)). The insets in these figures plot the number of iterations taken by the in-crowd algorithm as a function of the lower iteration bound (see Section 4.4.3). Except where noise is much stronger than λ (to the right of Figure 4.6(b)), the lower iteration bound is relatively tight.

The vertical dashed line in Figure 4.6(b) divides problems with choices of λ appropriate for denoising (to the left of the line) from those with λ insufficient to denoise the signal (right of the line). Most real problems of interest, where noise suppression is desirable and overfitting of noise is not, are expected to use λ greater than noise. If high levels of noise are combined with a low λ, the result is a high in-crowd iteration count (see inset of Figure 4.6(b)) and longer running times than the other methods. Outside the zone where λ is too small and for the entirety

[2] As before, homotopy and the in-crowd algorithm yielded solutions almost exactly congruent with each other. The maximum l_1 deviation of the in-crowd and homotopy solutions was less than $1.4 * 10^{-9}$ for any problem.

Table 4.4: Running Times in Seconds for Imaging Problem 14 with Changing λ

λ	SNR	In-Crowd	Homotopy
0.20	10	2.37	27.4
0.05	40	7.21	65.4
0.05	10	7.58	66.3
0.02	100	17.4	120.0
0.02	10	18.0	122.0

of Figure 4.6(a) (which plots performance where λ is proportional to noise), the in-crowd algorithm is still the fastest BPDN solver for this class of problem.

We also tested the effect of lowering λ on imaging problem 14. As before, we tested the cases both where the signal-to-noise ratio (SNR) equaled 10 and when the SNR was set to $\frac{2}{\lambda}$. As shown in Table 4.4, running times increase modestly with decreasing λ.

4.7 Low-Noise, Dense Problems

The imaging problems that inspired work on the in-crowd algorithm (see Section 4.2.2) are of a scale with $\frac{M}{p} \approx$ 10–40: less sparse than some interesting BPDN problems, but sparser than others. Typical video compression problems with an overcomplete basis [81] have $\frac{M}{p} \approx$ 50–200; a relatively high-magnitude $\|\mathbf{r}\|_2$ is acceptable and a correspondingly large λ is used. In addition to sparse, noisy problems, Figure 4.6(a) demonstrates that the in-crowd algorithm is even better suited to very sparse, very underdetermined problems with low noise and λ, and thus small final $\|\mathbf{r}\|_2$.

Compressed sensing problems [69, 70, 86] give rise to a class of very low-noise BPDN problems that are less sparse, with $\frac{M}{p} \approx 5$ and $\frac{N}{M} \approx 3$. Compared to the BPDN problems presented thus far, in these applications noise is small and there

Table 4.5: Dense Problem Definitions; $\lambda = 0.0005$, SNR = 10000

Problem	N	M	S	p_G	Accuracy
18	5000	2000	500	856	97.7%
19	10000	5000	1000	1322	97.5%
20	20000	5000	1000	1912	98.7%
21	50000	10000	1500	2354	99.3%
22	50000	10000	2000	4557	99.1%

are many more observations per unknown. Given the additional high-fidelity data available, the underlying signal $\mathbf{x}_{ideal}$ is expected to be reconstructed more or less exactly unless p is overwhelmingly large. We ran a set of dense problems defined in Table 4.5 with results plotted in Figure 4.7 and Table 4.6 to characterize in-crowd performance on dense problems. Despite the deceptively high p_G (which includes many almost-zero terms), for every problem in this suite the correlation coefficient between the recovered $\mathbf{x}$ and $\mathbf{x}_{ideal}$ was high (mean correlation given in % in Table 4.5) and never less than 96% for any problem. While the iterative methods (the active set FPC method and SPGL1) both perform well on these problem scales, it is worth noting that the in-crowd algorithm maintains a run-time advantage over homotopy. Moreover, the fact that the number of iterations taken by the in-crowd algorithm was almost exactly equal to the lower iteration bound (shown by the proximity of points to the diagonal in the inset of Figure 4.7) indicates that extremely few false steps were ever taken by the in-crowd algorithm. Perhaps a choice of $L = 25$ is overly cautious for this type of low-noise, nearly fully determined problem; see Section 4.8.5 for a discussion of potential modifications to the in-crowd algorithm that could make it faster on dense problems.

Table 4.6: Running Times in Seconds for Exact Solutions of Denser Gaussian Problems

Problem	In-Crowd	Homotopy	SPGL1	FPC AS
18	4.18	20.1	2.52	1.42
19	26.7	118.5	6.69	5.08
20	75.3	361.7	33.5	13.7
21	262.1	1642.7	111.3	53.5
22	1650.1	5606.9	361.0	98.3

4.8 Computational Complexity

4.8.1 Outer Loop Complexity

Here we provide an analysis of the algorithmic complexity of the in-crowd algorithm. Step 3 dominates the complexity of the outer loop (i.e. Steps 3–10, excluding Step 6). It requires a matrix multiplication of $\mathbf{A}$ (which is $M \times N$) with the $M \times 1$ residual, requiring MN operations. A lower limit to the number of times the outer loop is run is $\lceil \frac{p}{L} \rceil + 1$, derived in Section 4.4.3. As with investigations into the number of homotopy iterations needed to find a solution [108], it is advantageous to empirically investigate the ratio of the actual number of iterations to this lower limit, henceforth denoted by $k_{out} \geq 1$. k_{out} ranged from 1.007–3.06 for all Gaussian random problems we investigated (see insets of Figures 4.3, 4.6 and 4.7) and from 2.56–6.86 for all our imaging problems (see inset of Figure 4.4). Although it is tempting to declare k_{out} to be effectively a constant, k_{out} might scale with M or N for certain types of problems, so we include it in our expression of computational complexity of the outer loop: $MN\left(\lceil \frac{pk_{out}}{L} \rceil + 1\right)$.

4.8.2 Inner Loop Complexity

The subproblem solver used in MATLAB's quadprog routine [101, 102] uses an active-set strategy that alternates between using a least-squares solver on the nonzero components of $\mathbf{x}$ and a method of determining which components should be added or subtracted to this active set. Constraints on the associated quadratic programming problem (which enforce $|x_i| \geq 0$) act on the complement of the active sets; since the problem handed to the subproblem solver is dense and with fewer than $L+1$ zero-valued components, the number of active constraints is also small and the computational cost of running the subproblem solver is dominated instead by the complexity of the iterated least-squares problem. The first iteration of this problem has a complexity of $O(q^3)$ where q is the current cardinality of I. Subsequent solutions to the least squares problem are accelerated by a Cholesky update to the initial problem as atoms enter and leave the active set, with a computational complexity $O(q^2 n)$ where n atoms are added or subtracted; often n is 1 or 2.

Assuming the size of the active set grows linearly with the number of outer iterations executed, q at iteration i is $\frac{iL}{k_{out}}$. Letting $k_{in} \geq 0$ be the number of iterations (beyond the first iteration) the subproblem solver must make times the mean n, we obtain the following expression for the total computational complexity Φ_{sub} of all operations performed by the subproblem solver:

$$\begin{aligned}
\Phi_{sub} &= \sum_{i=1}^{\lceil \frac{pk_{out}}{L} \rceil} \left(\frac{iL}{k_{out}} \right)^3 + \sum_{i=1}^{\lceil \frac{pk_{out}}{L} \rceil} \left(\frac{iL}{k_{out}} \right)^2 k_{in} \\
&= \frac{L^3}{k_{out}^3} \sum_{i=1}^{\lceil \frac{pk_{out}}{L} \rceil} i^3 + \frac{k_{in} L^2}{k_{out}^2} \sum_{i=1}^{\lceil \frac{pk_{out}}{L} \rceil} i^2 \\
&= O\left(\frac{L^3}{k_{out}^3} \left(\frac{p^4 k_{out}^4}{L^4} \right) \right) + O\left(\frac{k_{in} L^2}{k_{out}^2} \left(\frac{p^3 k_{out}^3}{L^3} \right) \right) \\
&= O\left(\frac{p^4 k_{out}}{L} \right) + O\left(\frac{p^3 k_{in} k_{out}}{L} \right) \qquad (4.7)
\end{aligned}$$

4.8.3 Overall Complexity

The total complexity Φ of the in-crowd algorithm is therefore

$$\begin{aligned}\Phi &= O\left(MN\left(\lceil\frac{pk_{out}}{L}\rceil+1\right)\right)+ \\ &\quad O\left(\frac{p^4k_{out}}{L}\right)+O\left(\frac{p^3k_{in}k_{out}}{L}\right). \end{aligned} \tag{4.8}$$

Depending on the problem characteristics, any of the three terms of Equation 4.8 can dominate. Problems with a large number of unknowns N or observations M but few nonzero components will be dominated by the first term; it is in this regime that the in-crowd algorithm performs best compared to its peers. Paradoxically, often the first term can be made *smaller* by increasing N. Its linear scaling in pN shows that if it is possible to add atoms to form an overcomplete basis in exchange for additional sparsity, total complexity will decrease. In the case for natural images [82] described by sparse atoms chosen to reflect common features, for example, increasing the number of atoms N to 1.5 times the dimensionality of the image reduces p by more than a factor of 2. The product pN therefore also decreases, and every term in Equation 4.8 becomes smaller. For the class of images that compose medical scans [69], it is conceivable that an even more overcomplete basis results in even sparser possible representations, decreasing every term in Equation 4.8, especially the second and third terms.

Very large problems with incoherent $\mathbf{A}$ matrices and high $\frac{p}{M}$ (see Section 4.7) are likely to be dominated by the second term in Equation 4.8. Incoherence predicts few false steps of the subproblem solver, thus a low k_{in}. As mentioned before, for problems with exceptionally large p an alternative in-crowd method where the Cholesky factorization is passed between subproblem solver iterations would be advantageous in that the middle term of Equation 4.8 disappears in exchange for k_{in} increasing by approximately L.

The third term of Equation 4.8 can dominate when neither p nor N is excessively large, or when special structure of the $\mathbf{A}$ matrix causes k_{in} to increase (specifically, if the subproblem solver takes many steps before finding an exact answer). For asymptotically-large problems the third term of Equation 4.8 should never dominate complexity, but in practice when $p < 15000$ both the second and the third term of Equation 4.8 can represent substantial computation.

As shown in Section 4.7, the in-crowd algorithm does not scale as well as FPC for problems with dense solutions. This weakness could be predicted from Equation 4.8, which reveals complexity terms that are cubic and quartic in p. Being interested especially in sparse problems, we selected a subproblem solver that performs well with small p, but other subproblem solvers may be more appropriate for different problem scales (see Section 4.8.5).

4.8.4 Comparison of Homotopy and In-Crowd Complexity

FPC and SPGL1 are both iterative methods, making their complexity analysis at least as difficult to determine as the number of iterations required to converge to a reasonable BPDN solution. However, homotopy's computational complexity is more accessible. Furthermore, as homotopy performs more similarly to in-crowd than other approaches across a wide range of problems, performing this analysis may provide greater insight into the relative performance of the in-crowd algorithm.

The number of steps taken by a homotopy solver is bounded below by p, and in general is often roughly proportional to p in a similar manner to the how the number of in-crowd iterations is equal to $\left(\lceil \frac{pk_{out}}{L} \rceil + 1\right)$. Each homotopy iteration involves two potentially rate-limiting steps: an inverse update requiring an $O(q^2)$ computation plus a search determining the next critical λ requiring $O(MN)$ operations. The $O(MN)$ term is not always mentioned in discussions of homotopy

complexity, but it can be seen to be necessary by considering (for example) equations 21a and 21b of [92] which compute which atoms will enter or exit the active set next. As $q < M$ and $q < N$ one might expect the second term to be always largest, however despite its favorable asymptotic scaling behavior, the $O(q^2)$ inverse update in practice often dominates computation time. Summing computational cost for $q = 1 \dots p$ and declaring k_{out} to be the number of homotopy iterations divided by p, homotopy's total complexity is

$$O\left(MNpk_{out}\right) + O\left(p^3 k_{out}\right). \tag{4.9}$$

Comparing Equations 4.8 and 4.9, one immediately sees that the complexity of in-crowd and homotopy solutions are related, but the former is a factor of L smaller given that k_{out} is similar between the two solvers, that k_{in} is small, and that the $\frac{p^4 k_{out}}{L}$ term of Equation 4.8 (derived from the initial Cholesky factorizations at the start of the subproblem solvers) does not dominate, which is true while $p < 15000$. In fact, for incoherent Gaussian problems of Section 4.6.1, the empirically-measured speed of the in-crowd algorithm was 23.75 times faster than homotopy; close to a factor of $L = 25$. This seems to indicate that choosing a larger L always yields solutions faster, however there is a limit to the benefits incurred by increasing L. When L is too high too many false steps are made, increasing k_{out} and k_{in} more than enough to negate the benefit from increased L.

4.8.5 Potential Improvements for Future Investigation

We can see several avenues for further speed improvements to the in-crowd algorithm going forward. These include:

1) Adaptively choosing the value of L and the type of subproblem solver based on the type and scale of the problem being solved,

2) Warm-starting the outer loop, the suproblem solver or both, based on the guess of a good dense solver (like SPGL1 or active set FPC) iterated only a few times; and

3) Using the fact that the theorems proving in-crowd optimality are quite permissive, such that the subproblem solver does not need to solve BPDN *per se*, as long as the final value of $f(\mathbf{x})$ is smaller than that of the initial guess, and that for all nonzeros $\{x_k\}$ in the subsolver solution, $\langle \mathbf{r}, A_k \rangle = \text{sgn}(x_k)\lambda$.

We can see four potential customizations that may accelerate the in-crowd algorithm for specific problems.

Customization 1: Other fixed or adaptive choices of L can be used.

Customization 2: Subproblem solvers can be selected on the fly based on the problem scale.

Customization 3: Subproblem solvers do not have to solve BPDN *per se*, as long as the final value of $f(\mathbf{x})$ is smaller than that of the initial guess and that for all nonzeros $\{x_k\}$ in the subsolver solution, $\langle \mathbf{r}, A_k \rangle = \text{sgn}(x_k)\lambda$.

Customization 4: The outer loop, the subproblem solver or both can be warm-started based on the guess of a good dense solver (like SPGL1 or active set FPC) iterated only a few times.

Particularly intriguing is a conjunction of Customizations 1 and 3: the outer loop could separate atoms k with a very high $|\langle \mathbf{r}, A_k \rangle|$ (which should definitely be investigated) from a second set only marginally above λ (which could be fully investigated only if the associated k_{in} turns out to be reasonable, and ignored otherwise).

Overall, there are many freedoms permitted by in-crowd optimization that we have yet to explore. The conjunction of this flexibility with the already-encouraging

numerical results presented in this paper mean that the in-crowd algorithm will be of considerable industrial and academic interest as a fast BPDN solver.

4.9 Conclusion

We have presented a new algorithm for solving BPDN which we observe to be approximately 15 times faster (see Figure 4.4 and Table 4.3) than the best available alternative method (homotopy) for the types of imaging problems we encounter. It is approximately 5 times faster than SPGL1 on large mostly-orthogonal problems (see Figure 4.3 and Table 4.2). The in-crowd algorithm performs well with a range of λ provided that λ is high enough to remove noise in the system (see Figure 4.6). We expect it to perform well for sparse, real-world, noisy, large-scale BPDN problems; therefore it may be of great usefulness to applications such as overcomplete video codecs and underdetermined model selection. Section 4.7 reveals that alternative BPDN solvers are faster on dense problems, but Section 4.8 suggests that an alternative subproblem solver that scales more gracefully with larger p may be possible. However, even without modification the in-crowd algorithm is of immediate practical utility on sparse problems, and potentially provides the groundwork for a family of specialized algorithms able to scale well for most BPDN problems with many unknowns.

4.10 Error Decay Bound

Here we will show that $f(\mathbf{x})$ strictly decreases with iteration under the in-crowd algorithm, and for arbitrary $\mathbf{y}$ and $\mathbf{A}$ where $\|A_i\|_2 = 1 \,\forall\, i$, this decrease is initially exponential.

Define the *minimum projection property* $\Theta(\mathbf{A})$ of $\mathbf{A}$:

$$\Theta(\mathbf{A}) \equiv \min_{\mathbf{z} \in \text{Span}(A_i),\, \|\mathbf{z}\|_2 = 1} \left(\max_k |\langle \mathbf{z}, A_k \rangle| \right)$$

Remark For all matrices $\mathbf{A} \neq \mathbf{0}$, $\Theta(\mathbf{A}) > 0$

This is clear by contradiction. If $\Theta(\mathbf{A}) = 0$, then there must be some $\mathbf{z}$ such that $\langle \mathbf{z}, A_i \rangle = 0 \; \forall i$. Such a $\mathbf{z}$ must then lie outside the span of $\{A_i\}$.

Remark For N x N orthonormal matrices, $\Theta(\mathbf{A}) = \frac{1}{\sqrt{N}}$, and adding additional columns to any $\mathbf{A}$ can only increase $\Theta(\mathbf{A})$. Finding $\Theta(\mathbf{A})$ in general is a non-convex problem.

With this definition in place, we have the following theorem on the convergence of the in-crowd algorithm.

Theorem 4.10.1 *The error $f(\mathbf{x})$ under the in-crowd algorithm always decreases with iteration, and converges at least exponentially in iteration count for matrices where $\|A_i\|_2 = 1$ while $\|\mathbf{r}\|_2 \geq \frac{2\lambda}{\Theta(\mathbf{A})}$ and $\|\mathbf{r}\|_2^2 \geq 2\lambda \|\mathbf{x}\|_1$.*

Proof At iteration t of the algorithm, suppose that we have a current residual $\mathbf{r}_t = \mathbf{y} - \mathbf{A}\mathbf{x}_t$. For the algorithm to step through an additional iteration, at least one new component must be added to I. This implies that there must exist some non-empty set of indices i where the usefulness $u_{t+1,i} \equiv |\langle \mathbf{r}_t, A_i \rangle|$ must be larger than λ. Let $k = \underset{i}{\text{argmax}}(u_{t+1,i})$. The optimizer has available to it the candidate solution $\mathbf{x}_t + \epsilon \mathbf{e}_k$ where $\mathbf{e}_k$ is the unit vector in the k direction. Therefore the optimizer will converge on a solution with error at most equal to $f(\mathbf{x}_t + \epsilon \mathbf{e}_k)$ for the choice of ϵ that minimizes f at the end of iteration $t+1$. Hence,

$$\begin{aligned} f(\mathbf{x}_{t+1}) &\leq f(\mathbf{x}_t + \epsilon \mathbf{e}_k) \\ &\leq \frac{1}{2} \|\mathbf{y} - \mathbf{A}(\mathbf{x}_t + \epsilon \mathbf{e}_k)\|_2^2 + \lambda \|\mathbf{x}_t + \epsilon \mathbf{e}_k\|_1 \end{aligned}$$

Using properties of the inner product,

$$\begin{aligned} f(\mathbf{x}_{t+1}) &\leq \frac{1}{2}\|\mathbf{r}_t\|_2^2 - \epsilon\langle \mathbf{r}_t, A_k\rangle + \frac{1}{2}\epsilon^2 + \lambda\|\mathbf{x}_t\|_1 + \lambda|\epsilon| \\ &\leq f(\mathbf{x}_t) + \epsilon(\lambda\,\mathrm{sgn}(\epsilon) - \langle \mathbf{r}_t, A_k\rangle) + \frac{1}{2}\epsilon^2 \end{aligned}$$

Without loss of generality[3], consider only the case $\epsilon > 0$ and $\langle \mathbf{r}_t, A_k\rangle > \lambda$. Define $\Phi(\epsilon) \equiv \epsilon(\lambda - \langle \mathbf{r}_t, A_k\rangle) + \frac{1}{2}\epsilon^2$; this represents the change to f over a single iteration of the in-crowd algorithm if error can be improved only[4] by modifying x_k. Choosing $\epsilon = (\langle \mathbf{r}_t, A_k\rangle - \lambda)$ makes $\Phi(\epsilon) = -\frac{1}{2}\epsilon^2 < 0$, so $f(\mathbf{x}_{t+1}) \leq \left(f(\mathbf{x}_t) - \frac{1}{2}\epsilon^2\right) < f(\mathbf{x}_t)$, proving the first part of Theorem 4.10.1, that f always decreases with iteration count. Solving for $\Phi(\epsilon') \leq -\frac{\|\mathbf{r}_t\|_2^2\Theta^2(\mathbf{A})}{8}$ is feasible for a range of ϵ' when the following quadratic has real roots:

$$\epsilon'^2 + 2\epsilon'(\lambda - \langle \mathbf{r}_t, A_k\rangle) + \frac{\|\mathbf{r}_t\|_2^2\Theta^2(\mathbf{A})}{4} = 0.$$

The requirement therefore is that

$$4(\lambda - |\langle \mathbf{r}_t, A_k\rangle|)^2 \geq \|\mathbf{r}_t\|_2^2\Theta^2(\mathbf{A}).$$

By the fact that the algorithm continued at Step 4, $\langle \mathbf{r}_t, A_k\rangle - \lambda > 0$, so it follows that

$$2(|\langle \mathbf{r}_t, A_k\rangle| - \lambda) \geq \|\mathbf{r}_t\|_2\Theta(\mathbf{A})$$

The choice of k implies that $|\langle \mathbf{r}_t, A_k\rangle| \geq |\langle \mathbf{r}_t, A_i\rangle|\ \forall i \neq k$. By the definition of $\Theta(\mathbf{A})$ and since $\|A_k\|_2 = 1$, there exist j such that $|\langle A_j, \mathbf{r}_t\rangle| \geq \Theta(\mathbf{A})\|\mathbf{r}_t\|_2$. It follows that $|\langle \mathbf{r}_t, A_k\rangle| \geq \Theta(\mathbf{A})\|\mathbf{r}_t\|_2$. A stricter requirement on the existence of a real ϵ' is therefore

$$\begin{aligned} 2(\Theta(\mathbf{A})\|\mathbf{r}_t\|_2 - \lambda) &\geq \|\mathbf{r}_t\|_2\Theta(\mathbf{A}) \\ \|\mathbf{r}_t\|_2 &\geq \frac{2\lambda}{\Theta(\mathbf{A})} \end{aligned}$$

[3]True since $\mathrm{sgn}(\epsilon) = \mathrm{sgn}(\langle \mathbf{r}_t, A_k\rangle)$ so $\epsilon(\lambda\,\mathrm{sgn}(\epsilon) - \langle \mathbf{r}_t, A_k\rangle)$ is always negative and equal to $-|\epsilon|(|\langle \mathbf{r}_t, A_k\rangle| - \lambda)$.

[4]This is an unlikely worst case scenario for the in-crowd algorithm, only attained when all the elements added to I are almost parallel so that only one is made nonzero, but orthogonal to the existing I such that no co-optimization with existing members of the I is possible.

which is the first condition on $\|\mathbf{r}\|_2$ of Theorem 4.10.1. As long as $\|\mathbf{r}_t\|_2 > \frac{2\lambda}{\Theta(\mathbf{A})}$, we can find an ϵ' where $\Phi(\epsilon') = -\frac{\|\mathbf{r}_t\|_2^2\Theta^2(\mathbf{A})}{8}$. Thus,

$$\begin{aligned} f(\mathbf{x}_{t+1}) &\leq f(\mathbf{x}_t) - \frac{\|\mathbf{r}_t\|_2^2\Theta^2(\mathbf{A})}{8} \\ &\leq \frac{1}{2}\|\mathbf{r}_t\|_2^2\left(1 - \frac{\Theta^2(\mathbf{A})}{4}\right) + \lambda\|\mathbf{x}_t\|_1 \end{aligned}$$

However, we desire a bound showing an exponential decrease of the total error, not just the residual imperfection. Splitting the $\left(1 - \frac{\Theta^2(\mathbf{A})}{4}\right)$ term into two equal portions,

$$f(\mathbf{x}_{t+1}) \leq \frac{1}{2}\|\mathbf{r}_t\|_2^2\left(1 - \frac{\Theta^2(\mathbf{A})}{8}\right) + \lambda\|\mathbf{x}_t\|_1 - \frac{\|\mathbf{r}_t\|_2^2\Theta^2(\mathbf{A})}{16}$$

which implies

$$f(\mathbf{x}_{t+1}) \leq f(\mathbf{x}_t)\left(1 - \frac{\Theta^2(\mathbf{A})}{8}\right)$$

when $\|\mathbf{r}\|_2^2 \geq 2\lambda\|\mathbf{x}\|_1$, which is the second condition on $\|\mathbf{r}\|_2$ of Theorem 4.10.1.

4.11 Convergence Criteria for BPDN

Prior work (for example, [109]) has shown that a convex function $g : \mathbb{R}^n \to \mathbb{R}$ attains its global minimum at $\mathbf{x}$ if and only if the zero vector $\mathbf{0}$ is an element of the subdifferential of g. For a given λ, the subdifferential of $f(\mathbf{x}) = \frac{1}{2}\|\mathbf{y}-\mathbf{A}\mathbf{x}\|_2^2+\lambda\|\mathbf{x}\|_1$ is

$$\partial f(\mathbf{x}) = -\mathbf{A}^{\mathrm{T}}(\mathbf{y} - \mathbf{A}\mathbf{x}) + \lambda\partial\|\mathbf{x}\|_1. \tag{4.10}$$

For the l_1 norm, the subdifferential is the set

$$\partial\|\mathbf{x}\|_1 = \left\{ \mathbf{v} \in \mathbb{R}^n \;\middle|\; \begin{array}{ll} v_i = 1 & x_i > 0 \\ v_i = -1 & x_i < 0 \\ v_i \in [-1, 1] & x_i = 0 \end{array} \right.$$

Let I be the support of $\mathbf{x}$. For those indices $k \in I$, the requirement that $\mathbf{0} \in \partial f(\mathbf{x})$ implies that

$$A_k^{\mathrm{T}}(\mathbf{y} - \mathbf{A}\mathbf{x}) = \langle A_k, \mathbf{r} \rangle = v_k \lambda = \mathrm{sgn}(x_k)\lambda \tag{4.11}$$

For those indices $j \in I^c$, $x_j = 0$, we have that

$$\left| A_j^{\mathrm{T}}(\mathbf{y} - \mathbf{A}\mathbf{x}) \right| = |\langle A_j, \mathbf{r} \rangle| = |v_j|\lambda \,\text{for some}\, v_j \in [-1, 1]$$

Equivalently,

$$|\langle A_j, \mathbf{r} \rangle| \leq \lambda \tag{4.12}$$

To summarize, there are two necessary and sufficient criteria for the minimizer $\mathbf{x}$ of the function $f(\mathbf{x}) = \|\mathbf{y} - \mathbf{A}\mathbf{x}\|_2^2 + \lambda\|\mathbf{x}\|_1$. On the support of $\mathbf{x}$, the correlation between the residual and the columns of $\mathbf{A}$ must equal exactly $\mathrm{sgn}(x_k)\lambda$. Off the support, the correlation must have magnitude less than or equal to λ. To show that these two criteria together are equivalent to finding the solution of Equation 4.3, consider a candidate solution $\mathbf{x}$. Since zero-valued components j have $|\frac{\partial \frac{1}{2}\|\mathbf{r}_t\|_2^2}{\partial x_j}|_{x_j=0} = |\langle \mathbf{r}, A_j \rangle| \leq \lambda$, no change in x_j for any j can result in a lower total error. All non-zero components satisfy $\langle \mathbf{r}, A_k \rangle = \mathrm{sgn}(x_k)\lambda$, thus error is locally stationary. Hence it is impossible to alter any component x_i of $\mathbf{x}$ to decrease total error. Therefore $\mathbf{x}$ is a local minimum. Since the problem is convex, the minimum is global.

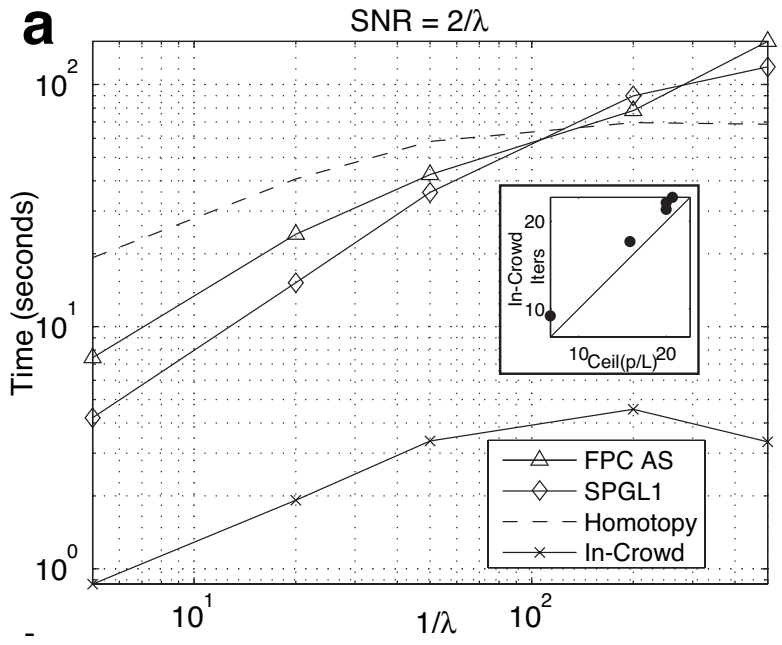

(a)

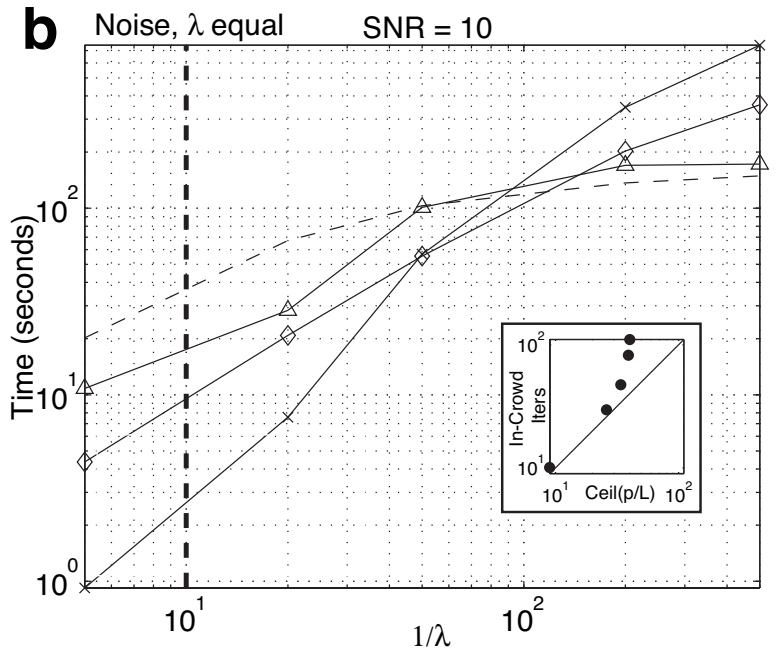

(b)

Figure 4.6: Performance of algorithms with alternative λs for Gaussian problem 14. (a) Mean running times for changing λ with the noise-to-λ ratio fixed at 0.5. Inset: mean in-crowd iteration count as a function of Ceil($\frac{\text{mean}(p)}{L}$); log scale used. (b) Mean running times for changing λ with the signal-to-noise ratio fixed at 0.1. Problems to the right of the dashed line constitute fitting noise. Inset: mean in-crowd iteration count as a function of Ceil($\frac{\text{mean}(p)}{L}$); log scale used.

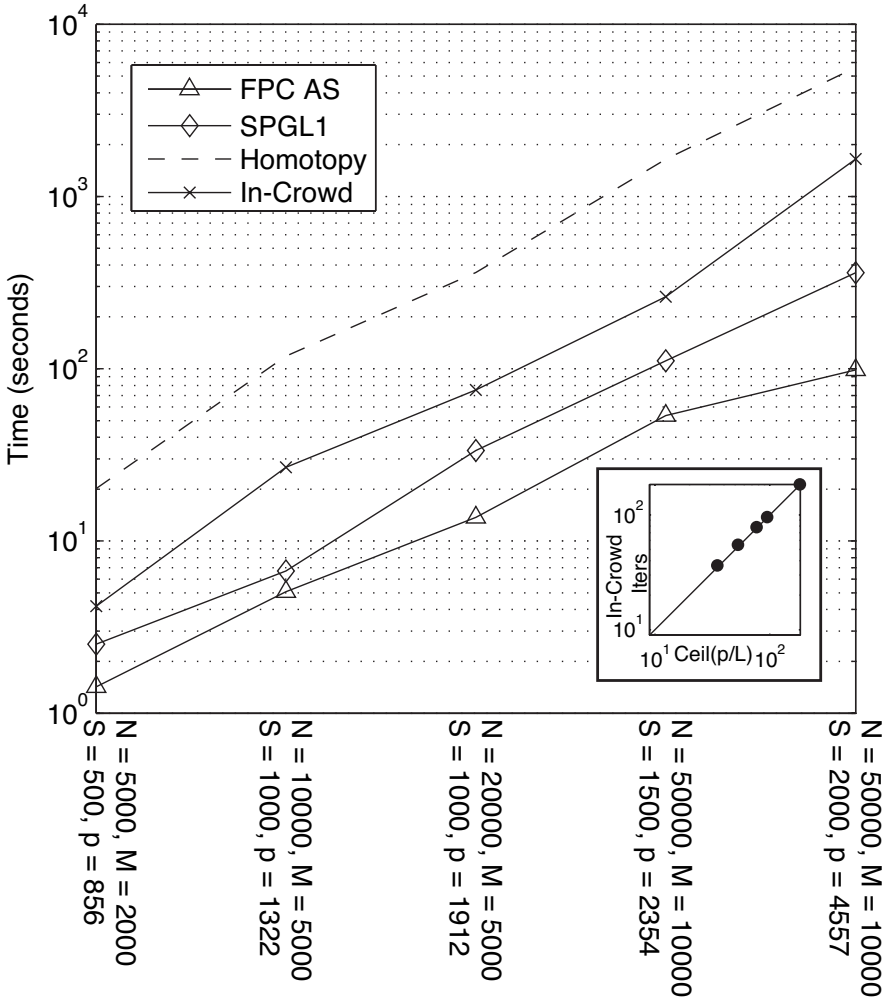

Figure 4.7: Running time for random Gaussian matrices with low-noise, dense problems. More problem details are found in Table 4.5. Inset: mean in-crowd iteration count as a function of Ceil($\frac{\text{mean}(p)}{L}$); log scale used.

Chapter 5
An angle sensitive CMOS imager

5.1 Introduction

Conventional digital cameras record light from three-dimensional scenes by capturing a 2D map of light intensity at a single plane of focus. Intensity is just one of the properties of the light rays that an image sensor might measure. Other quantities include wavelength [18], incident angle [28, 110, 111], and polarization angle. Taken together, this parameterized description of the light at the image sensor is known as the light field [1, 3]. A pixel array which can capture more information beyond intensity from the light field provides a more complete description of the scene presented to it.

This paper demonstrates an image sensor that directly records both local incident angle and intensity information from a light field. The chip is manufactured in a commodity 180nm CMOS process and performs light-field capture passively, with a single lens in ambient light. Just as the recovery of wavelength information in addition to intensity maps enabled color photographs, the additional information acquired in incident angle provides opportunities for unique digital imaging capabilities such as computational refocus and passive range measurement [110].

To date, CMOS image sensors have used a variety of active and passive approaches to acquire range information from a given visual scene. Time-of-flight (TOF) cameras calculate the time required for a reflected light pulse to traverse the distance from a laser illumination source to the image sensor [112–115]. Alternative active measurement methods for ranging, such as light-section [116] or structured light [117], analyze the distortion a scene induces in controlled illumination. Passive imaging techniques typically employ multiple integrated cameras,

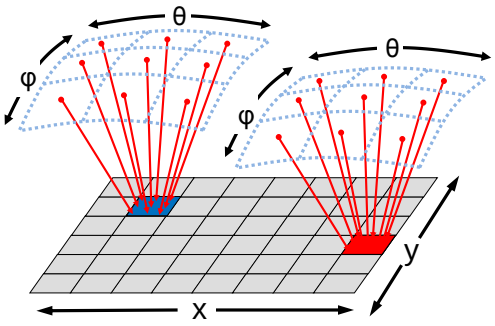

(a)

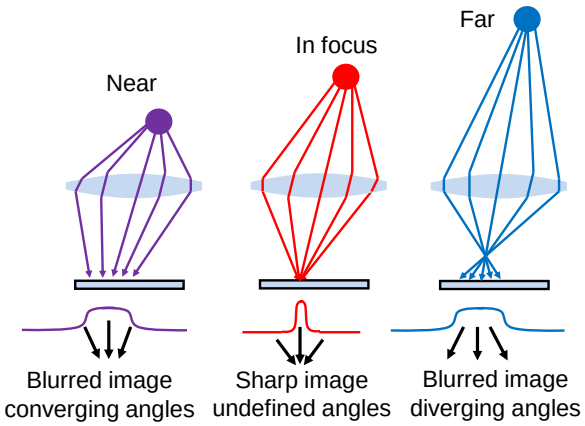

(b)

Figure 5.1: A light-field image sensor (a) measures both local incident angle and intensity. (b) Angular information in the light-field encodes information about out of focus objects.

from a pair of integrated stereo cameras [118] to the multiaperture cameras proposed by Fife et al. [63].

The relevant properties of the light field that an image sensor must capture for both post-capture rangefinding and image refocus are local incident angle and intensity (Fig. 5.1(a)). For an object that is in focus, the pixel array must capture an intensity map of the resulting image. For an object that is out of focus, the image is blurred, greatly reducing the information available from local intensity measurements. To reconstruct this information, a traditional camera requires mul-

tiple images taken at different focal lengths or locations [39]. However, as shown in Fig. 5.1(b), a blurred image has significant local angle information, which directly encodes the structure necessary to perform computational refocus and depth map computations [110]. An image sensor which captures both incident angle and intensity information therefore functions as a light-field image sensor.

In the next section, we provide some background information on the light field as well as the physical principles enabling angle-sensitive pixels [28]. In Section III, we present the design considerations for individual angle-sensitive pixels in standard CMOS manufacturing and the integration of angle-sensitive pixels into imaging systems. Next, we describe the architecture of our fabricated chip, and report on experimental results. Finally, we conclude with a discussion on the implications of this work.

5.2 Background information

5.2.1 The light field

In 1846, Michael Faraday proposed that light rays can be treated as a vector field [36]. Gershun [1] expanded this concept and defined the light field for a given point in space as the infinite collection of rays which represents the light arriving from all other points in space. Recent work in this area uses a mathematical formulation of the light field known as the "plenoptic function" [2]. This multivariate function relates light intensity to position in space (the Cartesian coordinates x, y, and z), direction of arrival (the solid angles θ and ϕ), wavelength (λ), polarization angle (ψ), and time (t). Characterization of this function for a given visual scene provides a complete representation of the scene.

Recording the light field is useful for a number of applications, as it provides

much more information than a conventional photograph or movie. Acquiring both the spatial and angular components of the plenoptic function is particularly important, as it permits post-capture computational construction of images at synthetic focal depths [34,40]. Furthermore, it allows for the extraction of information about the three-dimensional structure of a scene [119] and prediction of illumination patterns ("light field rendering") [4].

Unfortunately, fully measuring the plenoptic function for any non-trivial scene is impossible. No observer can measure the intensity of all rays at every point in space, much less for all time and all wavelengths. All practical imaging methods only sample a portion of the light field. A photograph generated by a monochrome CMOS pixel array represents a 2D slice of the plenoptic function, $I(x, y)$ at a fixed z and t and for an average θ, ϕ, ψ, and λ. A color image sensor adds another dimension to the captured slice, $I(x, y, \lambda)$.

Several techniques have been developed to improve light field sampling by recording local distributions of angle from the light field. The simplest method, proposed by Adelson, uses an array of pinhole cameras [37]. Each individual camera captures the angle-dependent intensity $I(\theta, \phi)$ at a particular location in space. Placing the cameras at different positions (x_i, y_i) takes a 4D slice of the plenoptic function, $I(x, y, \theta, \phi)$. Arrays of conventional cameras have also been used [38], along with camera scanning [40] and specialized aperture masks [41, 120]. Chip-scale solutions have proposed using microlenses to emulate these camera arrays [42].

All of these existing approaches to acquire information about local angle require either multiple external optics or mechanical systems for moving optical components. The additional cost and complexity required has largely relegated light-field imaging to laboratory settings. Integrating local angle measurement into CMOS digital image sensors will drastically simplify these light-field imaging systems.

Here we present such a digital light-field imager which relies on the Talbot effect.

5.2.2 The Talbot effect

First observed by Henry Fox Talbot in 1836, the Talbot effect describes the "self-imaging" property of periodic objects such as diffraction gratings [35]. Illumination of a grating with a plane wave normal to its surface generates periodic intensity patterns, known as self-images, at uniformly spaced distances behind the grating (Fig. 5.2(a)). The observed intensity patterns have identical periodicity to the diffraction grating. Lord Rayleigh [44] demonstrated that this effect was a consequence of Fresnel diffraction and that the self-images are observed at half-integer multiples of the Talbot depth $z_t = 2d^2/\lambda$, where d is the grating period and λ is the light wavelength.

More recent work has shown that the self-images of the Talbot effect respond to incident angle. This sensitivity is known as the off-axis Talbot effect [56]. For macroscale gratings (where $d \gg \lambda$), self-imaging occurs at multiples of the distance $z = z_t \cos^3(\theta)$, where θ is the angle of incident light. In addition, the periodic self-images shift laterally by a distance $\Delta x = z \tan(\theta)$ in a direction perpendicular to the grating.

When several individual light sources illuminate a single grating, each source generates its own set of self-images at a characteristic depth and lateral shift dependent on the incident angle. Assuming that the dielectric surrounding the grating is linear and angles are small, the independent self-images superimpose to form a single image. The brightness of the superimposed image encodes the magnitude of illumination, while the lateral shift of the self-image encodes information on the incident angle of light rays.

Therefore, we have used the Talbot effect to build an image sensor which mea-

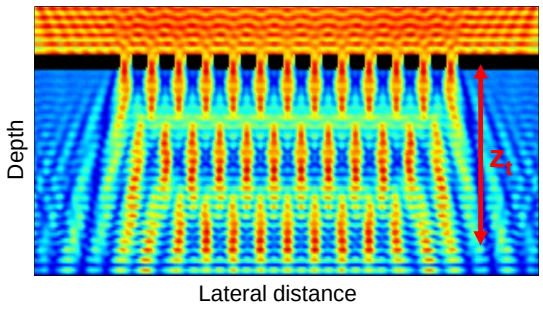

(a)

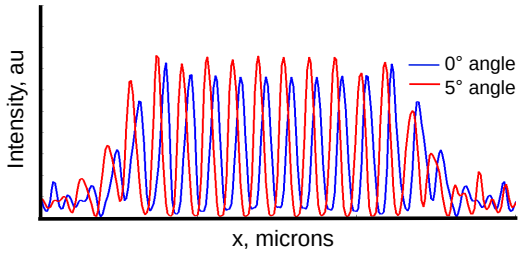

(b)

Figure 5.2: Illustration of the Talbot effect. (a) FDTD simulation. (b) Intensity peaks shift laterally in response to changes in incident angle.

sures information about the intensity and incident angle of the light striking it. Each pixel of this image sensor will contain a diffraction grating and a means of characterizing the self-images it generates. We term these pixels "angle sensitive pixels" as they respond to both incident intensity and incident angle [28]. An array of these pixels are able to directly sample a 4D slice of the plenoptic function, without any additional parallel or moveable optics.

5.3 Angle sensitive pixels

5.3.1 Pixel design

To achieve a spatial resolution comparable with existing image sensors, an angle sensitive pixel must have a pitch of only a few microns. As several periods of the diffraction grating are necessary for self-image formation, the grating itself must have a pitch of only a few wavelengths. We have used numerical modeling and simulation to analyze diffraction effects on these small length scales. Finite difference time domain (FDTD) simulations show that Talbot-like self-images still form for a micron-pitch grating and that these periodic intensity patterns exhibit a lateral shift in response to incident angle (Fig. 5.2(b)). These simulations have assumed a linear, isotropic, homogenous dielectric and infinite gratings of perfect metal conductors under monochromatic plane illumination. Although this neglects the thin barrier layers of TiN associated with backend interconnect deposition and complex oxynitride passivation cap, our previous experience is that a simplified optical model is sufficient for angle-sensitive pixel design [28].

Fortunately, modern CMOS manufacturing easily achieves sub-micron resolution, and we can use metal interconnect layers to integrate high density diffraction gratings into the individual pixels of an image sensor. Furthermore, these gratings embedded in back-end of line dielectric achieve Talbot depths on the scale of the layer stack. As an example, we consider illuminating a 1μm pitch grating with green light (wavelength $\lambda = 532$nm in vacuum). If the grating is embedded in a matrix of silicon dioxide dielectric (refractive index $n \approx 1.46$, yielding an effective wavelength of $\lambda = 364$nm), the characteristic Talbot depth is 5.50μm. Based on classical diffraction theory, strong periodic intensity patterns will occur at multiples of 2.75μm. This lets us integrate structures to analyze the self-images on-chip

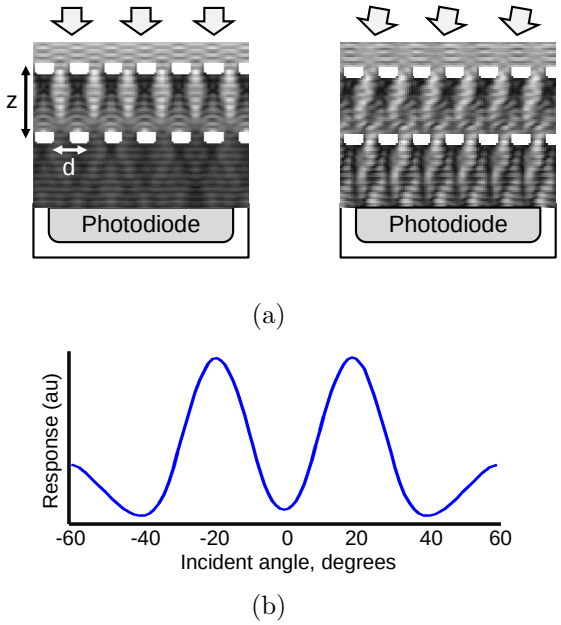

Figure 5.3: Structure of an angle-sensitive pixel. (a) For different incident angles, the analyzer grating passes or blocks light to the photodiode, generating (b) a periodic response to incident angle.

as well.

Previous work studying macro-scale Talbot effects (where grating pitch $d \gg \lambda$) placed a CCD array behind the grating at the Talbot depth and directly imaged the resulting intensity patterns [54]. One approach to developing an angle-sensitive pixel is to miniaturize this arrangement, using a small sub-imager array for each micro-scale grating. This approach has two primary disadvantages. First, an array of these pixels would generate a large amount of data which requires complex processing to extract information on local angle. Second, the required sub-imager array must have pixels of 1/2 the grating pitch in order to resolve the Talbot image. Although previous work has demonstrated pixel-scale sub-imager arrays in a 0.11μm CCD process [59], carrier diffusion effects typically limit their true resolution to 1μm or worse.

Instead, as shown in Fig. 5.3(a), we add a second diffraction grating behind

the first at a depth where strong periodic intensity patterns form: half-integer multiples of the Talbot depth [28]. We term this second grating an "analyzer grating" and have implemented it in metal interconnect as well. As the incident angle of light changes, the intensity patterns generated by the first grating shift relative to the analyzer grating. When the intensity patterns align with the gaps of the analyzer grating, the total light flux passed by the two gratings is high. When the intensity patterns align with the bars of the analyzer grating, little light passes through. Measuring the total light flux with a single photodiode below the analyzer grating, we recover the alignment of the self-image and therefore an angle-sensitive response.

The photodiode placed behind the two gratings measures a periodic response to incident angle (Fig. 5.3(b)). This response I can be approximated as a function of the incident angle θ and intensity I_o by the relation

$$I = I_o(1 + m\cos(\beta\theta + \alpha)) \tag{5.1}$$

where m, α, and β are parameters dependent on the geometry of the grating pair. Modulation depth m is a measure of the strength of the incident-angle dependent behavior: lower m implies less angle selectivity. The coefficient β defines an angular sensitivity, or sensitivity of the response to small changes in incident angle. α defines which angle results in a peak photodetector response and depends on the lateral offset between diffraction and analyzer gratings.

Both the modulation depth m and the angular sensitivity β control how angular information influences the output of an angle-sensitive pixel. A good optical design will maximize m, because a larger m results in a pixel which responds more strongly to incident angle. For a given vertical separation z between primary and analyzer grating, m is proportional to $\cos(2\pi z/z_t)$, where z_t is the characteristic Talbot depth for the primary grating. Optimal designs place the analyzer grating at

depths where strong self-imaging behavior occurs, namely at separation distances $z = \frac{N}{2} z_t = Nd^2/\lambda_{\text{des}}$, where N is a positive integer, d is the grating pitch, and λ_{des} is the design wavelength in back-end dielectric. The separation depth z and grating pitch d additionally determine the angular sensitivity $\beta = 2\pi z/nd$, where n is the index of refraction of the bulk dielectric. Available inter-layer spacings in a given manufacturing process establish constraints on possible choices of z and consequently grating pitch and angular gain for angle-sensitive pixels with large values of m.

Manufacturing variability in interconnect geometry is also a critical constraint on angle-sensitive pixel design, in particular on the choice of integer N. Sources of variation include the inter-grating dielectric thickness z, grating pitch d, inter-grating alignment, and grating wire width. Each of these can potentially influence one or more of the parameters in Eq. 5.1. Errors in grating alignment will primarily result in changes to the phase offset α. Such errors are expected to be small, as large deviations would lead to back-end connectivity failures, and can be corrected using the full quadrature information available from a set of four angle-sensitive pixels, described below. Variation in line width, such as that caused by nonuniformity in dielectric etch rates, does not alter the actual pitch of the grating, but does affect the strength of the generated diffraction pattern and therefore the strength of angular response m. Based on simulation results, the percentage variation in m is approximately 70% that of the width variation. In contrast to grating offset and wire width errors, deviations in wiring pitch d, or the center-to-center spacing of the wires in the gratings, will directly influence the Talbot depth z_t. Changes in this depth will inversely affect the angular sensitivity β and degrade the modulation depth m. Similarly, variation in inter-layer dielectric thickness z also directly influence β and m.

The most critical consequence of process variation is degradation of the modulation depth m of Eq. 5.1, since sufficiently small m implies a loss of angular sensitivity. A reasonable design goal is to achieve no more than a 30% degradation in modulation depth from the optimum design, when the vertical separation z between the two gratings is equal to $\frac{N}{2}z_t$. Because modulation m is proportional to a cosine function of this vertical separation, the maximum absolute variation in vertical separation which achieves 0.7 of the optimum is $|\Delta z| = z_t/8$. The permissible relative tolerance in vertical inter-layer spacing from the optimum which satisfies our design goals is therefore $\Delta z/z = 1/4N$. Similar analysis results in a permissible tolerance in wiring pitch of $\Delta d/d = 1/8N$. The chemical-mechanical polishing used to create aluminum interconnect layers is known to generate significant intermetal oxide thickness variation [121], so we have only chosen robust angle-sensitive pixel designs where N is low (1 or 2) for our image sensor.

5.3.2 Ambiguity resolution

The response of an angle-sensitive pixel depends on both the overall brightness and incident angle. As a result, the output of a single pixel cannot distinguish between a bright source at an angle blocked by the analyzer grating and a dim source at an angle passed by the analyzer grating. This ambiguity can be resolved with a pair of complementary responses in which the parameters m and β are equal (Fig. 5.4(a)). The difference between the two responses contains information on incident angle, while the sum encodes incident intensity.

The required complementary response, with $\alpha = \pi$, is achieved by laterally shifting the analyzer grating by 1/2 a period relative to the diffraction grating. We also implement a pair of complementary quadrature responses, where $\alpha = \pi/2$ and $\alpha = 3\pi/2$ to better characterize the periodic relationship between incident

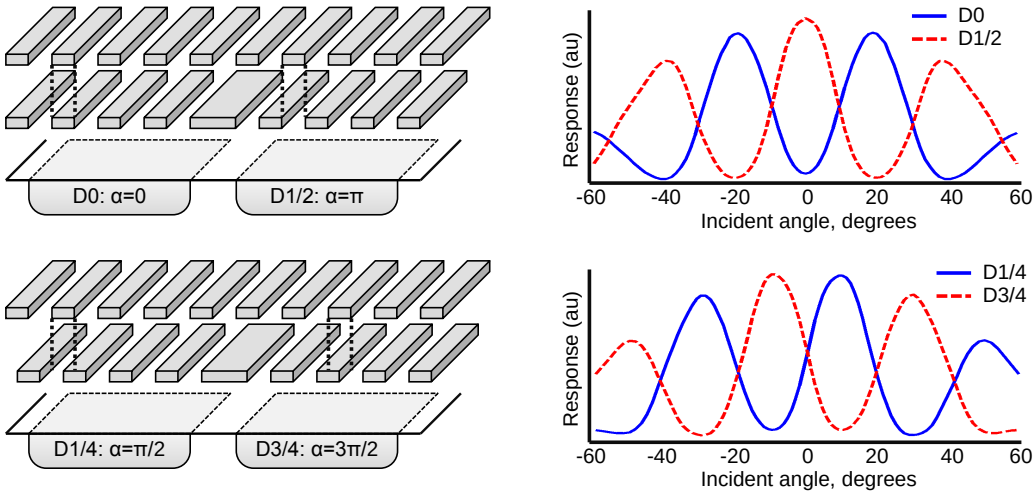

(a) (b)

Figure 5.4: (a) Pairs of complementary angle-sensitive pixels. (b) Simulated responses of depicted pairs of complementary angle-sensitive pixels.

angle and pixel response. These quadrature responses result from similar shifts of the analyzer grating of 1/4 period as shown in Fig. 5.4(a).

We treat these four pixel responses as two differential signal pairs, where the differential mode encodes angle (specifically $\cos(\beta\theta)$ and $\sin(\beta\theta)$) and the common mode represents intensity (Fig. 5.4(b)). Although four pixels are necessary to faithfully extract information about local incident angle, this is a reasonable design compromise. When objects are in focus, light arrives at the pixels of the image sensor from a wide range of angles, and each individual angle-sensitive pixel functions as a typical image sensor pixel with no loss of spatial resolution. When objects are out of focus, image blurring results in large correlations in local intensity but inhomogeneous angle, and angular information becomes more useful than densely spaced intensity-sensitive pixels.

Using complementary pairs of angle-sensitive pixels resolves the ambiguity between local intensity and local incident angle. However, the intrinsic periodicity

of response to incident angle introduces a second ambiguity which sets limits on the range of identifiable incident angles. The parameter β controls this periodicity, while also setting the "gain" of an angle-sensitive pixel. High values of β provide good sensitivity to small changes in incident angle, but decrease the range of angles we can unambiguously identify. In contrast, low values of β widen the range of resolvable incident angles, but at a cost to angular sensitivity.

We avoid this design tradeoff by using an array containing angle-sensitive pixels with different β parameters. By using multiple β values, we compensate for weaknesses of individual periodic response curves. High β pixel responses provide us with the ability to discriminate fine gradients in incident angle. Low β pixel responses provide coarse directionality. As each β needs its own set of four pixel responses, the resulting angle-sensitive pixel array requires a complex mosaic pattern of angular filters, reminiscent of the Bayer filters used in color image sensors.

5.4 System architecture

5.4.1 Angle-sensitive pixel array

The fabricated chip contains 153,600 pixels, arranged as a 48x50 tiling of subunits composed of 64 distinct angle-sensitive pixels (Fig. 5.5(a)). The tiled subunit measures 60μm on a side, for an active imager area measuring 2.88mm by 3mm. Each individual angle-sensitive pixel is 7.5μm on a side and contains a pair of diffraction gratings for angle sensitivity placed above a conventional 3-transistor active CMOS pixel. An example pixel layout is shown in Fig. 5.6. The pixels employ a n-well/p-substrate photodiode measuring 6.1μm by 5.2μm in size, resulting in an effective fill factor of 56% and an integration capacitance of 20fF, computed from pixel layout. All pixel transistors are regular V_{th} devices, and operate from a 1.8V

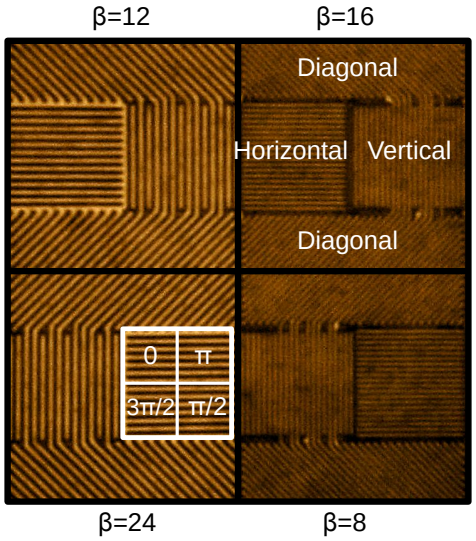

(a)

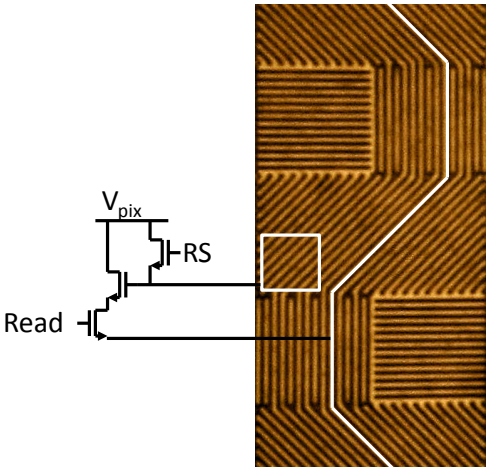

(b)

Figure 5.5: Microphotograph of (a) one full angle sensitive pixel tile with multiple orientations, β and α values. (b) Gratings function as routing buses.

supply. The output swing from each pixel is 600mV, corresponding to a full scale signal charge of 75,000 electrons.

Blocks of four angle-sensitive pixels, each with distinct analyzer grating offsets, work together to provide a good characterization of local incident angle along a

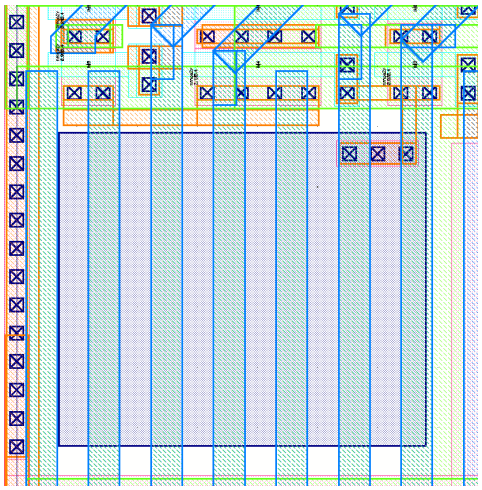

Figure 5.6: Example layout of an angle-sensitive pixel.

given axis. To minimize undesired edge effects which result from finite diffraction gratings, each block of four pixels shares one single diffraction grating responsible for generation of Talbot self-images. Below the shared grating, the individual pixels have unique offsets in their analyzer gratings to provide the desired angle responsivity curves.

The tiled subunit contains 16 such blocks of angle-sensitive pixels. These blocks are divided into four groups based on the orientation of the primary and analyzer gratings. Two groups have gratings aligned perpendicularly to each other, and the remaining two groups have the same gratings rotated by $\pm 45°$. As the off-axis Talbot effect only responds in a direction perpendicular to grating orientation, a particular angle-sensitive pixel only responds to changes in incident angle along one axis. We employ multiple grating orientations to characterize the solid angles of elevation and azimuth and to reduce spatial ambiguity further. For each orientation, angle-sensitive pixels with four values of simulated β: 9.1, 13.5, 18.4, and 25.1, measure both large and small gradients of incident angle. We achieve these angular gains by using three different inter-metallization spacings and two

Table 5.1: Fabricated angle-sensitive pixel types

Design	Grating pitch	Metal layers	Pred. $\beta = \frac{2\pi z}{nd}$	Meas. β	Meas. m
1	0.72μm	M5-M4	8.2	7.6	0.28
2	1.04μm	M5-M3	11.4	13.1	0.51
3	0.72μm	M5-M3	16.5	15.9	0.35
4	1.04μm	M5-M1	22.8	24.5	0.44

different grating pitches, as shown in Table 5.1.

All local diffraction gratings for the angle-sensitive pixels are implemented in the back-end metallization layers. By careful choice of grating pitch and orientation, the bars forming the diffraction gratings also serve as readout bus lines (Fig. 5.5(b)). This double usage lets us simultaneously route 16 pixel signals to the readout backend from each 64 pixel tile in one read operation. The 16-lane pixel bus is split into two channels, each sampling four phases of angle-sensitive pixel, for two orientations and a single selected β.

5.4.2 Readout and digitization

The integrated mixed-signal backend, shown in Fig. 5.7, specifically handles the mixture of intensity and angle information measured by angle-sensitive pixel array. Column-parallel sample and hold circuits acquire the individual pixel outputs for amplification and re-encoding through 192 column-parallel programmable gain amplifiers. Each amplifier computes the sum and difference of complementary pairs of angle-sensitive pixel responses and provides independent, selectable gain for the two resulting signals. This operation separates the intensity information encoded in the sum from the angle information encoded in the difference. Column-parallel algorithmic analog-to-digital converters read the amplifier outputs, and the resulting digital values are sent off-chip through 24 serial channels. Global timing control drives both a programmable rolling shutter and readout backend operations. To

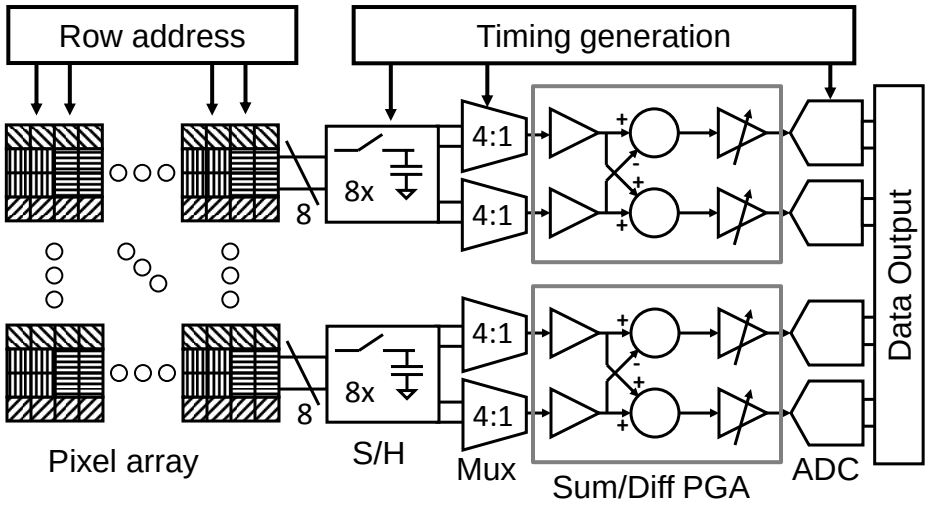

Figure 5.7: Block diagram of manufactured chip.

help confirm basic optical function, we included a global multiplexer which lets us directly measure the responses of single angle-sensitive pixels.

Two channels of the backend operate on the 16 pixel outputs generated by a 64-pixel tiled subunit in every read operation. Each channel first samples 8 signals from four pairs of complementary angle-sensitive pixels (each pair share identical β and orientation but have α's different by π). The sampled voltages are multiplexed one complementary pair at a time onto one column-parallel amplifier. Each column-parallel amplifier, shown schematically in Fig. 5.8(a), first converts individual pixel output voltages into differential current-mode signals by using degenerated differential pairs and a global reference voltage. Recombination of the resulting current-mode signals in the current domain results in a pair of signals which separately represent the intensity and incident angle information (Fig. 5.8(b)). For testability, an alternate mode of operation disables the recombination operations and leaves the individual pixel outputs unchanged. Resistive loads, configured as part of a standard common-mode feedback biasing scheme translate

the signal currents into voltages for subsequent digitization. To account for differences in relative strength between intensity and angle information, the resistors for these paths are separately programmable to make best use of the available full-scale range of the downstream ADC's. The gain steps are binary weighted, with a minimum of 1 and a maximum of 16.

A two-stage algorithmic 10 bit analog-to-digital converter based on capacitive charge pumps [122] performs digitization of the amplified signals. The algorithmic architecture was chosen for maximum compactness, enabling column-parallel integration. Each gain stage of the converter operates on a differential input and relies on charge redistribution to realize the required voltage gain. Source followers provide buffering to the next gain stage. Each stage operates with a sub-binary radix (G = 1.8) to alleviate the effects of device mismatch. As a result, twelve conversions are necessary to obtain the 1000 levels necessary for 10 bit resolution.

The complete ADC is shown in Fig. 5.9(a). It comprises 20 single transistor switches, 8 capacitors ($C_1 = C_2 = 200$fF, $C_r = 50$fF sets the sub-binary radix), 4 NMOS source followers and a single shared comparator, for a total area of 2400 square microns per converter. All clock signals (Fig. 5.9(b)) for switches and comparator operation are generated globally and shared across ADCs, with local retiming to avoid errors due to skew.

Operation of the converter alternates between the two gain stages. Initially, the shared comparator is connected to the first stage and compares $V_{\mathrm{in,p}}$ to $V_{\mathrm{in,n}}$. The result provides the first digitized bit and sets the polarity of the reference voltages $V_{\mathrm{ref,p}}$ and $V_{\mathrm{ref,n}}$ Next, the clock signal $\phi_{1,\mathrm{s}}$ samples the differential input voltage onto capacitors $C_{1,\mathrm{p}}$ and $C_{1,\mathrm{n}}$. Bringing the clock signal $\phi_{1,\mathrm{s}}$ low and asserting $\phi_{1,\mathrm{r}}$ disconnects the input voltage from the sampling capacitors and drives one plate each of $C_{1,\mathrm{p}}$ and $C_{1,\mathrm{n}}$ to the reference voltages. Redistribution of charge at nodes

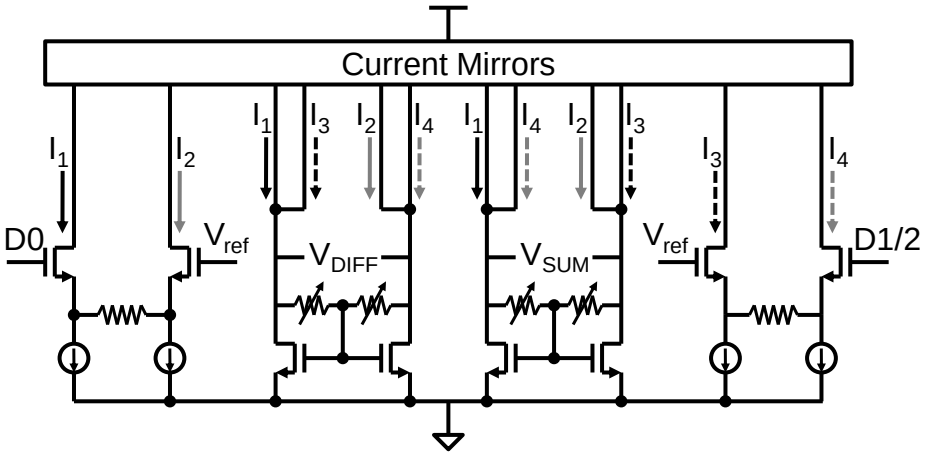

(a)

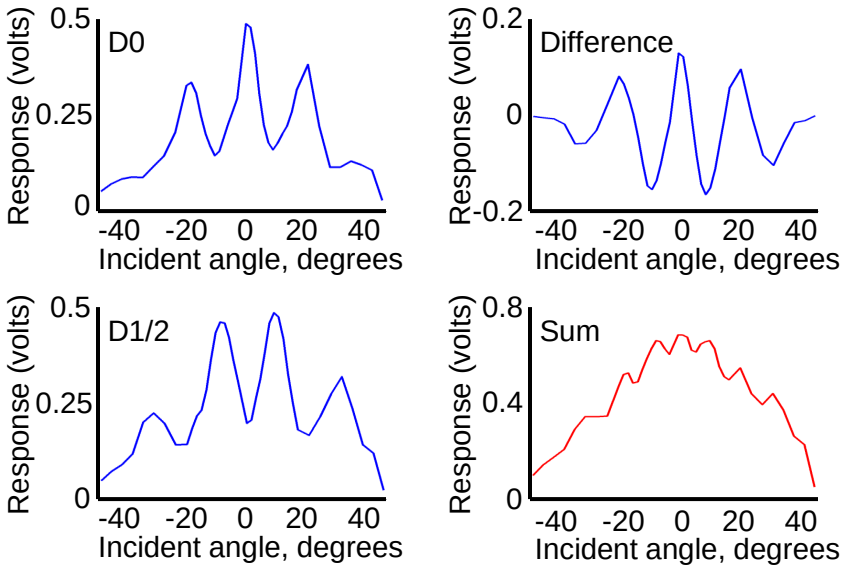

(b)

Figure 5.8: Readout amplifier computes sum and difference from complementary angle-sensitive pixel responses. (a) Simplified readout amplifier schematic. Degenerated differential pairs convert angle-sensitive pixel outputs (D0 and D1/2) to differential currents (I_1 to I_4). A set of current mirrors copies these signal currents, which are then combined to perform the sum and difference operations. Programmable resistive loads with common-mode feedback convert the currents back into voltages for digitization. (b) Sum and difference calculated from measured responses with identical gain settings.

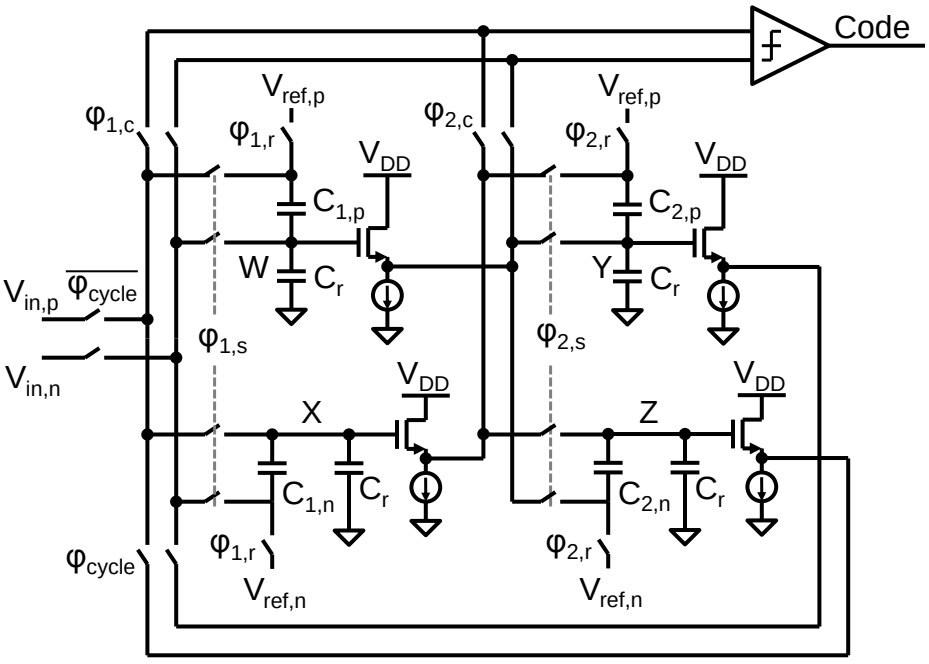

(a)

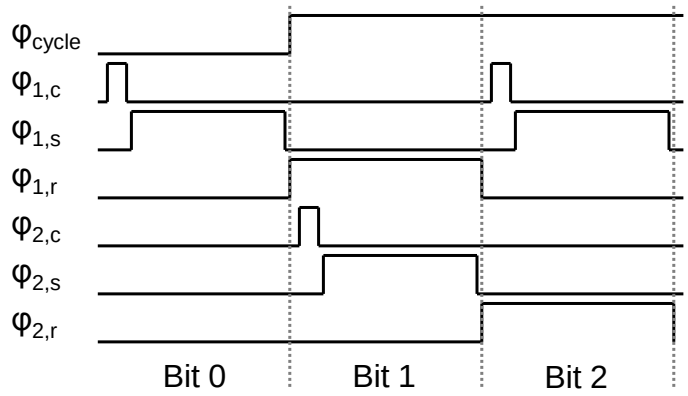

(b)

Figure 5.9: (a) Schematic of charge-pump based algorithmic ADC which provides a compact differential ADC for digitization. (b) Timing diagram of main ADC control waveforms.

W and X drives the differential output voltage to $V_X - V_W = 1.8\,(V_{\mathrm{in,p}} - V_{\mathrm{in,n}}) - 0.8\,(V_{\mathrm{ref,p}} - V_{\mathrm{ref,n}})$. The additional pair of capacitors $\mathrm{C_r}$ control the stage gain and therefore the conversion radix. When $\mathrm{C_r}$ =$\mathrm{C_1}/4$, charge balance results in the desired radix of 1.8.

The source followers buffer the resulting node voltages to the second stage, which uses the shared comparator to compare V_W and V_X and to set the second digital bit. As with the first stage, the clock $\phi_{2,\mathrm{s}}$ samples the voltages V_W and V_X onto capacitors $C_{2,\mathrm{p}}$ and $C_{2,\mathrm{n}}$. The clock $\phi_{2,\mathrm{r}}$ controls charge redistribution of the second stage and drives its outputs to cycle back to the first stage for the next bit of conversion. After six full cycles, the converter provides the final 12 bit output.

With an input 250mV peak-to-peak 10kHz sine wave and the amplifier configured to provide a gain of 4 (resulting in a 1Vpp full scale ADC input), the complete readout backend provides a SNDR of 53.6dB (8.6 ENOB) and a SFDR of 63dB at an ADC sample rate of 400kS/s. Measured DNL with an input 250mV ramp and identical amplifier gain setting was under 3 LSB's at the 10b level for the same sample rate. Manufactured in a mixed-mode/RF TSMC 180nm process, the chip measures 20 square millimeters and consumes 80mA from a 1.8V supply at an image capture rate of 200 frames per second. A micrograph of the die is shown in Fig. 5.10.

5.5 Results

5.5.1 Basic angle sensitive-pixel behavior

We confirmed basic angle-sensitive pixel functionality by configuring the image sensor in a testing mode using the global multiplexer. The outputs of individual pixels were recorded while a 520nm light source (provided by a commercial green

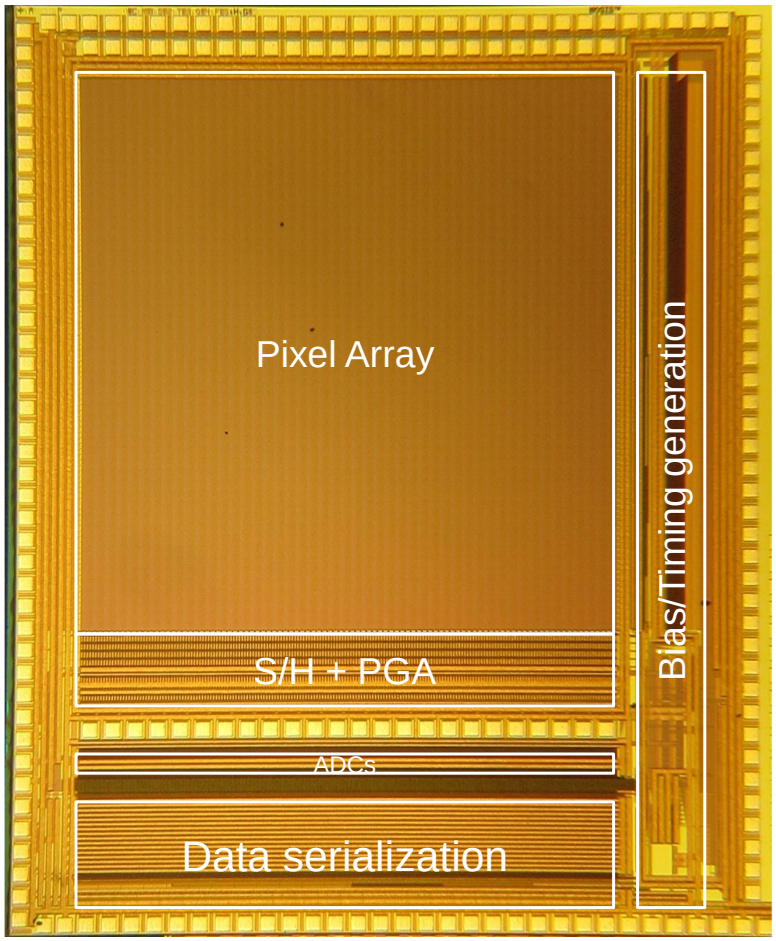

Figure 5.10: Chip microphotograph. The die area is 20mm^2.

light-emitting diode) swept through incident angle. Figure 5.11 compares the measured and simulated responses for one set of angle-sensitive pixels with gratings aligned orthogonally to the angle sweep. Figure 5.12 shows the differences between outputs from the pixels for the four designs with distinct angular sensitivities (β parameter of Eq. 5.1). We observed periodic responses for the different β designs close to those predicted in simulation as incident angle changed. Measured β values and simulated β values are provided in Table 5.1.

For pixels with gratings aligned parallel to the direction of the incident angle sweep, we observed essentially no angle sensitivity aside from the overall envelope

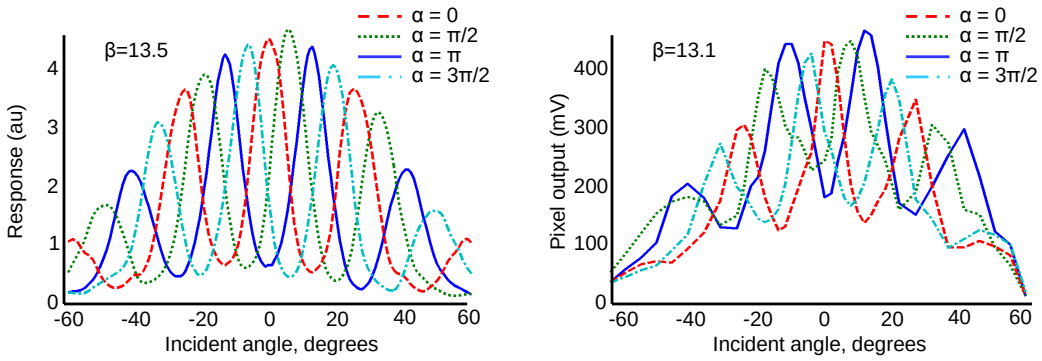

(a) (b)

Figure 5.11: Comparison between simulated(a) and measured(b) responses for four angle-sensitive pixels with identical angular sensitivity β but distinct phase offsets α.

function exhibited by all pixels. Pixels with gratings aligned diagonally to the incident angle sweep exhibited reduced periodicity, with an apparent angular gain 0.7 times that of pixels with orthogonally aligned gratings. This reduction factor is the result of a 45 degree projection of the swept angle onto the gratings. Of the 4 distinct designs, the $\beta = 7.6$ devices show the least ideal responses with the lowest measured modulation depth (m parameter of Eq. 5.1) values. We believe this is due to the narrow vertical separation between their gratings, which are implemented in adjacent metal layers, such that z/z_t is the least well controlled. Overall, the primary difference between measured and simulated responses of our angle-sensitive pixels is reduced modulation depth, likely the result of manufacturing variability, the complex passivation stack and finite grating effects. Nonetheless, all designed pixels show clear angle responses.

As the Talbot effect is a diffractive phenomenon, we expected the wavelength of incident light to influence the angle sensitivity of our pixels. To investigate the importance of this effect, we also conducted sweeps of incident angle with 470nm and 590nm light sources (provided by commercial blue and yellow LED devices).

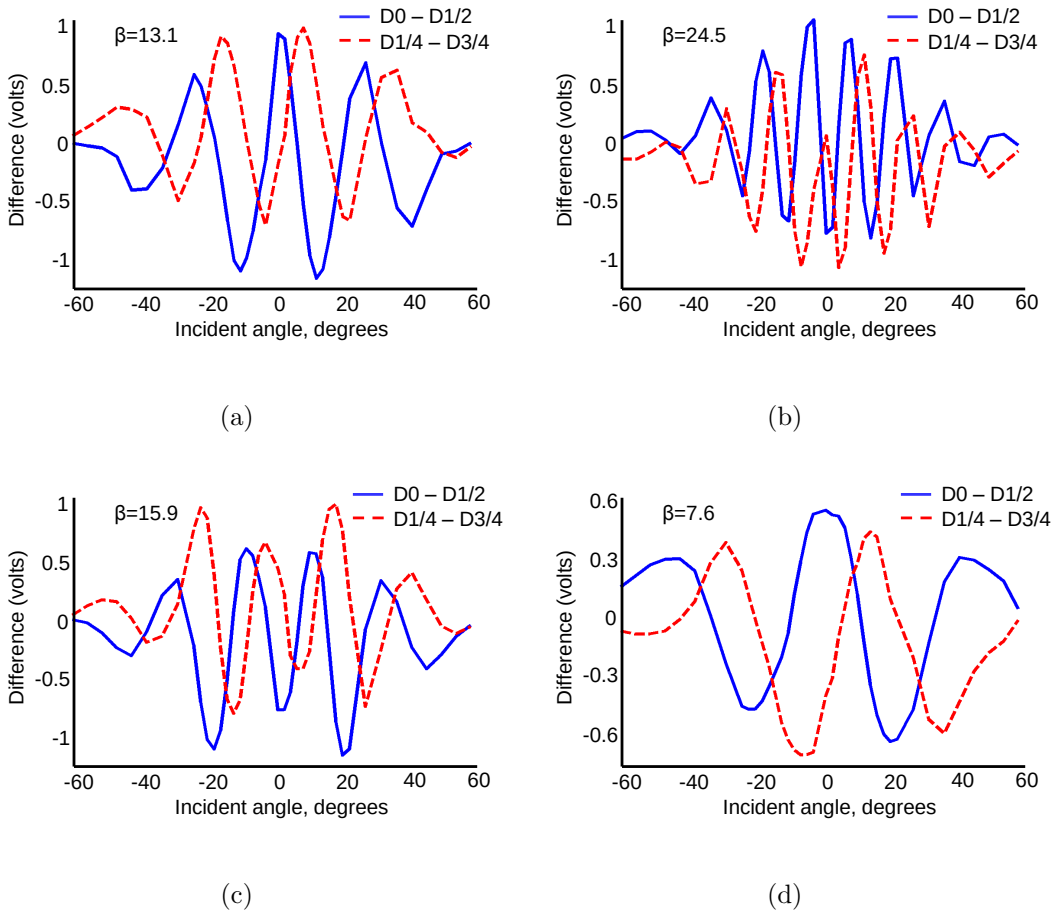

Figure 5.12: Measured differences for complementary pairs of angle-sensitive pixels with different β values, $\lambda = 520$nm.

The differences between pixel outputs are plotted in Fig. 5.13. Changing the wavelength of incident light relative to the design wavelength of 520nm results in response curves with reduced m, indicating a degradation in the quality of angular response. Nevertheless, overall angular sensitivity is preserved, and the angular gain β is not appreciably affected. Both of these observations are in agreement with the design equations presented above and previous work [28]. Based on the relative insensitivity of pixel responses to changes in wavelength, we performed all imaging tests under white light illumination also provided by LEDs.

As the metal diffraction gratings reflect much of the incident light, we expected

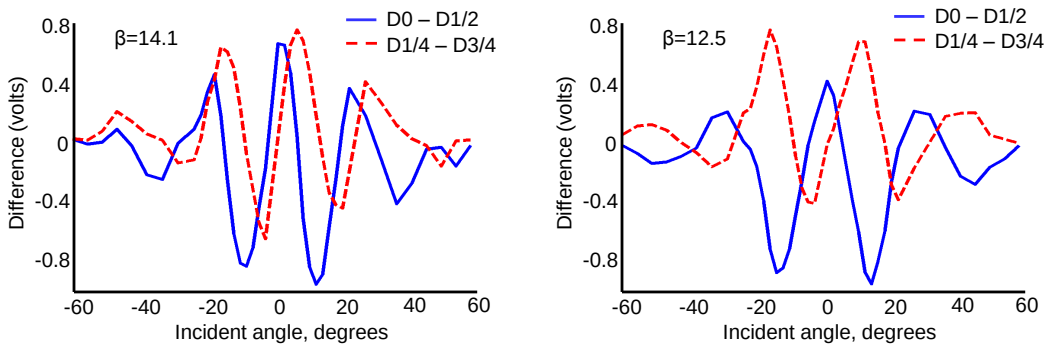

(a) (b)

Figure 5.13: Changing the wavelength of incident light has little effect on overall angle sensitivity, but weakens the strength of response. (a) $\lambda = 470$nm. Measured $\beta = 14.1$ and $m = 0.40$. (b) $\lambda = 590$nm. Measured $\beta = 12.5$ and $m = 0.32$.

angle-sensitive pixels to have reduced sensitivity compared to conventional CMOS active pixels. Comparing the measured sensitivity of an active CMOS pixel with gratings to that of a identical active CMOS pixel without gratings, the diffractive structure reduces sensitivity by a factor of 6 to 8, depending on the grating pitch. This sensitivity reduction is weakly dependent on wavelength, with a slight increase in sensitivity (less than 20%) at longer (redder) wavelengths. The observed effect of the gratings on color response may be related to diffractive effects such as the Rayleigh-Wood anomaly [123, 124] or the plasmonic extraordinary optical transmission effects observed by Ebbesen [125, 126].

5.5.2 Imaging results

In order to demonstrate the capabilities of this angle-sensitive pixel based image sensor, we created a light field camera by placing the imager behind a commercial fixed-focus camera lens (Nikkor 50mm f/1.8 Ai-S). Target objects were placed at a distance of one meter, and we adjusted the focal plane of the lens for different imaging tests. For all tests, we used the maximum aperture opening of F#=1.8.

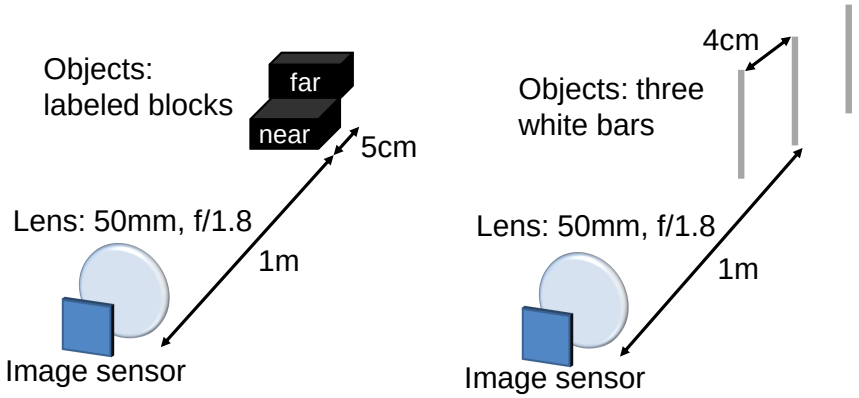

(a) (b)

Figure 5.14: Illustration of imaging tests. (a) Blocks labeled near and far used to test computational refocus. (b) Three white bars arranged at different depths used to test rangefinding.

The imaging tasks of Fig. 5.14 were designed to demonstrate that the camera system captures sufficient light-field information to enable post-capture synthetic refocusing and depth mapping.

As a first test, we placed two blocks (labeled with the words "near" and "far" in Fig. 5.14(a)) at a location significantly out of focus relative to our light-field camera. Measuring the outputs of all angle sensitive pixels generates 32 different angle images (one from each complementary pair of angle sensitive pixel types in the tiled subunit) and a single intensity image. The angle images are shown in Fig. 5.15. Because the blocks are far from the camera's plane of focus, the recovered intensity image of Fig. 5.16(a) is badly blurred. Although each of the individual angle images are lower in resolution than the intensity image, they retain more detail of the blocks, illustrating how local incident angle measurement is important for recovering information from blurred images. Comparing the sub-frames of Fig. 5.15, we observe that angle-sensitive pixels with different angular gains, orientations, and phases result in distinct images. This diversity indicates that each of the various pixel types provides unique information about the blurred

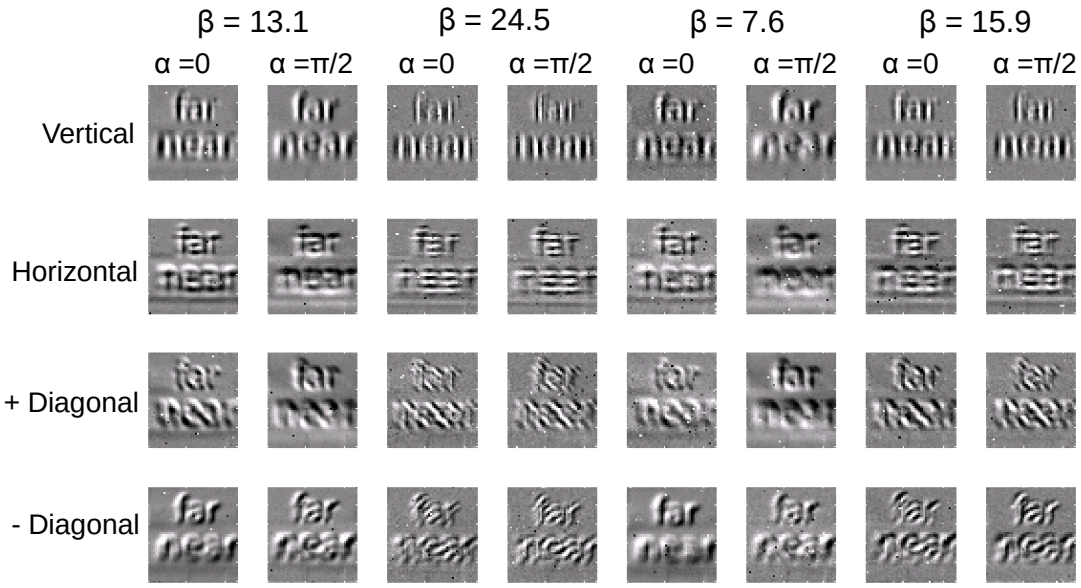

Figure 5.15: Angle images provided by the light-field camera. Each subimage corresponds to the difference in response for a pair of angle-sensitive pixels with distinct orientation, β, and α

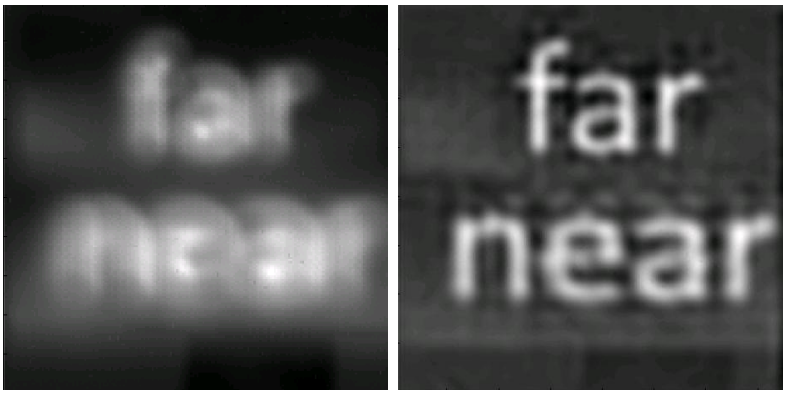

(a) (b)

Figure 5.16: (a) Intensity image from light field camera. (b) Synthetically refocused image based on angle information from Fig. 5.15, processed in the manner shown in Fig. 5.17, and intensity image in (a).

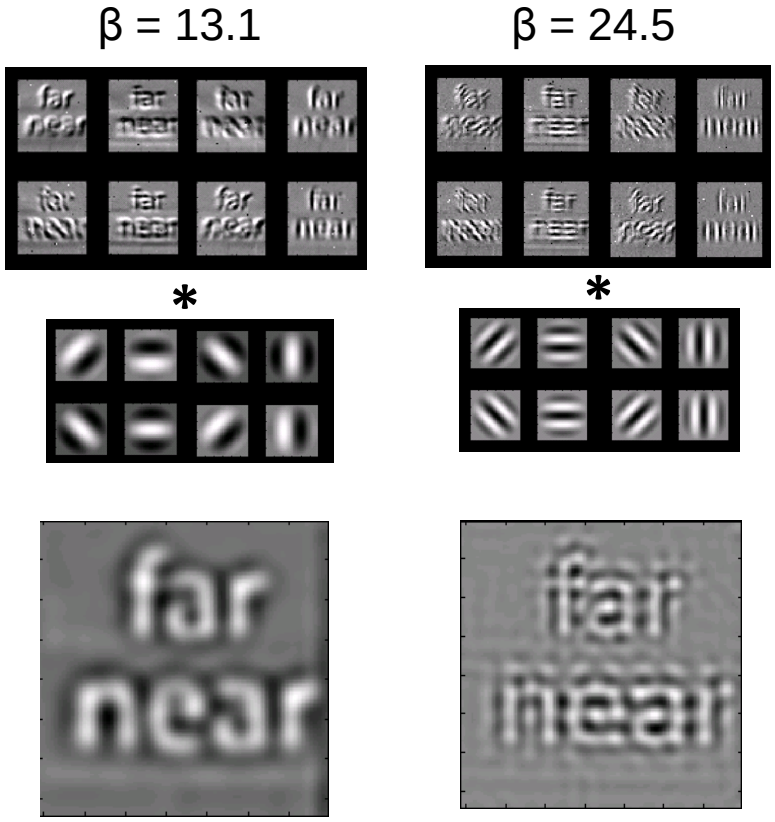

(a) (b)

Figure 5.17: Using angle images to perform refocus by convolving with scaled, oriented Gabor filters. (a) Summing together the convolution of 8 individual angle images with Gabor filters results in an intermediate image for $\beta = 13.1$. (b) Identical operation performed for angle images with $\beta = 24.5$.

image.

Previous work has shown that recording light field information enables computational refocus of captured images [34, 41]. We demonstrated this synthetic refocus by combining the intensity image with the 32 difference images. Each difference image was convolved with a Gabor filter [127, 128] whose orientation, spatial frequency and phase matched that of the relevant angle sensitive pixel. Adding the convolution products from identical frequency components together results in filtered images such as those in Fig. 5.17 for different spatial frequencies.

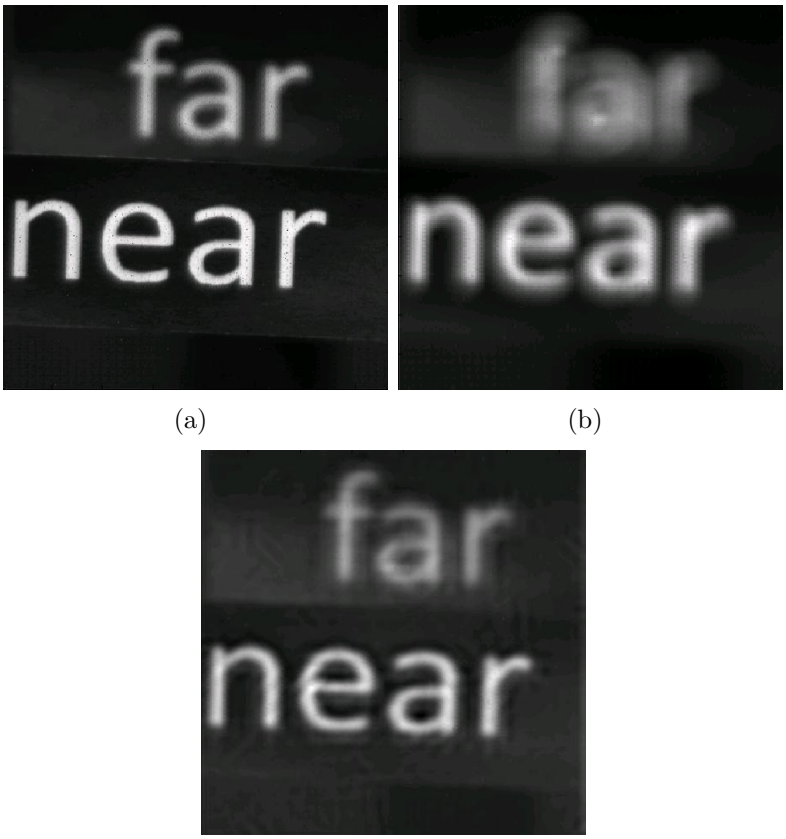

(a) (b)

(c)

Figure 5.18: (a) Raw pixel image from the image sensor when the word "near" is optically in focus. (b) Intensity image after small adjustment to optical focal plane. (c) Image in (b) after synthetic refocus.

Summing the resulting filtered images together with the intensity image generated the computationally refocused image shown in Fig. 5.16(b). The reconstructed image is much clearer than the original intensity image, and the labels are clearly legible.

Although a total of 64 angle-sensitive pixels are used to extract the complete angle information for computational refocus, the effective spatial resolution of an angle-sensitive pixel image sensor depends on the camera's plane of focus. For regions of a visual scene where the camera optics place an image in perfect focus, light arrives at each angle-sensitive pixel from many angles. As the light does not

Figure 5.19: Raw pixel image from the image sensor. As the front dice are in focus, the individual angle-sensitive pixels act as conventional intensity-sensitive pixels.

have a strong angular dependence, the periodic angle-sensitive component of the angle-sensitive pixel response (the cosine term of Eq. 5.1) averages to zero. Thus, each pixel functions as a conventional CMOS active pixel, albeit with some loss in sensitivity due to the gratings. This provides us with local intensity resolution at the actual pixel pitch, or 7.5μm (Fig. Fig. 5.18(a) and Fig. 5.19). In regions of the image that are out of focus, the angular sensitivity of each pixel responds to local incident angle gradients. Nevertheless, the sum of the responses generated by a single pair of complementary angle-sensitive pixels still provides local intensity information at an overall spatial resolution of 15μm.

In addition to sampling the local intensity at a 15 micron pitch, our angle-sensitive image sensor also acquires angle information that synthetic refocus can use to improve effective resolution. The spatial resolution for out-of-focus objects recoverable through refocus will depend on the degree of object blur. For the subsequent analysis, we assume that a visual scene generates an in-focus image at a distance ΔF relative to the surface of the imager, as shown in Fig. 5.20. For sufficiently large distances ΔF, a single pixel on the image sensor will receive light from objects at different spatial positions in the scene. However, the incident

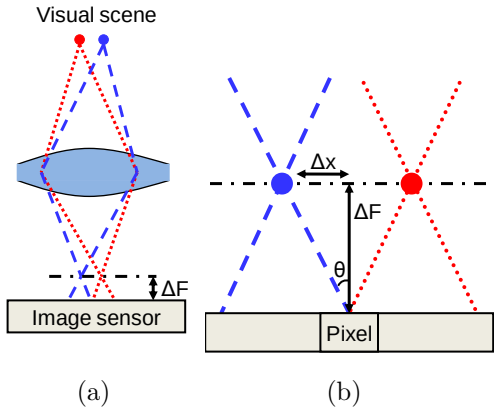

Figure 5.20: (a) Objects out of focus generate significant angular information. (b) Enlarged view of region directly above the image sensor illustrating critical dimensions.

light striking the pixel from these different objects arrives from distinct angles. In particular, an object's lateral displacement Δx corresponds to an angular displacement θ relative to normal by the relation $\Delta x = \Delta F \tan(\theta) \approx \theta \Delta F$. When placed behind a lens with aperture f/1.8 (numerical aperture of 0.28 in air), pixels of the image sensor receive light from a range of angles spanning +0.28 to -0.28 radians.

An angle-sensitive pixel convolves the angular distribution of the light it sees with its own characteristic angular response given by Eq. 5.1. Using an appropriate, diverse set of pixels, we obtain a complete description of this angular distribution up to the spatial frequency set by the angle-sensitive pixel with the highest angular sensitivity β in the set. From the Nyquist-Shannon sampling theorem, a signal with maximum spectral frequency Ω can be recovered with a sampling frequency of 2Ω. Consequently, a set of angle-sensitive pixels with highest angular sensitivity $\beta_{\max}$ can effectively sample an angular distribution at a resolution of $2\pi/2\beta_{\max}$ radians. This angular resolution translates to a spatial resolution sampling of $\pi\Delta F/\beta_{\max}$. As an example, the tiled subunit of 64 angle-sensitive pixels contains sufficient diversity to obtain a complete description of the local angular

distribution. We consider a point on an object whose focal plane is $\Delta F = 108\mu$m above the image sensor. With a f/1.8 aperture, the point generates a 60μm diameter blur. In our design, $\beta_{\max} = 24.5$ provides an angular resolution of 0.13 radians, or spatial resolution of 15μm. As the image blurs further with increasing ΔF, this resolution will degrade, but at a rate 1/4 that predicted by the lens aperture alone. Figure 5.18 demonstrates refocus for a significantly smaller ΔF as compared to the example shown in Fig. 5.16.

The aperture of the imaging lens affects refocus performance. In particular, the sampling limit is accurate only when pixel responses have at least one period over the numerical aperture of the photographic lens. This sets a minimum aperture size where angle-sensitive pixels will be able to function effectively. Like the spatial resolution achieved through refocus, this minimum aperture is set by the highest periodicity (highest β) angle-sensitive pixels. For the fabricated image sensor with highest angular resolution of 0.13 radians, the minimum photographic aperture is approximately f/4. At this aperture, the available range of angles is so narrow that only one quarter of the pixels (those with $\beta = \beta_{\max}$) recover information on local incident angle, limiting the quality of refocus. Choosing a smaller aperture than f/4 restricts the range of ray angles to the extent that angle sensitivity is lost across the sensor, and the angle-sensitive pixel array becomes a conventional, intensity-sensitive image sensor.

Small apertures are frequently used in photography to increase depth of field and reduce blurring in out of focus objects. Depth of field is approximately proportional to F-number [129], but larger F-number reduces the amount of light the lens passes. Because angle-sensitive pixels provide computationally enhanced depth of field, they provide a means to decouple this conventional tradeoff between lens aperture and depth of field. With an optical aperture of f/1.8, the fabricated

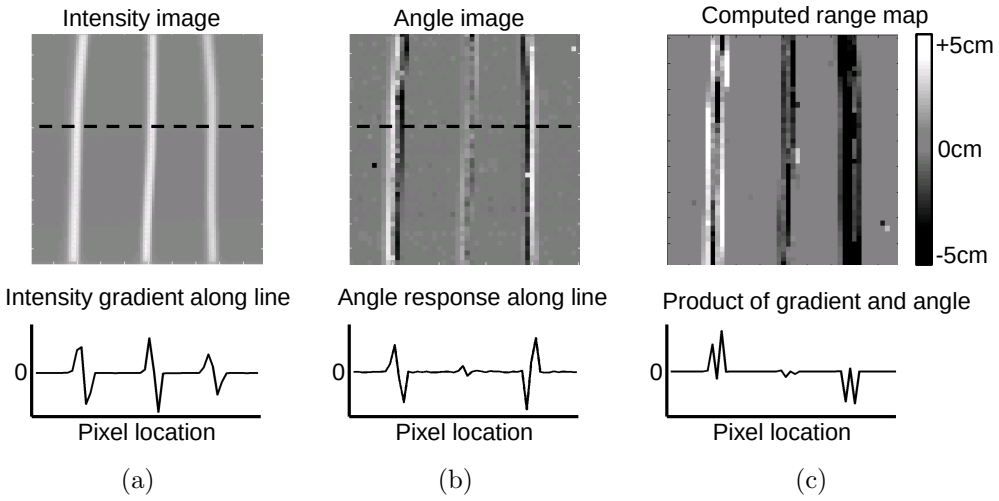

Figure 5.21: 3D depth extraction using angle information. (a) Intensity image of three white bars at different depths, computed gradient of intensity along the dashed line. (b) Angle image produced by one pair of angle-sensitive pixels with $\beta = 13.1$. (c) Range map based on intensity gradient and angle images.

image sensor with $\beta_{\max} = 24.5$ achieves an improvement in spatial resolution by a linear factor of 4 for out-of-focus objects. This blur reduction results in a computational depth of field equivalent to an aperture of approximately f/8.

The Gabor filters we use for computational refocus on captured images (Fig. 5.17) must be adjusted in scale and phase to account for the distance of in-focus images relative to the position of the image sensor ΔF. This distance determines the translation between angular and spatial resolution and therefore is necessary for effective synthetic focus. Furthermore, given prior knowledge of the optical system, measuring this distance lets us recover depth estimates of objects in a visual scene, relative to the focal plane of the lens optics. We investigated using angle-sensitive pixel outputs to compute a range map which provides the necessary range information from a single image. As shown in Fig. 5.21, objects at different depths (in this case, the 3 white bars of Fig. 5.14(b)) generated similar intensity images, but very different angular images. The bar on the left, whose image lies in

front of the image sensor produced an angular response with the same polarity as the gradient in intensity. In contrast, the bar on the right, whose image lies behind the image sensor, produced and angular response with the opposite polarity. The center bar generated little angular response as it is close to being in focus and therefore creates a homogenous distribution of angle.

To utilize this information for object rangefinding, we have developed a simple algorithm based the properties of blurred edges in a scene. An out-of-focus edge generates a local gradient in intensity whose magnitude is proportional to the contrast of the edge and inversely proportional to the degree of defocus. In other words, increasing distance between the location of the in-focus edge and the location of the image sensor leads to more blurring and a weaker intensity gradient across the captured image. The sign of this gradient is insensitive to the degree of defocus and to distance ΔF. In contrast, the direction of the angular distribution created by the out-of-focus edge depends on the sign of ΔF, that is, whether the location of the in-focus edge is in front of or behind the image sensor (Fig. 5.1(b)). A pair of differential angle-sensitive pixels with an odd symmetry (those with phase offsets α of $\pi/2$ and $3\pi/2$ in Eq. 5.1) and one full period in response over the range of angles admitted by the lens aperture ($\beta = 13.1$ for our lens with F#=1.8) will provide a response which inverts in sign based on the location of the edge relative to the focal plane of the lens. Furthermore, these angle-sensitive pixels have a response that is proportional to the contrast of the edge but only weakly affected by the degree of defocus. The ratio of the local ASP response to the local intensity gradient therefore provides a useful estimate of degree and direction of defocus, and accordingly of range to objects in a visual scene.

Each tiled subunit of 64 angle-sensitive pixels provides 4 estimates of range from the distinct orientations, each with an error inversely proportional to the lo-

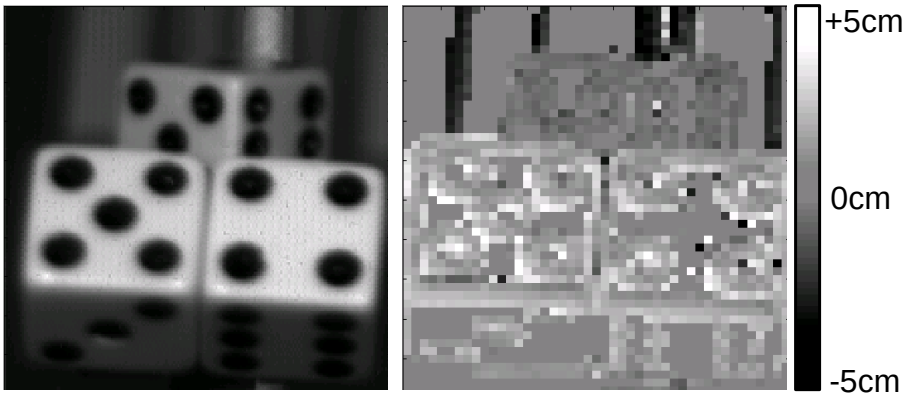

(a)

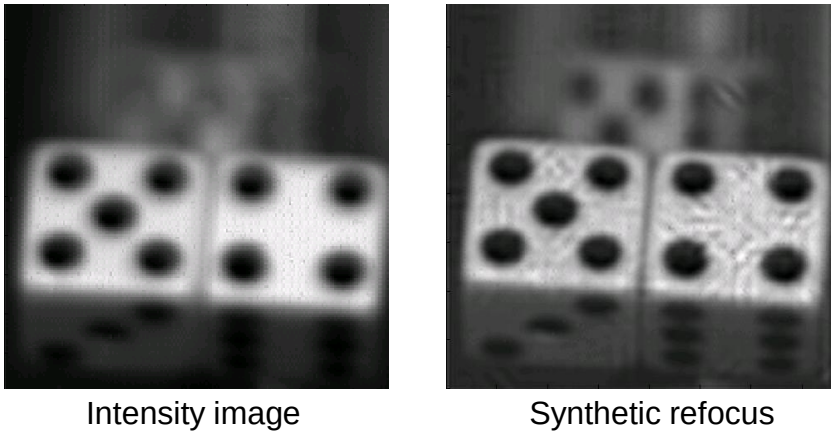

(b)

Figure 5.22: Computational refocus and rangefinding using light-field information from a complex scene. (a) Calculation of depth in a scene containing three dice at different depths. (b) Post-capture refocus performed on same scene after moving camera focus.

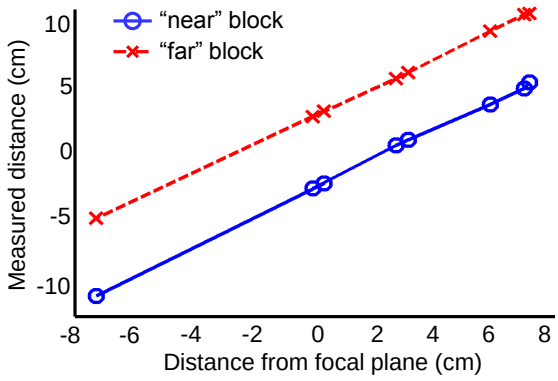

Figure 5.23: Plot of measured range to a pair of labeled blocks. The two blocks are separated by a fixed distance and moved together to various positions relative to the lens focal plane.

cal intensity gradient in that orientation. To obtain a final range estimate, we employ a simple version of Bayesian estimation by adding together the product of each differential angle-sensitive pixel output with its associated intensity gradient and normalizing this sum-of-products by the sum of squared gradients. This estimation approach easily extends from rangefinding on simple edges to distance measurement for larger objects and areas of a visual scene. We applied this rangefinding algorithm both to simple scenes (Fig. 5.21) and more complex scenes (Fig. 5.22(a)). Once calibrated for lens optics, we computed the precision of our algorithm by placing the pair of labeled blocks used for refocus performance at various positions relative to the focal plane and measuring their locations. Calculated range information at these positions is plotted in Fig. 5.23. By comparing the estimated distances with the known separation between the two blocks, we obtained a mean-square error of $\pm$2.5mm at a focal distance of 1m.

Rangefinding performance with our light-field image sensor is comparable to the other methods shown in Table 5.2. One important limitation of our edge-based rangefinding is that it provides no meaningful estimates of range for regions of a

Table 5.2: Comparison of rangefinding performance with previous work

Ref.	[112]	[114]	[115]	[116]	[118]	This work
Method	Active ToF	Active ToF	Active ToF	Light-section	Stereo	Light-field
Pixels	128×128	80×60	128×96	256×256	$2 \times 128 \times 128$	400×384
Light source	Pulse laser	850nm LED	850nm LED	Sheet laser	Ambient	Ambient
Range	20-375cm	20-600cm	40-240cm	40cm	80cm	1m
Precision	5mm	2cm	16cm	0.26mm	1.67cm	2.5mm
Power	180mW	18mW	40mW	NA	30mW	140mW

visual scene with little or no contrast. Such areas can be identified by their lack of strong intensity gradient, and hence can be eliminated from range estimates (grey areas in Fig. 5.21 and Fig. 5.22(a)). This approach also fails when image defocus becomes sufficiently severe that edges begin to blur into one another. More sophisticated algorithms can likely overcome this limitation, but are beyond the scope of the work published here.

To demonstrate synthetic refocus and rangefinding with complex scenes, we used our camera to photograph several dice at different depths. We used the processing methods described above to perform range mapping and computational refocus with the light-field information recovered in a single image. As can be seen in Fig. 5.22(a), when we place the focal plane of the camera between the dice, the forward pair of dice are identified as being 3cm in front of the focal plane in the captured image, while the rear die is identified as falling behind the focal plane by 2cm. Background structures (vertical bars) are identified as lying behind the rear die. Moving the focal plane in front of all the dice blurs the intensity image (Fig. 5.22(b)), but the angular information captured by the angle-sensitive pixel array is sufficient to computationally bring the dice back into focus.

Table 5.3: Summary of sensor performance

Parameter	Value
Process node	TSMC 0.18μm 1P6M Analog/RF CMOS
Chip area	4×5mm
Array size	400×384 pixels
Pixel size	7.5μm×7.5μm
Fill factor	58%
Conversion gain	8μV/e$^-$
Supply voltage	1.8V
Frame rate	200 frame/s
Objective lens	Nikkor 50mm, F# = 1.8
Refocus resolution	15μm×15μm at 60μm spot size
Rangefinding error	±2.5mm at 1m range
Power consumption	140mW at 200frame/s

Table 5.3 summarizes the performance parameters of the demonstrated image sensor as well as important measurement results.

5.6 Conclusions

We anticipate several avenues for further development in our demonstrated light-field image sensor. In particular, the reduction in quantum efficiency from the gratings must be addressed with alternative angle-sensitive pixel structures. Significant in-focus resolution enhancement can be achieved by decreasing in pixel pitch from the current 7.5μm. Although grating pitch is limited by design considerations, using fewer periods of grating is a direct approach to reducing angle-sensitive pixel size. However, at least three grating periods are necessary to avoid strong edge effects from finite gratings. To improve the spatial resolution achievable with computational refocus, angle-sensitive pixels with higher angular sensitivity β will be necessary. While the more tightly controlled back-end available in recent CMOS manufacturing processes below 180nm could be used to generate these pixels, ion migration barriers necessary for damascene copper interconnect and specialized

low-k dielectric require more accurate optical simulations than our current model. Finally, the algorithms for computational refocus and rangefinding based on angle-sensitive pixel outputs have significant room for improvement.

We have demonstrated a CMOS image sensor appropriate for light-field imaging. The imager incorporates a diverse array of angle sensitive pixels, each of which employs a pair of metal diffraction gratings to filter for light from specific incident angles. The pixel-scale gratings were implemented using the interconnect layers inherent to the standard 180nm CMOS manufacturing process used, and no additional off-chip optics or postprocessing was necessary. Compared to a traditional intensity-sensitive imager, our chip captures a much richer description of the light striking it. The additional information permits post-capture range finding of objects in a scene and permits computational refocus of out-of-focus parts of the scene. Angle-sensitive pixel arrays therefore provide a very low cost and complexity approach to building image sensors for light-field capture under ambient illumination.

Chapter 6
Image processing implications

6.1 Introduction

Image capture and image processing are frequently treated as distinct processes. The capture device is responsible for acquiring and digitizing a bitmap image containing an array representing local light intensities. Processing works directly in the digital domain, taking the captured image as input. However, image capture is fundamentally a form of image processing which takes a visual scene as input and converts light reflected from the scene to a chemical (film) or electrical (digital sensor) signal to generate an output.

In many circumstances, the processing intrinsic to image capture is detrimental to the performance of the subsequent image processing tasks. For example, an object placed in focus for a conventional imaging system generates a sharp, high quality image. Changing the object depth blurs the captured image and can be described as a spatial low-pass filter resulting in loss of information. Current research has demonstrated image capture systems engineered to perform helpful, as opposed to harmful, image processing. These new systems modify a conventional camera by changing the optical path [41, 119, 120] or by altering the optical properties of the sensor pixels making up a digital image sensor.

We have recently presented a diffractive CMOS imager pixel [28], which filters incoming light according to the local distribution of light across incident angle. Compared to an imager pixel which measures local light intensity, these "angle-sensitive" pixels capture extra information about out-of-focus parts of a scene. The pixel-level signals encode out-of-focus scene features in a bandpass, rather than lowpass, format. In this paper, we develop a mathematical framework for

describing the optical image processing performed by such angle sensitive pixels, and show how the additional information captured enables computational refocus and depth estimation with simple computations.

The text is organized as follows: we first introduce the concept of an angular transfer function and develop a general mapping of a pixel's angular transfer function into a spatial transfer function as a function of the lens system used. We then review the physical structure and resulting angular transfer function of previously demonstrated angle-sensitive pixels. Based on this transfer function, we derive the spatial band-pass properties of such pixels, and the sampling behavior of angle-sensitive pixel arrays. We then discuss the implications and applications of such arrays, particularly in the context of 3D imaging, and finally show experimental results from one such array.

6.2 The angular transfer function

The pixels comprising a typical CMOS or CCD digital image sensor are physical devices which transduce the properties of the light they see into electrical signals. To analyze the image acquisition capability of a particular pixel device, we construct a model which describes its sensitivity to the specific property of interest. For example, the RGB pixels employed in color image sensors each have a distinct wavelength response profile. By measuring this wavelength dependent sensitivity, we obtain a wavelength transfer function $h(\lambda)$ which models how the pixel responds to light of different monochromatic wavelengths.

Wavelength is just one of the possible properties of light that the pixels of an image sensor might measure. Recent work in our lab has demonstrated image sensors composed of pixels which are sensitive to the incident angle of light striking them [110]. In a similar manner to wavelength and color pixels, these angle-

sensitive pixels have a characteristic angular sensitivity. By measuring their angle-dependent response to light, we obtain the angular transfer function $h(\theta, \phi)$. This function describes the detector response to plane wave incident light arriving from different incident angles.

We begin our discussion with the general implications of incident angle imaging. Before exploring this idea, we first introduce some notation which will be used throughout the remainder of the text. Let $S(x, y, z)$ represent an arbitrary three-dimensional visual scene of interest, with (x, y, z) coordinates denoting spatial position. We assume Lambertian reflectance for the scene, such that illuminating light is reflected in an isotropic manner. We simplify the image-forming optical system to a single thin lens with focal length F and aperture D satisfying the paraxial small-angle approximation. For image capture, we assume that the image sensor is composed of a 2D array of pixels arranged in a regular grid and that its size is much smaller than D. The recorded image is finally represented by an array of voltages $V(i, j)$, with (i, j) coordinates denoting pixel position and voltage V proportional to incident photon flux.

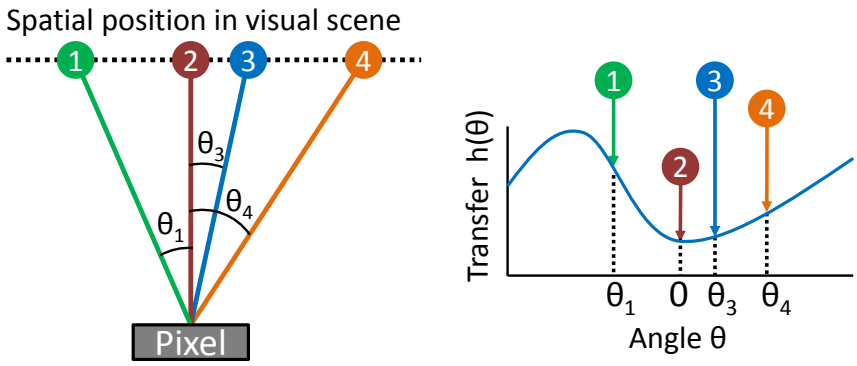

Figure 6.1: The response of a pixel to a visual scene is the sum of the intensity of light arriving from different points, weighted by the angular transfer function $h(\theta, \phi)$

To start, we consider the simple imaging arrangement of Figure 6.1, with a 2D image $S(x, y)$ placed a distance Z directly in front of a single pixel with angular transfer function $h(\theta, \phi)$. We assume that the size of the pixel is small relative to the scene $S(x, y)$ and therefore approximate it as a point at location (i, j). Light emanating from the scene at location (x_k, y_k) arrives at the pixel as a plane wave with a characteristic solid angle of incidence (θ_k, ϕ_k), such that $x_k = Z \tan \theta_k$ and $y_k = Z \tan \phi_k$. Therefore, the contribution to the overall photon flux observed by the pixel from this kth location in the visual scene is $v_k = S(x_k, y_k)h(\theta_k, \phi_k)$. As this imaging arrangement uses no lens, all points of the scene are visible to the pixel. The pixel output will integrate the contributions from the entire visual scene, such that total pixel response V is given by the integral inner product

$$V = \int_{-\pi/2}^{\pi/2} \int_{-\pi/2}^{\pi/2} h(\theta, \phi) S \left(Z \tan \theta Z \tan \phi \right) \, \mathrm{d}\theta \, \mathrm{d}\phi \tag{6.1}$$

In effect, the angular transfer function $h(\theta, \phi)$ selectively strengthens or weakens the contribution of different scene locations to photon flux and therefore to the pixel response.

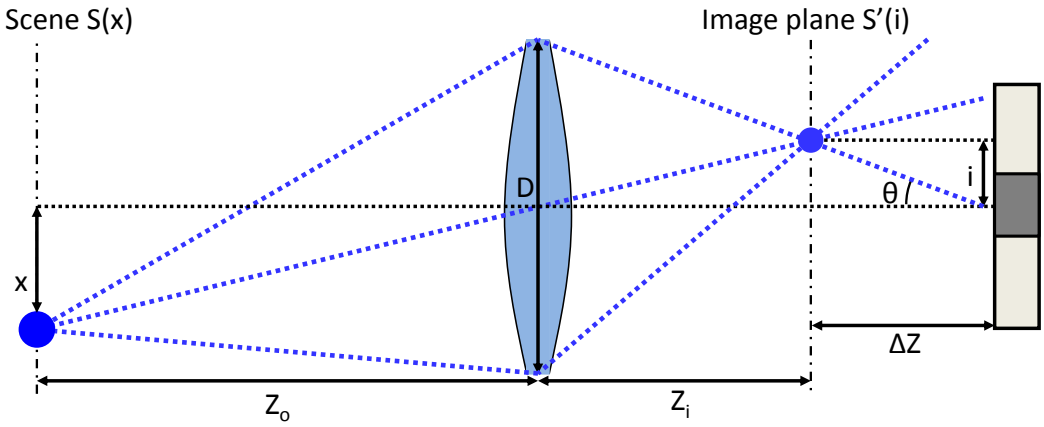

Figure 6.2: Light arriving at a pixel placed behind a lens can be expressed in terms of the light reflected by different points in the visual scene.

The angular transfer function acts as a spatial weighting function whose spatial scale is determined by the distance Z from pixel to scene. Introducing a thin lens to the scene-pixel system does not fundamentally alter this behavior. A visual scene $S(x, y)$ a distance Z_o in front of a thin lens projects a real image at a distance Z_i behind the lens. The relationship between these two distances is given by the thin lens equation $\frac{1}{Z_o} + \frac{1}{Z_i} = \frac{1}{F}$, where F is the lens focal length. The projected image is a scaled version of the original scene, scaled by the ratio $M = Z_o/Z_i$. We place a single pixel a distance Z behind the lens, approximated as a point at position (i, j). The geometry of the ray optics, illustrated in Fig. 6.1, imply that light at position (i, j) arriving from the scene $S(x, y)$ is given as a function of location and incident angle by the expression

$$\begin{aligned} I(i, j, \theta, \phi) &= S\left(\frac{Z_o}{Z_i} i + \frac{Z_o}{Z_i}\Delta Z \tan\theta, \frac{Z_o}{Z_i} j + \frac{Z_o}{Z_i}\Delta Z \tan\phi\right) \\ &\approx S\left(Mi + M\Delta Z \cdot \theta, Mj + M\Delta Z \cdot \theta\right) \end{aligned} \tag{6.2}$$

We have made a small angle approximation for the tangent function, and defined ΔZ as the distance between the image plane and the pixel: $\Delta Z = Z - Z_i$. The ratio $M = Z_o/Z_i$ sets the magnification of the system, and the distance ΔZ sets the mapping between spatial and angular coordinates. Since the image may form either in front of or behind the pixel, the sign of ΔZ can be positive or negative.

The projected image does not have the isotropic emission properties of the original scene, as the finite aperture of the lens restricts the maximum observable incident angles $\theta_{\max}$ and $\phi_{\max}$ to $\pm\arctan(D/2Z)$. Nevertheless, over the range of incident angles passed by the lens, the pixel weights locations by its angular transfer function when it integrates light over the portion of the visual scene it sees. Assuming that the lens aperture transmittance is a 2D box function of

incident angle and that Z is large relative to lens aperture, the pixel output is therefore

$$V = \int_{-D/2Z}^{D/2Z} \int_{-D/2Z}^{D/2Z} h(\theta, \phi) I(i, j, \theta, \phi) \, \mathrm{d}\theta \, \mathrm{d}\phi \tag{6.3}$$

Conventional image sensor pixels attempt to achieve an isotropic response to incident light and have angular transfer functions $h(\theta, \phi)$ which are well approximated by simple symmetric concave functions. In contrast, recently developed angle-sensitive pixels have angular transfer functions which are windowed sinusoids [28]. These pixels use micro-scale diffraction effects to achieve their periodic angular response. The principles of their operation are described in the next section.

6.3 Angle-sensitive pixels

Angle sensitive pixels have been implemented as shown in Fig. 6.3. We overlay a photodiode with a pair of stacked metal diffraction gratings. Light incident upon the upper grating generates periodic diffraction patterns ("self-images") at specific depths beneath the grating, an phenomenon known as the Talbot effect [35]. Self-images are strongest at half-integer multiples of the Talbot distance z_T [44], defined as twice the square of the grating pitch (d), divided by the wavelength of the light (λ): $z_T = {}^{2d^2}/_{\lambda}$

In an angle sensitive pixel, the diffracted light passing through the upper grating strikes a second "analyzer grating" of equal pitch, placed at a depth where strong periodic diffraction patterns form, $h = \frac{1}{2} n z_T$ where n is an integer. The self-images shift laterally in response to shifts in the incident angle [56], and the analyzer grating blocks or passes light depending upon the position of the self-image intensity peaks relative to the analyzer grating. When the peaks align with

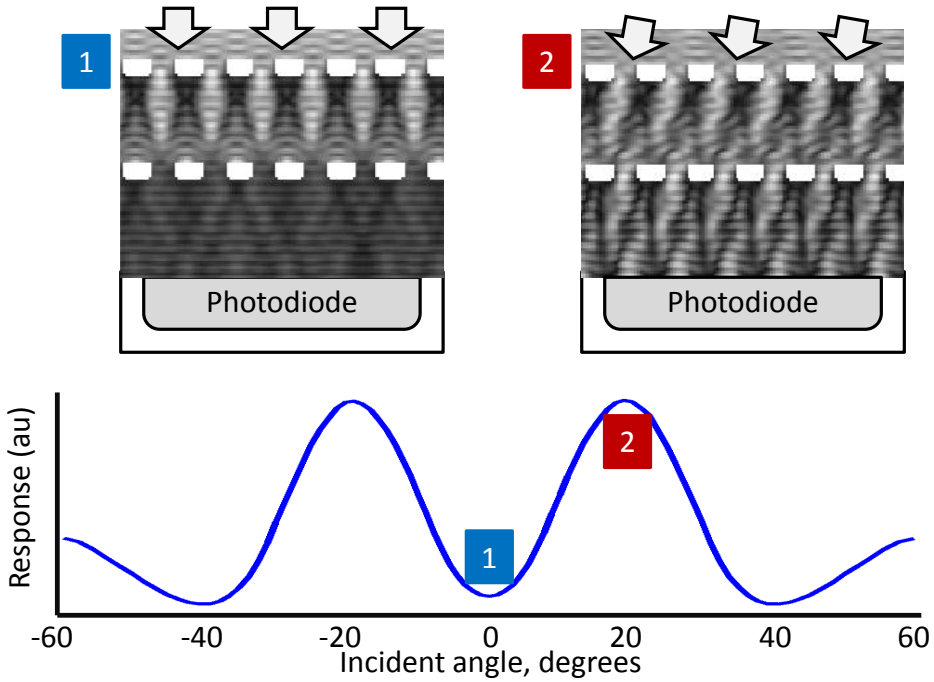

Figure 6.3: An angle-sensitive pixel relies on diffractive optics to achieve a periodic response to incident angle.

gaps in the grating, light passes through; when they align with the bars, light is blocked. The photodiode below measures the light flux passed by the analyzer grating. Because both the self-image of diffracted light and analyzer grating are periodic, the amount of light passed also varies periodically with incident angle θ according to the equation:

$$h(\theta) = I_o A(\theta)(1 - m\cos(\beta\theta + \alpha)) \tag{6.4}$$

The parameter $\beta = 2\pi h/d$ defines the frequency of the periodic response. I_o is the incident light intensity, modulation depth $m(0 < m < 1)$ is set by the quality of the self-image and phase offset α is set by the lateral offset between the gratings. Finally, the aperture function $A(\theta)$ is a symmetric windowing function which accounts for metal sidewalls and reflections at the chip's surface. This

periodic response to angle contrasts with that of traditional image sensor pixels, which essentially average light from all angles with equal weight.

Angle sensitive pixels have been manufactured entirely in a standard commodity semiconductor manufacturing process [110], using doped silicon junctions as photodiodes and metal interconnect layers for local diffraction gratings. Because the gratings are of a fine pitch ($d < 1\mu$m), these pixels can be built on the scale of a conventional digital image sensor pixel. Figure 3 shows the simulated response of a single angle-sensitive pixel to light of varying incident angle but uniform intensity, illustrating the periodic angle-dependent response predicted by eq. 6.4.

The angular transfer function of eq. 6.4 only applies for θ measured perpendicular to the orientation of the grating wires, and only for a single light source. In general, the pixel gratings can take any orientation angle ψ, and the light rays striking the pixel $I(\theta, \phi)$ are distributed in two angular dimensions. We can then write the overall pixel output as the superposition of the pixel's response to incident light from each direction:

$$V = \int_{-\pi/2}^{\pi/2} \int_{-\pi/2}^{\pi/2} I(\theta, \phi) A(\theta, \phi) \left[1 - m \cos\left(\phi \cdot \beta \sin\psi + \theta \cdot \beta \cos\psi + \alpha\right)\right] \, \mathrm{d}\theta \, \mathrm{d}\phi \quad (6.5)$$

6.4 Bandpass properties of angle-sensitive pixels

The angle-sensitive pixels exhibit their sinusoidal response along the axis perpendicular to the gratings. In the axis parallel to the gratings, the aperture function dominates the angular sensitivity, resulting in a simple, symmetric concave sensitivity profile similar to those of conventional image sensor pixels. To simplify analysis of our incident angle imaging sensor, we project the 2D optics and imaging system into a single dimension perpendicular to the gratings. Furthermore, we treat the angular transfer function of pixels as a product-separable function, and

therefore consider only the dimension corresponding to the axis with the sinusoidal response.

As previously done in section 6.2, we consider an optical system with a single thin lens, and a 1D image $S(x)$ placed a distance Z_o away. The lens projects an image a distance Z_i away, and we place a single angle-sensitive pixel a distance Z away from the lens, approximated as a point at position i. Light at position i arriving from the scene $S(x)$ is given as a function of incident angle by the expression

$$\begin{aligned} I\left(i,\theta\right) &= S\left(\frac{Z_o}{Z_i}i + \frac{Z_o}{Z_i}\Delta Z\tan\theta\right) \\ &\approx S\left(Mi + M\Delta Z\cdot\theta\right) \end{aligned} \tag{6.6}$$

The angle-sensitive pixel weights this incident light distribution with its characteristic angular transfer function and integrates the total flux to generate a response V(i) given by

$$\begin{aligned} V\left(i\right) &= \int I\left(i,\theta\right)\cdot h\left(\theta\right)\,\mathrm{d}\theta \\ &= \int_{\theta_1}^{\theta_2} S\left(Mi + M\Delta Z\cdot\theta\right) A(\theta)(1 - m\cos(\beta\theta + \alpha))\,\mathrm{d}\theta \end{aligned} \tag{6.7}$$

The limits of integration θ_1 and θ_2 are determined by the position of the pixel in the optical system, finite lens aperture and distance between lens and pixel. For a pixel placed on the optical axis, such that i equals zero, then the limits θ_1 and θ_2 are $\pm\arctan\left(D/2Z\right)$.

For a more intuitive understanding of the pixel response, we observe that incident angle θ at the pixel maps directly to position in the scene coordinates x, where $x = Mi + \Delta x$ and $\Delta x = M\Delta Z\cdot\theta = k\theta$. Substituting these relationships into the previous integral expression for $V(i)$, we have

$$V(i) = \frac{1}{k}\int_{\Delta x_1}^{\Delta x_2} A\left(\frac{\Delta x}{k}\right)\left[1 - m\cos\left(\frac{\beta}{k}\Delta x + \alpha\right)\right] S(Mi + \Delta x)\, \mathrm{d}\Delta x \tag{6.8}$$

If the distance to the image sensor Z is large relative to the lens aperture D, then the spatial limits Δx_1 and Δx_2 are given by $\pm k\,(D/2Z)$ for i equal to zero. We observe that the response $V(i)$ is the sum of two distinct components. The first contribution to the response arises purely from the aperture function $A\,(\Delta x/k)$ and is similar to that observed by a conventional image sensor pixel. The second contribution to the response results from the action of the diffraction gratings on light of different incident angles, generating the $m\cos\left(\beta/k\Delta x + \alpha\right)$ in the integrand. To extract this sinusoidal component of the response, we introduce a second, complementary angle-sensitive pixel with frequency of response β identical to the first, but phase offset α_2 distinct by an additional offset of π, such that $\alpha_2 = \alpha + \pi$. We assume that the devices are small such that the lateral offset in position Δi is negligible, and therefore they occupy approximately the same position i. By trigonometric identities, the sum of the two pixel responses $\Sigma V(i)$ has the form

$$\Sigma V(i) = \int_{\Delta x_1}^{\Delta x_2} A\left(\frac{\Delta x}{k}\right) S(Mi + \Delta x)\, \mathrm{d}\Delta x \tag{6.9}$$

This response convolves the image $S(x)$ with the symmetric aperture function $A(\theta)$ and therefore acts as a low-pass filter on the scene. If we approximate A as Gaussian, the response corresponds to a simple 1D Gaussian blur whose scale is set by the parameter k. When the pair of pixels is placed at the image plane such that ΔZ is zero, then the scaling factor k is zero as well. Under this condition, the aperture function A becomes a Dirac delta function. By the sifting property of delta functions, this summed response simply corresponds to a single point in the image $S(Mi)$, indicating a one-to-one correspondence between image coordinates and pixel coordinates and accordingly an in-focus image. As the image plane moves

away from the image sensor position, ΔZ and hence k increase in magnitude and create the blur across pixels characteristic of an out-of-focus image.

In contrast, the difference in the two complementary pixel responses $\Delta V(i)$ extracts the response component resulting from the periodic nature of the pixel's angular transfer function:

$$V\left(i\right) = \frac{1}{k}\int_{\Delta x_1}^{\Delta x_2} A\left(\frac{\Delta x}{k}\right)\cos\left(\frac{\beta}{k}\Delta x + \alpha\right) S\left(Mi + \Delta x\right)\,\mathrm{d}\Delta x \tag{6.10}$$

We observe that a pair of angle-sensitive pixels convolves the visible scene it sees with a windowed sinusoid. The period of the sinusoid is set by the response frequency β of the pixel and therefore controlled by the geometry of the diffraction gratings, while the window of the sinusoid is set by the aperture function A. This response acts as a 1D spatial bandpass filter on the image $S(x)$, computed in the optical domain.

To extend the previous analysis to two dimensions, we recall the response of an angle-sensitive pixel to a set of 2D incident light rays, given in Eq. 6.5. By relating incident angle θ and ϕ at the pixel to position coordinates in the image $S(x, y)$, we find that the difference in angle-sensitive pixel responses is given by

$$\begin{aligned} V\left(i,j\right) = \int_{\Delta x_1}^{\Delta x_2}\int_{\Delta y_1}^{\Delta y_2} A\left(\frac{\Delta x}{k}, \frac{\Delta y}{k}\right)\cos\Bigg(\frac{\beta\sin\psi}{k}\Delta y \\ + \frac{\beta\cos\psi}{k}\Delta x + \alpha\Bigg) S\left(Mi + \Delta x\right)\,\mathrm{d}\Delta y\,\mathrm{d}\Delta x \end{aligned} \tag{6.11}$$

The scaling parameter k is defined as before: $k = M\Delta Z$. We conclude that two angle-sensitive pixels together function as a 2D spatial bandpass filter on visual scenes $S(x, y)$ with a defined center frequency set by frequency β and rotation set by grating orientation ψ.

6.5 Bandpass sampling

The relevant properties of the angle-sensitive pixel based bandpass filter are its center frequency and bandwidth. The center frequency of the filter $\Omega_c = \beta/k$ is set by both the characteristic response of the angle-sensitive pixel itself (periodicity β) and the geometry of the imaging system (scaling factor $k = M\Delta Z$), particularly the position of the image sensor relative to the focal plane of the lens optics. The bandwidth is controlled by the physical lens aperture D and the windowing function $A(\theta, \phi)$. The uncertainty principle between spatial extent and spectral bandwidth implies that $(\Delta x_2 - \Delta x_1)\,\Delta\Omega \geq 1$ for Δx_1 and Δx_2 introduced in Eq. 6.8 and establishes a lower bound $\Delta\Omega \geq Z/(D \cdot k)$ for the filter bandwidth. Figure 6.4 shows the spectral response the lowpass filter formed by the sum of a pair of angle-sensitive pixels and the bandpass filters formed by the difference of angle-sensitive pixels.

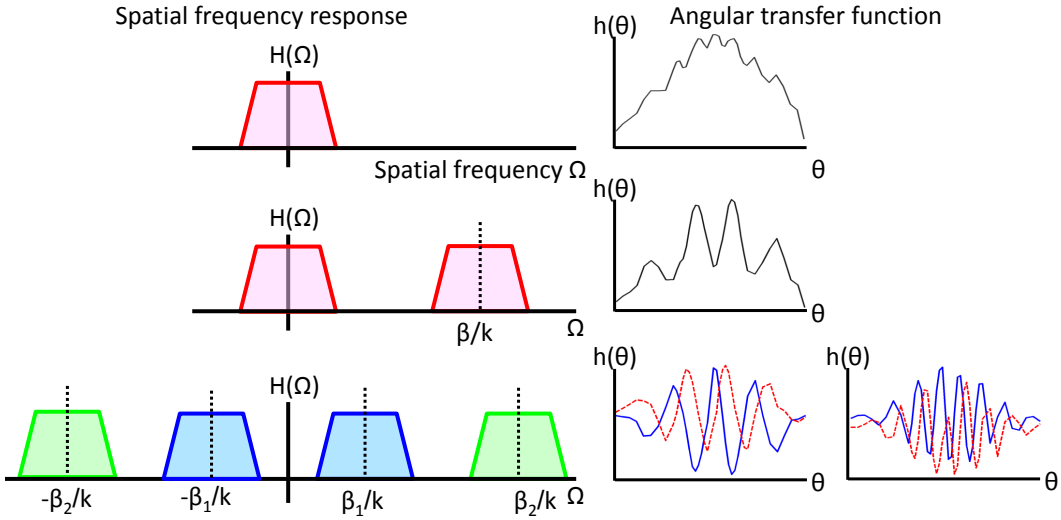

Figure 6.4: A conventional image sensor pixel acts as a low-pass spatial filter, while an angle-sensitive pixel has both a low-pass and bandpass component. Subtracting responses of complementary angle sensitive pixels eliminates the low pass component. Selecting different response frequencies β and phase offsets α generates bandpass filters with distinct center frequencies.

To examine the implications of these angle-sensitive pixel based optical band-pass filters, we consider a band-limited white image $S(x)$ with maximum spatial frequency $\Omega_{\max}$. To recover this image with a conventional image sensor, we place an array of pixels with pitch T such that the spatial sampling frequency achieves the required Nyquist frequency $2\Omega_{\max}$. However, this sampling scheme is only successful with an in-focus image. Approximating the angular transfer function of conventional pixels with a Gaussian function, each pixel acts as a low-pass filter with bandwidth $Z/(D \cdot k)$. When the image is in focus, such that the scaling factor k approaches zero, these pixels act as impulse functions and the properties of the Fourier transform of a periodic impulse train guarantee that $S(x)$ is recoverable with the sampled pixel responses. As the image goes out of focus such that $Z/(D \cdot k) \leq 2\Omega_{\max}$, the image is oversampled and information is lost relative to the in-focus case.

One complementary pair of angle-sensitive pixels cannot capture sufficient information to guarantee accurate reconstruction. Hence, we arrange an array of pixel pairs with pitch T as before. However, we employ N distinct angle-sensitive pixel types with uniformly spaced angular sensitivities $\beta_1 \cdots \beta_N$ such that the pitch of pixel pairs with sensitivity β_m is NT. For an in-focus image, the sum of outputs from each pair of angle-sensitive pixels generates a response identical to that of a conventional image sensor pixel, and $S(x)$ is recoverable as before. The difference in responses for each pair is approximately zero, owing to the large cosine argument in the integral for $\Delta V(i, j)$ of Eq. 6.10, and does not contribute any meaningful information.

As an image moves out of focus, the scaling factor k increases in magnitude. This increase results in Gaussian blur seen by the sum of responses from individual pixel pairs (Eq. 6.9) and a reduction in recovered spectral bandwidth in a manner

identical to defocus on a conventional image sensor. The response differences from individual pixel pairs (Eq. 6.10) act as bandpass filters and have center frequency and bandwidth inversely proportional to k. For mild defocus and small k, the N bandpass filters span beyond the spatial sampling frequency and aliasing occurs in the highest frequency filters. Nevertheless, the image $S(x)$ remains recoverable as no spectral content is missing. At some ideal degree of defocus, corresponding to scaling factor k_{ideal} the N bandpass filters exactly cover the full range of spatial frequency $(-\Omega_{\max}, \Omega_{\max})$ and no aliasing occurs. This point corresponds to the maximum amount of defocus allowed while maintaining a complete image recovery. Further blur beyond this point results in irreversible information loss. These three conditions are diagrammed in Fig. 5.

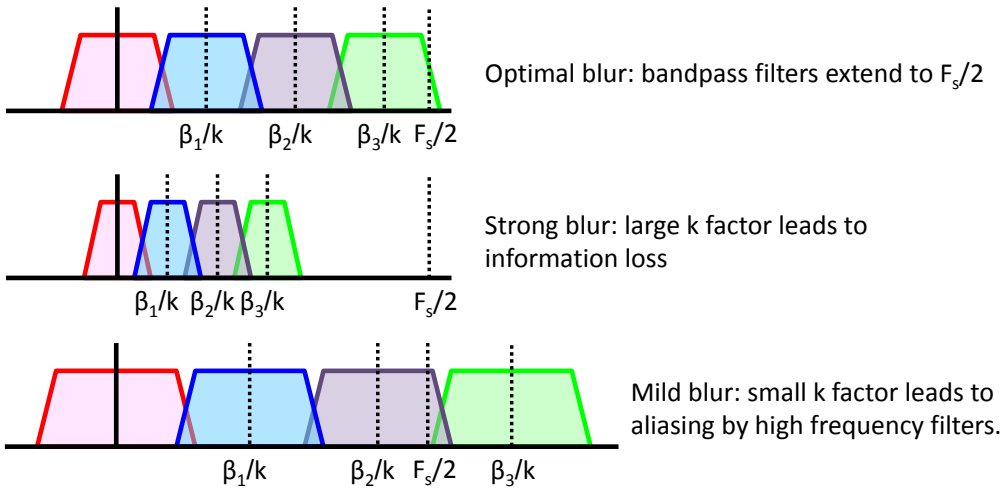

Figure 6.5: Degree of lens defocus sets scaling parameter k and therefore both bandwidth and center spatial frequency of the angle-sensitive pixel filters.

The ideal degree of defocus is proportional to N, the number of bandpass filters chosen. In general, the filter count represents a continuum, with increasing N providing increased tolerance for image defocus. Conventional image sensors having one "bandpass" filter with a zero center frequency, can be thought to be the trivial case with N = 1 and occupy one extreme. On the other extreme, recently

published Fourier-domain cameras use a very large set of bandpass filters and have sufficient defocus tolerance to perform imaging with no lens [130].

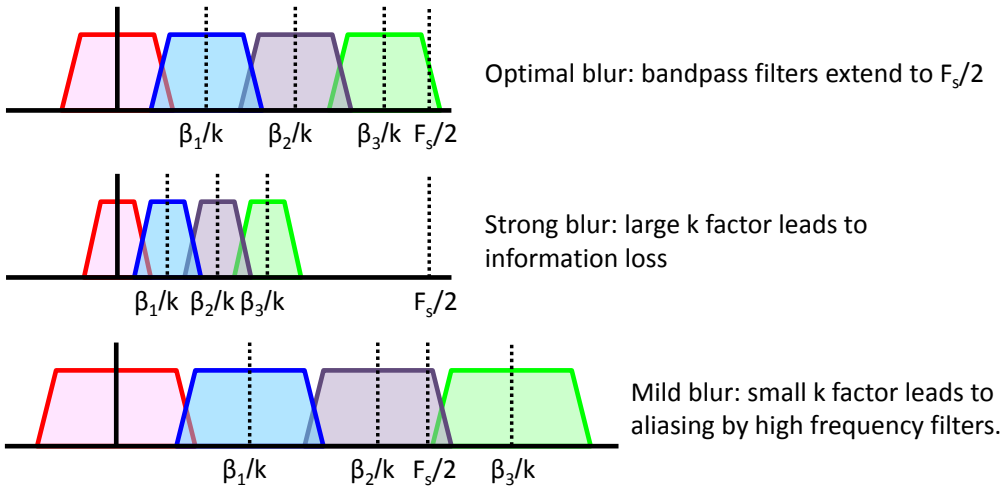

Figure 6.6: Lens aperture controls filter bandwidth relative to center frequency.

In a conventional image sensor, reducing lens aperture D provides a method to recover spectral content lost through defocus blur. This bandwidth increase comes at the cost of less gathered light. For an angle-sensitive pixel array, decreasing lens aperture increases each filter's bandwidth relative to its center frequency, rather than setting the maximum recovered spatial frequency. This allows for independent control of bandwidth from center frequency in this set of spatial bandpass filters, as shown in Fig. 6.6. An optimal choice of lens aperture ensures appropriate overlap between adjacent bandpass filters and a smooth response across the entire spatial frequency band of interest. Choosing too wide an aperture generates unwanted notches between adjacent filters, while an aperture that is too narrow incurs significant overlap and corresponding frequency ripple.

In summary, the bandpass nature of an angle-sensitive pixel array results in robustness to changes in optical system parameters. Furthermore, it loosens the traditional tradeoff in lens aperture between light gathering ability and sampling

bandwidth. An image sensor employing a full, 2D array of angle-sensitive pixels will have unique imaging abilities and accompanying design considerations.

6.6 Implications for angle-sensitive imaging

The preceding analysis projected the imaging system into a single dimension, where a set of N uniformly spaced bandpass filters spans the desired maximum spatial frequency. In two dimensions, each bandpass filter covers a disc in 2D frequency space and the corresponding sampling constraint is that the bandpass filters cover the area corresponding to the maximum 2D spatial frequencies. For a given grating orientation shared by angle sensitive pixel pairs, different angular sensitivities result in bandpass filters with spectral response aligned along the axis perpendicular to grating orientation. By choosing different grating orientations as well as angular sensitivities, we can create the block of angle sensitive pixels in Fig. 6.7, which for proper scaling factor k and aperture D cover the frequency space of interest.

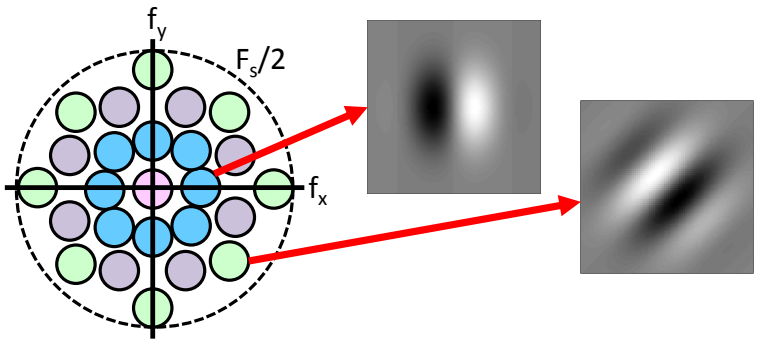

Figure 6.7: Bandpass sampling in two dimensions. Each bandpass filter corresponds to a disc, and an optimal set of filters (two shown) evenly tiles the area corresponding to the maximum recoverable spatial frequency.

We mathematically explore the concept of a block of angle-sensitive pixels forming a set of bandpass filters by considering the relationship of Eq. 11. Angle-

sensitive pixels compute a response which is similar to one entry in a windowed 2D Hartley Transform. Closely related to the Fourier transform, the Hartley transform is defined in two dimensions as [131, 132]

$$H(a,b) = \frac{1}{\sqrt{2}} \iint h(x,y) \left[\cos\left(ax+by\right) + \sin\left(ax+by\right)\right] \, \mathrm{d}x \, \mathrm{d}y \tag{6.12}$$

Setting α to zero, we find that the pair of pixels with response of Eq. 6.10 provides the cosine term in the transform integral. The sine term is also necessary, as the cosine functions only cover one side of the Fourier domain: both in-phase and quadrature responses are required to distinguish side-bands for each bandpass filter. To generate the complete Hartley transform response, we introduce a second pair of angle-sensitive pixels identical except with values of α shifted by $\pi/2$ to generate the required anti-symmetric term. The response difference between these additional pixels will have the integral form

$$\begin{aligned} V\left(i,j\right) = \int_{\Delta x_1}^{\Delta x_2} \int_{\Delta y_1}^{\Delta y_2} A\left(\frac{\Delta x}{k}, \frac{\Delta y}{k}\right) \sin\Bigg(\frac{\beta \sin\psi}{k}\Delta y \\ + \frac{\beta\cos\psi}{k}\Delta x + \alpha\Bigg) S\left(Mi + \Delta x\right) \, \mathrm{d}\Delta y \, \mathrm{d}\Delta x \end{aligned} \tag{6.13}$$

Taken together, these four angle-sensitive pixels, each with identical response frequency β but distinct phase offsets α separated by $\pi/2$ compute a complete entry in a 2D Hartley transform, windowed by the aperture function A.

With the appropriate set of angle-sensitive pixels with different frequencies β and orientations ψ evenly tiling frequency space, we obtain a full, windowed 2D block Hartley transform on the visual scene $S(x,y)$. The size of the transform block is set by the maximum spatial frequency we want to recover: higher spatial frequencies require larger blocks and therefore more angle-sensitive pixels to form a full set. The Hartley transform nature of the bandpass responses provides two

significant benefits. The first is that windowed sinusoidal transforms intrinsically provide a sparse output in response to natural scenes. This energy compaction property is useful for image compression or noise removal [132]. The second is that the Hartley transform is self-invertible, which provides a simple method to reconstruct an image from a set of bandpass filter outputs generated by an image sensor composed of angle-sensitive pixels.

The output of each pair of angle-sensitive pixels is one component of a spatial transform whose frequency is scaled by the degree of defocus k. Given an out-of-focus image V, self-invertibility implies that we can reconstruct the original scene by simply multiplying each pixel output $V(i,j)$ with the appropriate, scaled angular transfer function and summing together all contributions. This reconstruction $\hat{S}$ is a computationally refocused image and is expressed concisely with the double sum

$$\hat{S}(x,y) = \sum_i \sum_j V(i,j) h_{ij}\left(\frac{x-i}{k}, \frac{y-j}{k}\right) \tag{6.14}$$

where

$$h_{ij}(\theta,\phi) = A_{ij}(\theta,\phi)\left[1 - m_{ij}\cos\left(\beta_{ij}\sin(\psi_{ij})\phi + \beta_{ij}\cos(\psi_{ij})\theta + \alpha_{ij}\right)\right] \tag{6.15}$$

is the angular transfer function of the angle-sensitive pixel at location (i,j).

Accurate refocus requires prior knowledge of the degree of defocus k so that the transfer functions can be properly scaled. This factor can be computed directly from the differences between pairs of pixels. Assuming that the bandwidth of the scene $2\Omega_{\text{max}}$ is large relative to the bandwidth of the bandpass filters, the convolution integrals of Eq. 6.11 and Eq. 6.13 can be approximated as producing scaled sinusoids. We approximate the response of Eq. 6.11 with

$$P = W\cos\left(\beta\frac{\Delta x}{k}\right) \tag{6.16}$$

which represents the "in-phase" response and Eq. 6.13 with

$$Q = W \sin\left(\beta \frac{\Delta x}{k}\right) \tag{6.17}$$

which represents the "quadrature" response. The leading constant W is some weighting factor dependent on the integral. We can recover k by computing

$$\begin{aligned} \frac{\frac{dQ}{d\Delta x}P - \frac{dP}{d\Delta x}Q}{\left(\frac{dQ}{d\Delta x}\right)^2 + \left(\frac{dP}{d\Delta x}\right)^2} &= \frac{\frac{\beta}{k}W^2\cos^2\left(\beta\frac{\Delta x}{k}\right) + \frac{\beta}{k}W^2\sin^2\left(\beta\frac{\Delta x}{k}\right)}{\left[\frac{\beta}{k}W\sin\left(\beta\frac{\Delta x}{k}\right)\right]^2 + \left[\frac{\beta}{k}W\cos\left(\beta\frac{\Delta x}{k}\right)\right]^2} \\ &= \frac{k}{\beta} \end{aligned} \tag{6.18}$$

This is a local calculation, where the derivatives are the difference of adjacent responses in the angle-sensitive pixel array, taken along the orientation of the angle-sensitive pixel. As the factor k depends on distance to the object plane Z_o, Eq. 6.18 additionally provides a simple depth measurement relative to the focal plane.

6.7 Experimental results

Figure 6.8(a) is a microphotograph of a fabricated digital image sensor chip containing 153,600 angle-sensitive pixels and associated readout circuitry [110]. The pixels are divided into 64 different angular responses, with four different response frequencies β, four phases α, and four orientations α, and are uniformly tiled across the pixel array. In addition, we have also shown in Fig. 6.8(b) a close-up image of the pixel array, illustrating the diffraction gratings used for the angle-sensitive pixels, with different orientations and grating spacings for achieving distinct angular transfer functions. We used this camera chip with a fixed-focus camera lens (Nikkor f=50mm, F#=1.8) to perform imaging experiments. Target objects were placed

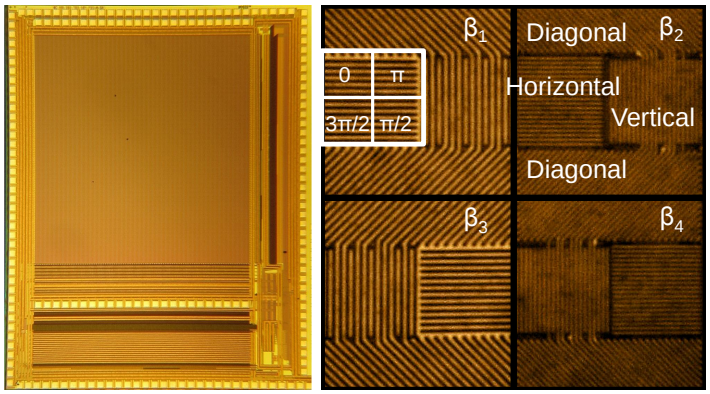

(a) (b)

Figure 6.8: (a) Photograph of fabricated image sensor containing 153,600 angle-sensitive pixels and associated readout circuitry. (b) Close-up image of pixel array with different angle-sensitive pixel types labeled.

at a distance of one meter from the lens, and white LEDs provided a controlled illumination source.

To test the filtering properties of angle-sensitive pixels, we chose the ray pattern of Fig. 6.9(a) as a first test image. The ray pattern displays alternating light and dark segments and contains a broad spectrum of spatial frequencies, arranged concentrically. The center of the diagram corresponds to high spatial frequencies, while the rim of the diagram contains low spatial frequencies. Furthermore, as the light and dark bands are arranged radially, different orientations at the same spatial frequency are also present.

We expect that these different frequencies and orientations will preferentially elicit strong responses in specific angle-sensitive pixels which have matching angular transfer functions. We recorded a single image with our angle-sensitive imager, and subtracted the responses of complementary angle-sensitive pixels to generate 32 distinct bandpass filter outputs. These outputs are shown in Fig. 6.9(b), divided by angular sensitivity and orientation. Low values of angular sensitivity β correspond to low spatial frequency bandpass filters and a strong selective response

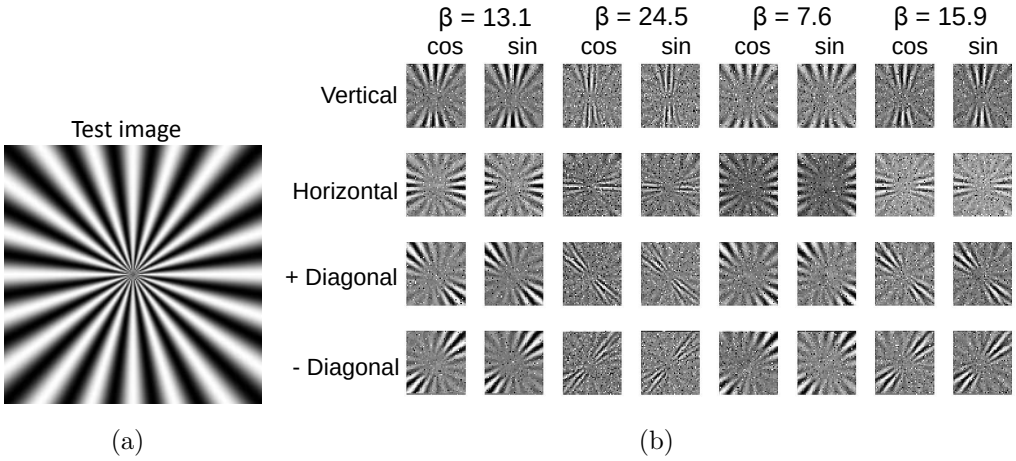

Figure 6.9: (a) Radial pattern test image. (b) Example bandpass filter outputs generated from ray test image by taking differences of angle-sensitive pixel pairs.

to the rim of the ray diagram. In contrast, high values of angular sensitivity β corresponding to high spatial frequency bandpass filters which respond near the center of the ray diagram.

The analysis of Section 6.5 indicates that the center spatial frequency and the bandwidth of the angle-sensitive pixel based bandpass filters scale with the factor k. To test this prediction, we chose a small block labeled with the word "near" as a test image. An in-focus image taken with the angle-sensitive image sensor is shown in Fig. 6.10(a). Under this condition, the image sensor lies in the image plane, such that $Z = Z_i$, and k is zero. As we adjust the focus of the camera lens and alter the position of the image plane relative to the position of the camera chip, the magnitude of k increases. Images captured at three different degrees of defocus are shown in Fig. 6.10(b), illustrating the increasing blur as scaling factor k increases. We have also shown the magnitude of the responses of two individual angle-sensitive pixel types and the base light intensity as a function of frequency in Fig. 6.10(b), up to the limit of the spatial Nyquist frequency set by pixel pitch. As blurring increases, the bandwidth and the center frequency of the response

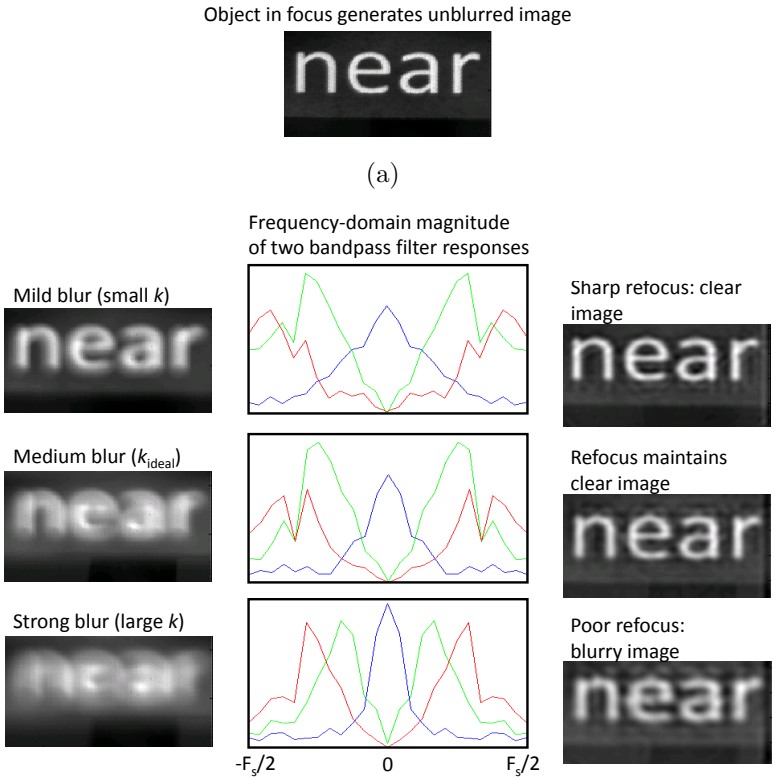

Figure 6.10: (a) In-focus test image of "near". (b) Increasing lens defocus results in increased image blur. (c) Filter responses shown for bandpass filters corresponding to $\beta = 13.1$ (green) and $\beta = 24.5$ (red) as well as low-pass filter from pixel response sum (blue). (d) Image refocus degrades when the bandpass filters no longer span the full spatial frequency spectrum.

magnitude decreases as predicted.

For the mild and medium blur cases of Fig. 6.10, the frequency response plots show that a strong response extends to the Nyquist limit. Performing image refocus by inverting the spatial Hartley filtering operation to obtain the images of Fig. 6.10(d), we observe that little degradation is observed for both of these cases relative to the in-focus image, as the set of bandpass filters spans the required spatial sampling bandwidth. Only with strong defocus do we observe significant resolution degradation from loss of image information, because the frequency span of

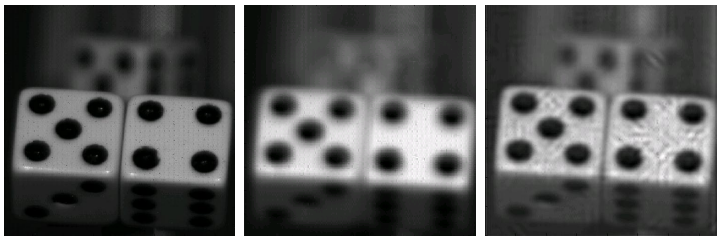

(a) (b) (c)

Figure 6.11: Refocus on more complex scenes. (a) Image with foreground dice in focus. (b) Moving camera focal plane in front of foreground blurs image. (c) Same picture of (b), computationally refocused.

the highest spatial frequency bandpass filter is significantly less than the sampling bandwidth.

The information recovery from the bandpass filters to perform image refocus has been successfully applied to more complex scenes. An in-focus image of a scene containing three dice is shown in Fig. 6.11(a). Intentional defocus of the camera lens results in the blurred image shown in Fig. 6.11(b). However, using the spatial filtering properties of angle-sensitive pixels, image refocus has restored the contrast of the two foreground dice and the legibility of the background die faces in Fig. 6.11(c).

To properly scale the angular transfer functions for the image refocus of Figs. 6.10 and 6.11, we must recover the degree of defocus k from a captured image. For each set of 4 angle-sensitive pixels sharing the same orientation and frequency in the array, we compute the difference in response between pairs having α's different by π. As sets of these pixels are tiled uniformly across the image sensor, this operation produces two subsampled images which represent the signals P and Q of Eqs. 6.16 and 6.17 for our visual scene and imaging system. We approximate the derivatives necessary for computing scaling factor k, $\mathrm{d}P/\,\mathrm{d}\Delta x$ and $\mathrm{d}Q/\,\mathrm{d}\Delta x$, by taking differences between the responses generated by adjacent sets of pixels along

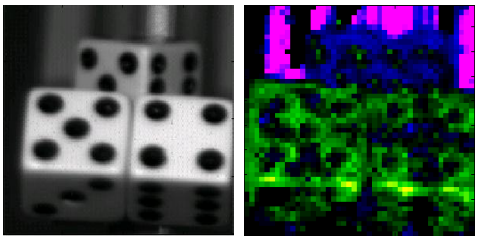

(a) (b)

Figure 6.12: Depth map computation. (a) Image captured from angle-sensitive camera chip. (b) Computed depth map showing that, relative to the camera's focal plane, the foreground dice are closer (green color), while the third background die is farther (blue). Features in the background are much further, represented with magenta.

the axis perpendicular to grating orientation. Because pixel locations (i, j) directly map to spatial positions (x, y) scaled by the magnification factor, we estimate the spatial coordinate derivatives with pixel coordinate derivatives. This procedure introduces a constant scaling factor which is immediately normalized during final computation and therefore does not affect the result.

Equation 6.18 lets us determine the amount of defocus seen by our chosen set of 4 pixels, permitting appropriate scaling for the angular transfer function at these pixels and additionally providing a local depth estimate. Using the four different pixel response orientations implemented for each response frequency β, we obtain four range estimates. To combine these independent results and generate a composite estimate, we separately compute the numerator and denominator of Eq. 6.18 for each orientation and sum them across different orientations. The ratio of the summed numerator and denominator provide us with our final estimate. This procedure automatically favors results which have high signal-to-noise ratio. An example of a depth map created in this fashion is shown in Fig. ch6fig:dicedepth, where green represents distances less than Z_o, and blue represents distances greater than Z_o.

6.8 Conclusion

We have presented a mathematical framework for analyzing the behavior of a recently developed class of sensor pixels known as "angle-sensitive pixels". These pixels have an oriented, periodic sensitivity to the incident angle of the light they see. This periodic sensitivity to angle translates to the application of a spatial bandpass filter with specific orientation and frequency when we use angle-sensitive pixels to acquire an image. Equivalently, angle-sensitive pixels provide signals which are the result of computing components of a 2D windowed block Hartley transform in the optical domain. The transform-based nature of angle-sensitive pixel imaging enables an efficient approach to 3D imaging by simplifying the image processing necessary for performing image refocus and computing range maps. We have demonstrated both of these operations with an existing angle-sensitive image sensor in conjunction with a conventional camera lens. By capturing a richer description of the light they see while remaining compatible with existing optical systems, angle-sensitive pixels provide an alternative, low cost and low complexity approach to image capture for a variety of imaging tasks.

Chapter 7
Optical flow computation

7.1 Introduction

Given a sequence of images in time, optical flow [133] describes the apparent motion of the visual world relative to the camera. Motion of objects in the visual world is a rich source of information for an observer, and measuring this motion field is important in a variety of applications from video compression to object tracking and avoidance. We demonstrate an image sensor which acquires information about object motion and enables efficient computation of optical flow directly from captured images. The sensor utilizes angle-sensitive pixels which act as spatial Gabor filters as a result of their periodic sensitivity to the incident angle of the light they see.

The most commonly used approach for estimating the optical flow field from an image sequence relies on temporal and spatial local derivatives of scene intensity [134]. VLSI systems in CMOS have been demonstrated which integrate these differential motion calculation algorithms with conventional image sensor pixels [135]. Unfortunately, as these systems rely on numerical approximations for derivatives of scene intensity, they are highly sensitive to noise and non-uniform illumination. Furthermore, 3D optical flow calculation is difficult as intensity patterns blur when objects move away from the camera's optical plane of focus.

An alternative technique for estimating optical flow depends on phase differences from quadrature-pair filters such as Gabor filters [136, 137]. A Gabor filter characterizes an image in terms of magnitude and phase at a particular frequency. Motion over time results in a change in the phase of the filter response over time. Although these phase-based methods for optical flow provide good

performance [138], they incur a significant resource cost compared to gradient-based methods as calculating filter responses is computationally intensive. Angle-sensitive pixels, however, compute these filter responses in the optical domain using zero power and hence provide sufficient information on scene structure to directly measure optical flow either with or without a lens.

7.2 Background theory

Angle-sensitive pixels (ASPs) [28] are pixel scale structures which respond to both the intensity and incident angle of the light they see. They achieve angle sensitivity through the Talbot effect, a diffractive phenomenon where incident light striking a periodic diffraction grating generates intensity patterns with identical periodicity behind the grating. These patterns shift laterally with changes in incident angle. A second diffraction grating placed below, called an analyzer grating, alternately blocks or passes the periodic intensity patterns as they shift in response to incident angle. A photodiode placed below the stacked diffraction gratings therefore acquires a periodic sensitivity to incident angle, as shown in Fig. 7.1. For a fixed intensity, we model this periodic response R to incident angle θ with the expression

$$R(\theta) = A(\theta)(1 + m\cos(\beta\theta + \alpha)) \tag{7.1}$$

The geometry of the gratings determines the parameters m, β, and α in the response, while $A(\theta)$ is a function modeling finite aperture effects, which we approximate with a Gaussian. To distinguish between changing incident intensity and incident angle θ, we use a pair of complementary responses with identical m and β, but with α values of 0 and π. The difference between these pixel responses is

$$g(\theta) = 2mA(\theta)\cos(\beta\theta) \tag{7.2}$$

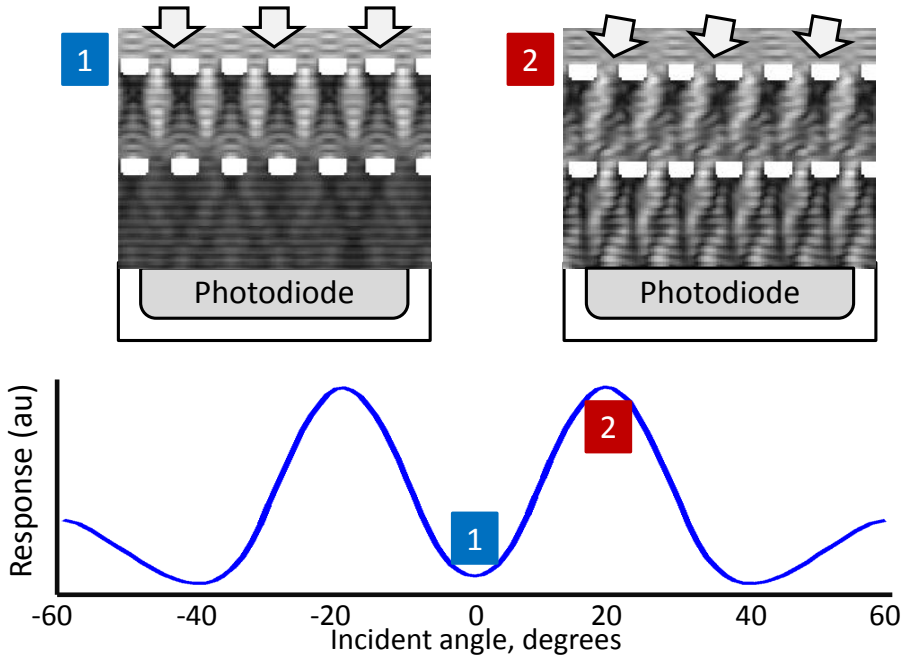

Figure 7.1: An angle-sensitive pixel relies on diffractive optics to achieve a periodic response to incident angle.

An additional pair of complementary quadrature responses with $\alpha = \pi/2$ and $\alpha = 3\pi/2$ provides more information on the periodic response, with a difference of

$$h(\theta) = 2mA(\theta)\sin(\beta\theta) \tag{7.3}$$

We achieve the required responses with distinct α values by laterally shifting the analyzer grating relative to the diffraction grating. Figure 7.2 illustrates this lateral shift used to generate the two complementary quadrature pairs of angle-sensitive pixels, as well as a simulated pair of response differences to incident angle.

This periodic sensitivity to changes in incident angle provides a means to compute spatial filter responses in the optical domain, significantly simplifying phase-based optical flow measurement. We consider a 1-dimensional visual scene, described by intensity $I(x)$, placed a distance z in front of a quadrature set of four

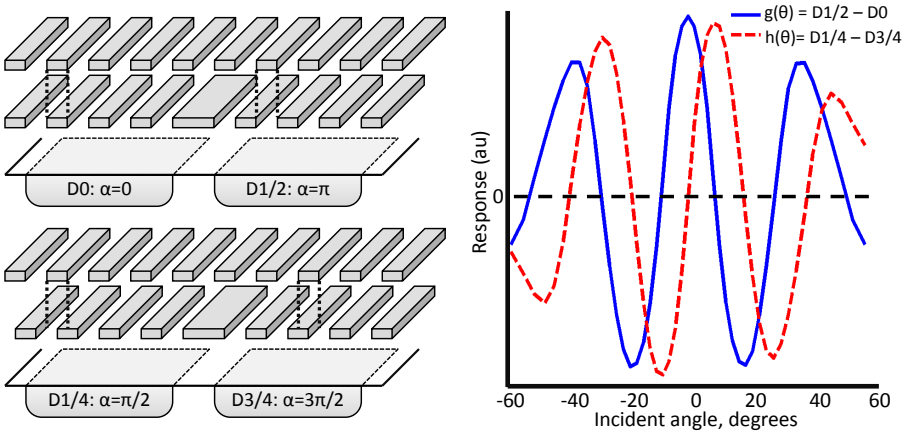

(a) (b)

Figure 7.2: a. Pairs of complementary angle-sensitive pixels with different α values. b. Difference in complementary responses results in a quadrature description of incident angle.

angle-sensitive pixels. Each pixel integrates incident light from the entire scene, weighted by its characteristic sensitivity to incident angle (Fig. 7.3). Using the small-angle approximation $\tan(\theta) \approx \theta$, spatial position x maps to incident angle θ with the relation $\theta = x/z$. Therefore the pair of complementary pixels which have the response difference of Eq. 7.2 have the output

$$P = 2m \int I(x) A\left(\tfrac{x}{z}\right) \cos\left(\tfrac{\beta x}{z}\right) dx = \int I(x) g\left(\tfrac{x}{z}\right) dx \tag{7.4}$$

Similarly, the quadrature pair of pixels with the response difference of Eq. 7.3 will have the output

$$Q = 2m \int I(x) A\left(\tfrac{x}{z}\right) \sin\left(\tfrac{\beta x}{z}\right) dx = \int I(x) h\left(\tfrac{x}{z}\right) dx \tag{7.5}$$

The two output differences P and Q are the results of applying a quadrature pair of spatial bandpass filters, with impulse responses of $g(x/z)$ and $h(x/z)$, to the scene $I(x)$. As the aperture function $A(\theta)$ can be modeled as a Gaussian, these four angle-sensitive pixels form a pair of quadrature Gabor spatial filters with center frequency of β/z. Scene motion such as that in Fig. 7.4 results in a

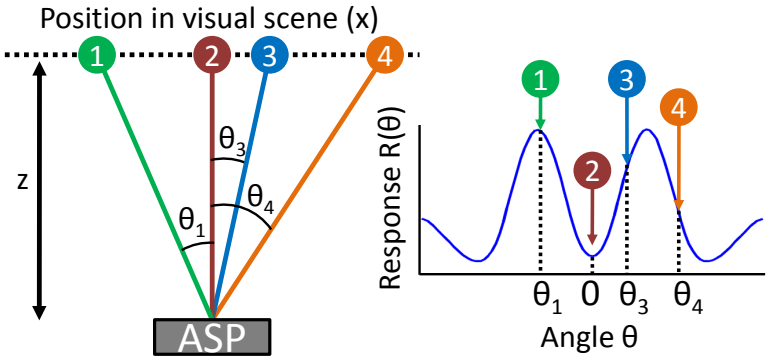

Figure 7.3: An angle-sensitive pixel provides an output which corresponds to a superposition of all incident light from the scene, weighted by the incident angle-dependent response.

response tradeoff between the cosine $g(x/z)$ and sine $h(x/z)$ Gabor filter responses and therefore corresponds to a phase shift in time.

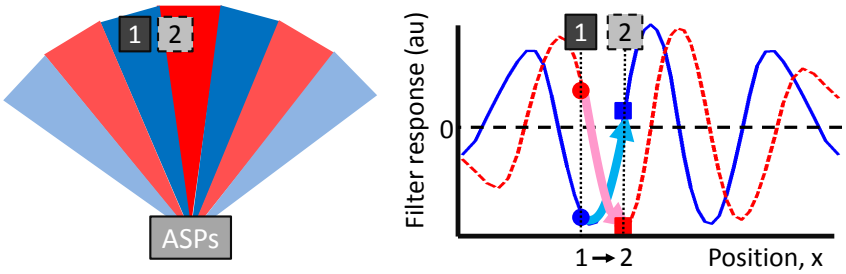

Figure 7.4: a. Periodic sensitivity of angle-sensitive pixels projects to a spatial Gabor filter (blue and red areas) with a specific frequency. b. Object motion from position 1 to 2 results in a phase shift in filter responses.

If the bandwidth of the bandpass filters is narrow relative to the bandwidth of the visual scene, the integrals P and Q representing filter output are well approximated by the impulse responses g and h, respectively. Therefore, the time derivatives of the two output differences can be described with the time derivative of the in-phase bandpass filter response, $g = m\cos(\beta x/z)$, and quadrature

response, $h = m\sin(\beta x/z)$. Assuming a fixed depth z, we have

$$\frac{dP}{dt} \approx \frac{\partial g}{\partial t} = -m\sin\left(\frac{\beta x}{z}\right)\frac{\beta}{z}\frac{dx}{dt}$$
$$\frac{dQ}{dt} \approx \frac{\partial h}{\partial t} = m\cos\left(\frac{\beta x}{z}\right)\frac{\beta}{z}\frac{dx}{dt}$$

Using the trigonometric identity $\sin^2(\theta) + \cos^2(\theta) = 1$, we find that the following expression recovers the desired lateral motion term $\partial x/\partial t$ from pixel output differences P and Q.

$$\frac{dx}{dt} = \frac{z}{m^2\beta}\left(P\frac{dQ}{dt} - Q\frac{dP}{dt}\right) \tag{7.6}$$

The differences between outputs for a single set of four angle-sensitive pixels provide outputs P and Q in response to a visual scene. As the scene changes in time, we use Eq. 7.6 to compute overall scene motion in the x direction. An additional set of four angle-sensitive pixels, oriented in the y direction, is necessary to extract overall 2D velocity. Therefore, computation of overall 2D scene motion only requires eight angle-sensitive pixels and simple computation, without any additional optics.

When using angle-sensitive pixels without a lens, their spatial bandpass responses span the entire visual scene. To perceive local scene motion, we use a lens (Fig. 7.5) to limit the extent of the visual scene to which a group of angle-sensitive pixel responds. Incident angle θ at the sensor maps to a spatial position $x \approx k\theta$ in the visual scene, where $k = Z\Delta F/F$. The mechanical arrangement of sensor relative to optics sets the parameters ΔF and F, while Z is the distance from the lens to the visual scene. As a consequence of the finite range of angles admitted by the lens aperture D, each angle-sensitive pixel in the array only integrates intensity over a limited spatial region. This has the effect of scaling the resulting spatial bandpass filter responses, reducing them in size to the spatial region the pixels see.

An array of angle-sensitive pixels used with a lens will therefore compute spatial filter responses for different subregions of the visual scene. Motion in a particular

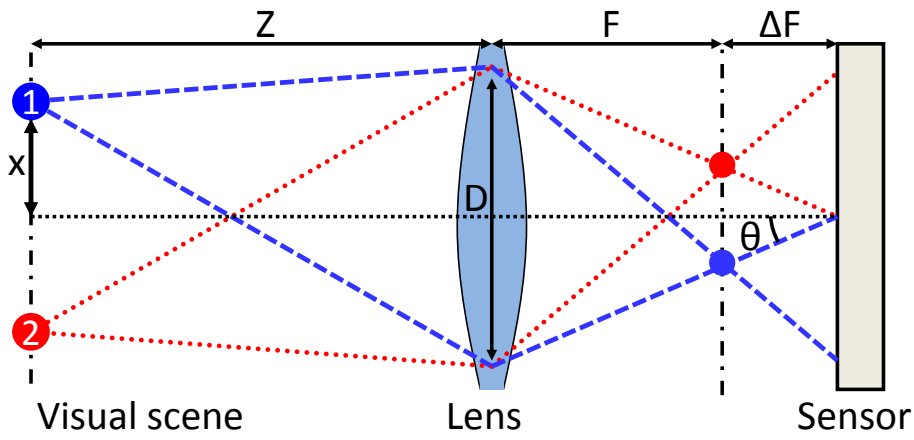

Figure 7.5: A lens objective with finite aperture restricts the range of incident angles shown to angle-sensitive pixels. This limits their response to a local region of the overall visual scene.

subregion will result in a phase shift for one pair of measured quadrature responses. Given these responses, Eq. 7.6 provides an estimate for this local motion. In contrast to lensless pixels, where the mapping between spatial position x and incident angle θ is $x \approx z\theta$, external optics results in the mapping $x \approx k\theta$. This necessitates substituting z of Eq. 7.6 with k to account for the scene scaling provided by the lens.

In addition, because ΔF depends on Z, finding $\partial(\Delta F)/\partial t$ provides an estimate for motion in the direction along the optical axis $\partial Z/\partial t$. Whereas measuring lateral motion requires only temporal derivatives of the filter responses, computing motion in z requires both temporal and spatial derivatives. This axial motion term can be found with

$$\frac{\partial Z}{\partial t} = \frac{\beta}{\Gamma^2}\left(Q\frac{\partial^2 P}{\partial t \partial x} - P\frac{\partial^2 Q}{\partial t \partial x}\right) \tag{7.7}$$

where Γ is a normalization term given by

$$\Gamma = \sqrt{\left(\frac{\partial P}{\partial x}\right)^2 + \left(\frac{\partial Q}{\partial x}\right)^2} = \frac{m\beta}{k} \tag{7.8}$$

The partial derivatives $\partial P/\partial x$ and $\partial Q/\partial x$ are estimated with differences in filter

outputs generated at adjacent positions in the array by nearby angle-sensitive pixels.

7.3 Results

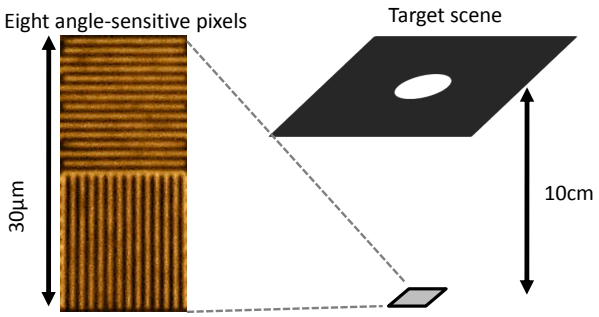

Figure 7.6: Using angle-sensitive pixels to measure gross scene velocity.

To demonstrate the use of angle-sensitive pixels as spatial bandpass filters for measuring optical flow, we used a block of 8 angle-sensitive pixels ($\beta = 13.1$ and $m = 0.51$) which provide two quadrature filter pairs, one oriented horizontally and the other vertically. This block of pixels occupied a total area of 15μm by 30μm. As shown in Fig. 7.6, we placed a white dot (2cm diameter) on a black background 10cm directly above the angle-sensitive pixels and measured the outputs of the 8 pixels while moving the dot both horizontally and vertically. Subtracting the outputs of complementary angle-sensitive pixel pairs produced the spatial bandpass filter responses. Scene motion such as a moving dot induces phase shifts over time in these responses, so we have used Eq. 7.6 to compute overall motion estimates in the x (horizontal) and y (vertical) directions.

As shown in Fig. 7.7, we observed good agreement between computed scene velocity from angle-sensitive pixel outputs and true velocity. For low speeds, our phase-based method using angle-sensitive pixel-based spatial bandpass filters is

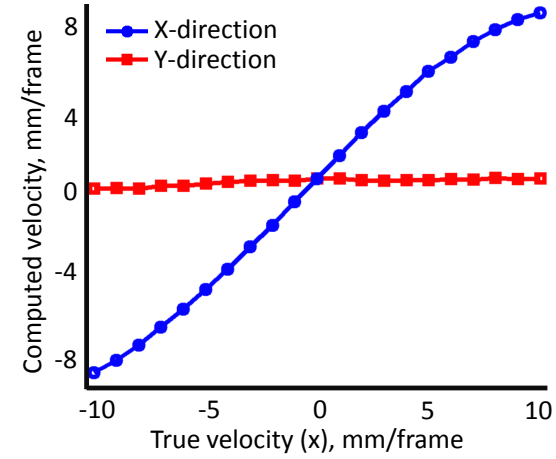

(a)

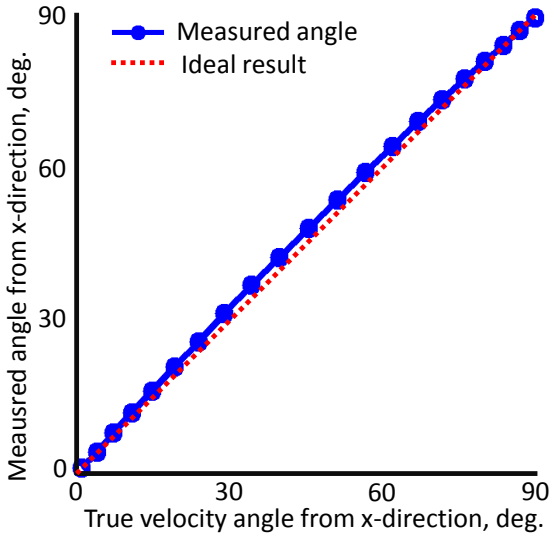

(b)

Figure 7.7: a. Measured velocity magnitude is monotonic in response to true object velocity. b. Computed direction using vertical and horizontal velocity components accurately reflects direction of motion.

linear in response to scene motion, but the response begins to saturate at higher velocities which approach a movement of 1cm between measurements. Furthermore, the direction of motion computed using the measured magnitudes of x- and y-velocity components matches closely with the true direction of scene motion.

For measuring velocity in different regions of a visual scene, we have used the

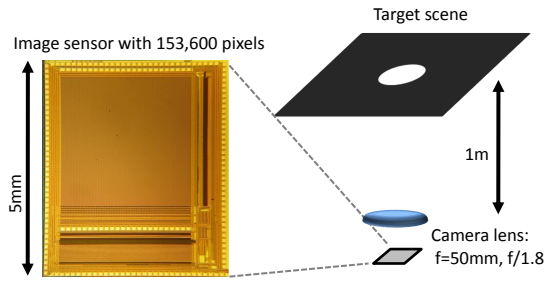

Figure 7.8: Using an angle-sensitive image sensor with camera lens to generate velocity fields for scene motion.

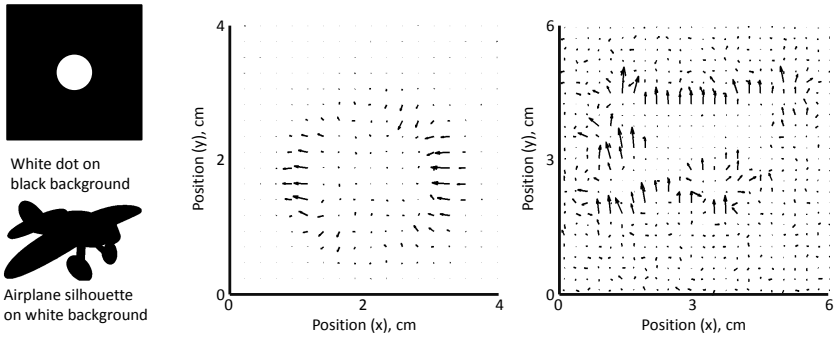

(a) (b) (c)

Figure 7.9: Demonstrating optical flow fields. a. Test images (white dot and black airplane) presented to the angle-sensitive pixel-based imager. b. Computed velocity field for white dot translating to the left by 0.5mm/frame. For clarity, the field has been subsampled. c. Computed velocity field for black airplane translating upwards by 0.5mm/frame.

angle-sensitive image sensor demonstrated in [110] which incorporates repeating tiles of 32 pairs of complementary angle-sensitive pixels. A conventional lens objective (Nikkor f=50mm, f/1.8) was used to limit the spatial scale of the resulting angle-sensitive pixel-based bandpass filters (Fig. 7.8). The aperture stop was set to maximum, corresponding to F# = 1.8. We used MATLAB to process sequences of captured images from the image sensor to generate vector flow fields.

We placed a white dot (2cm diameter) on a black background at a distance of 1m from the lens objective. Using a sequence of captured images and application

of Eq. 7.6, we obtain the 2D velocity field plotted in Fig. 7.9(b). As the spatial bandpass filters respond strongly to object edges, our optical flow estimation method only functions on object edges. With additional assumptions about the visual scene such as smoothness [134], the velocities computed from motion in object edges can be used to derive a full map of scene motion. When moving the dot in the z direction, we were able to measure velocity with a precision of 250 μm per frame with Eq. 7.7. We obtained similar results with an image of a black airplane on a white background, with an example velocity field shown in Fig. 7.9(c).

7.4 Conclusions

In this work, we have demonstrated using angle-sensitive pixels to estimate optical flow by taking advantage of their ability to function as spatial bandpass filters. By mapping their periodic sensitivity to incident angle onto visual scenes, angle-sensitive pixels compute filter responses in the optical domain. Because spatial motion translates to a phase offset over time in filter responses, we need only simple mathematical operations to compute accurate estimates of scene velocity. In summary, we have implemented a passive, hardware-based technique to solve the traditionally software-based problem of determining optical flow.

Chapter 8
Optical image compression

8.1 Introduction

Imaging systems typically combine an image sensor to digitize visual scenes with a subsequent transformation of the image into a sparser format for further processing. For example, image compression eases data storage or transmission requirements by applying an image transform, such as the discrete cosine transform (DCT), and rounding the resulting outputs. Many applications employ dedicated digital signal processors to compute 2D image transforms. Recent work has demonstrated image sensors which integrate transform calculations in the analog [13, 14] or digital [15] domain on a single chip. The image sensor presented here computes spatial Gabor transforms on chip in the optical domain, enabling efficient image processing in the backend circuits. Fabricated in 180nm digital CMOS, the chip requires only ambient light and a single camera objective to capture compressed images.

8.2 Background

Spatial Gabor transforms are a family of oriented, periodic 2D sinusoids with a Gaussian envelope, each of which acts as a bandpass filter in 2D frequency space. Figure 8.1 illustrates the convolution of the standard Lena test image with a single Gabor bandpass filter. Gabor transforms are frequently used in a diverse variety of applications from edge detection to image compression and object recognition [128] and also accurately model pathways in the vertebrate visual cortex [139].

Unlike the DCT employed in JPEG compression, the Gabor transform is not separable and cannot be computed using two sequential 1D filtering operations.

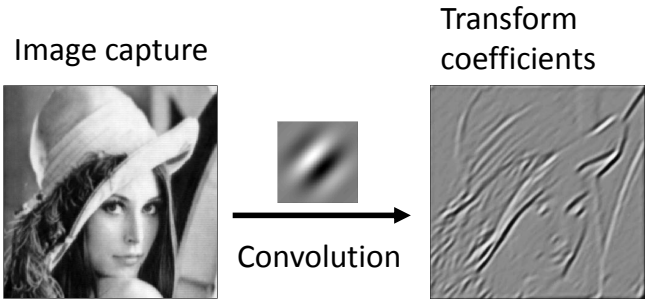

Figure 8.1: Gabor transforms involve a 2D convolution with a set of oriented, periodic filter kernels to generate a set of transform coefficients.

This is a significant drawback, as computing a full 2D convolution with a number of different filter kernels to obtain a transformed image requires considerable processing power. Our image sensor circumvents these operations by using the oriented, periodic response of angle-sensitive pixels [110] to perform the required spatial image transform in the optical domain.

8.3 System design

8.3.1 Optical design

Illustrated in Fig. 8.2, angle-sensitive pixels (ASPs) use a pair of local diffraction gratings with conventional active imager pixels and possess a periodic sensitivity to incident angle. Because the pixel output changes in response to both incident angle and intensity, we rely on pairs of complementary pixels to distinguish changes in incident angle from changes in intensity. These complementary pixel pairs, labeled A and B in Fig. 7.1, have different relative shifts between the diffraction gratings, and thus different angular responses. We treat the signals from these two pixels as a differential signal, where the differential mode encodes incident angle, and the common mode encodes light intensity.

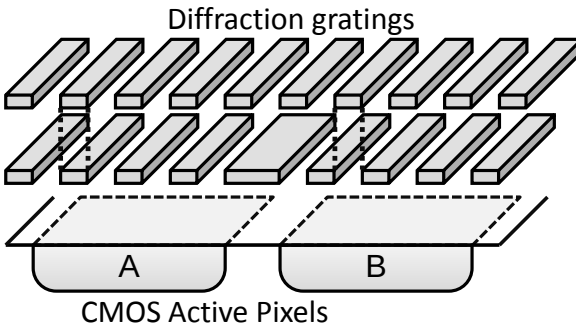

Figure 8.2: Angle-sensitive pixels combine diffractive optics with conventional photosensors and respond to incident angle.

To remove biases in this differential signal which result from the physical separation of complementary angle-sensitive pixels, we have utilized the common centroid layout of Fig. 8.3(a) to create an "optical differential pair." Measuring the output differential signal from this pair of ASPs, we obtain a windowed sinusoidal response like that shown in Fig. 8.3(b) to changes in incident angle along the axis perpendicular to the direction of the diffraction gratings. The geometry of the diffraction gratings controls the periodicity of the response, while the finite aperture of image-forming optics sets the width of the windowing function. Along the axis parallel to the diffraction gratings, only the windowing function appears in the angular response. This response can be described as a 2D Gabor filter operating on incident angle distributions [33].

When an image sensor is placed away from the focal plane of the imaging optics, as in Fig. 8.4(a), different spatial offsets of objects in a visual scene map to distinct incident angles. Consequently, the 2D Gabor filter response in angle generated by one optical differential pair projects to a 2D Gabor filter in the spatial domain (Fig. 8.4(b)). The geometry of the diffraction gratings utilized in the component angle-sensitive pixels sets the characteristic frequency, orientation, and phase of the filter response, and the aperture of the imaging optics control the envelope of

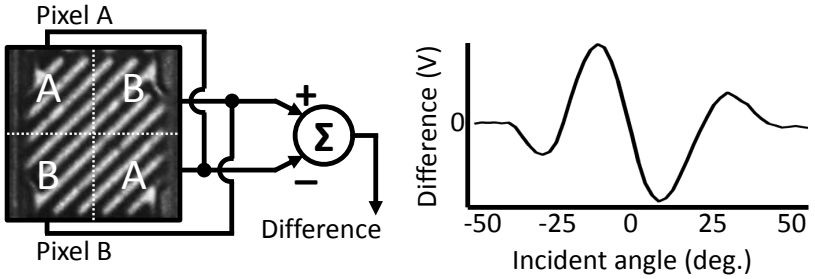

(a) (b)

Figure 8.3: The differential response of a) one pair of complementary angle-sensitive pixels is b) a periodic function of angle.

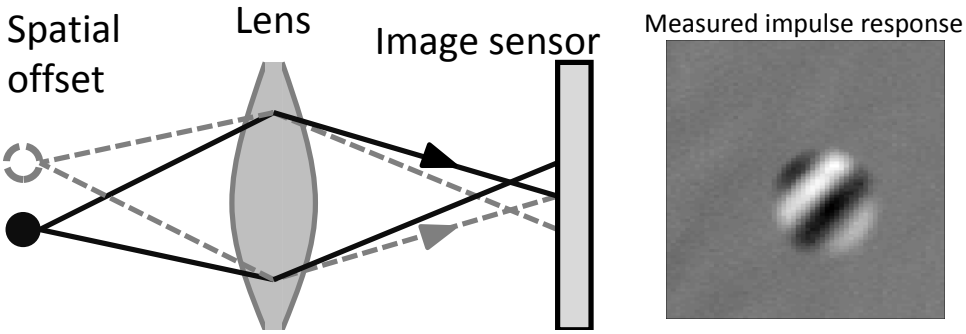

(a) (b)

Figure 8.4: A lens in a) an optical system maps spatial displacement to incident angle so that ASPs act as b) 2D Gabor filters in space.

the filter response. By using a variety of different complementary ASP pairs, each with a distinct geometry to provide a distinct transform coefficient, we obtain a full, low-order spatial 2D Gabor filter bank which implements a complete Gabor transform.

Figure 8.5 demonstrates the operation of this optically computed 2D spatial Gabor filter bank. Our implemented image sensor employs a tiled set of 24 optical differential pairs whose differential signals generate a set of 24 2D spatial Gabor filters with 3 frequencies, each of which has 4 orientations and 2 phases (sine and cosine). A micrograph of the pixel layout is shown in Fig 8.5(a), as well as a set of

measured impulse responses in Fig. 8.5(b) illustrating the response of each filter to a small white dot on a black background.

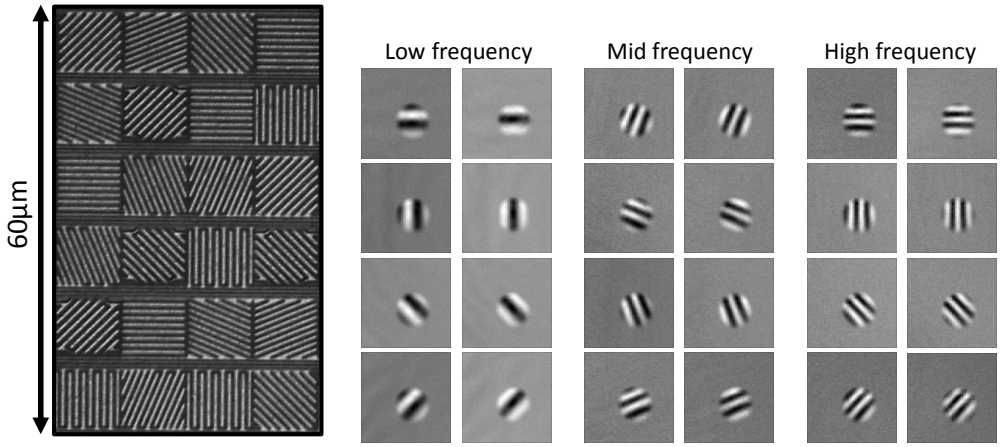

Figure 8.5: Implemented Gabor filter bank: a) 24 distinct angle-sensitive pixel designs generate spatial filters, with b) measured Gabor-like impulse responses.

8.3.2 Electrical design

Because Gabor filters efficiently compact the information found in a visual scene [128], they provide a good basis for image compression. Comparing a histogram of pixel-by-pixel values in the Lena test image with a histogram of the coefficients generated by convolving the image with a Gabor filter as in Fig. 8.6, we observe that many of the coefficients resulting from the filter operation are zero or near zero. By approximating the coefficients near zero as zero, and rounding the remaining nonzero coefficients to reduced precision, we reduce the number of bits required to encode an image relative to simply encoding each pixel-by-pixel brightness value at a fixed bit precision. The result of these two operations is a compressed image. Therefore, the readout back-end of our image sensor simply needs to round and approximate differential pixel signals to perform image compression. These

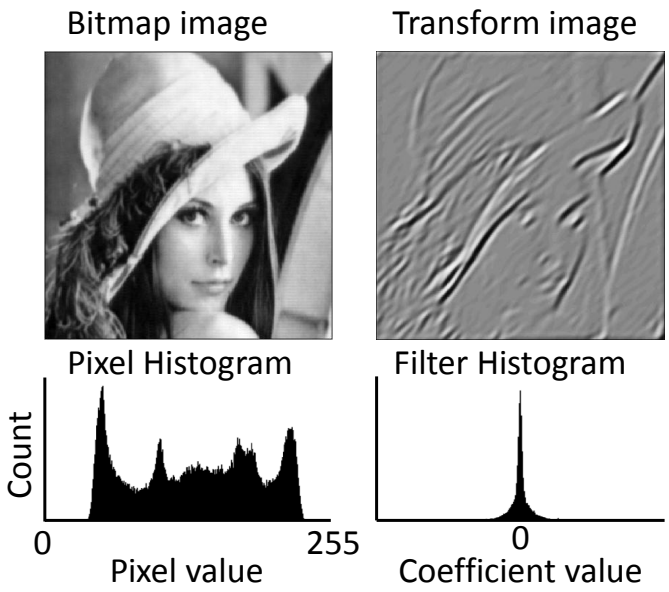

Figure 8.6: Gabor filter coefficients of an image are concentrated near zero.

circuits for image compression are simple and rely on the characteristics of our on-chip optical image transformations during the digitization process. By initially performing the image transform and filtering in the optical domain, we eliminate both the power consumed by analog or digital image transform circuits and the silicon area dedicated to implementing these computationally costly matrix operations. For image compression, these gains are particularly significant as a large number of transform outputs are simply discarded and never transmitted, wasting the resources dedicated to computing these results.

Each distinct Gabor filter resulting from the output of one selected differential optical pair uses one dedicated back-end readout channel, resulting in 24 Gabor filter outputs on the image sensor. The back-end channels incorporates a programmable gain differential amplifier, followed by a variable-resolution successive approximation ADC which has selectable "dead zone" which rounds near-zero inputs to zero.

Schematically shown in Fig. 8.7, the PGA has a differential architecture, tak-

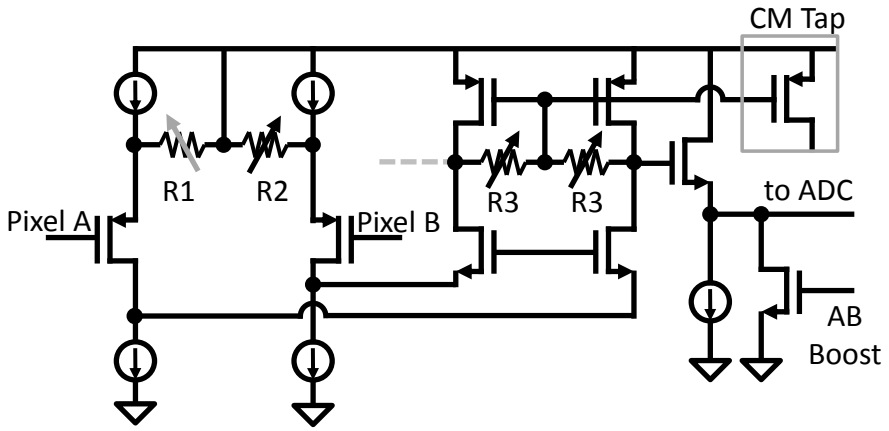

Figure 8.7: Schematic of programmable gain amplifier: resistors R1/R2 set imbalanced degeneration to correct common mode and R3 sets gain.

ing as inputs the outputs of a pair of complementary angle-sensitive pixels. Programmable load resistors (R3) provide 4 gain settings to account for the different signal gains of different filter designs and ensure effective utilization of the available ADC dynamic range. To cancel the poor common mode rejection of the optical differential pixel pair, we have employed programmable, imbalanced degeneration of the input transistors using resistors R1 and R2. The output of the amplifier is buffered with a class-AB source follower capable of driving a large voltage onto the ADC when necessary, while saving power for small signal swings.

While the differential mode signal from pairs of angle-sensitive pixels provide us with Gabor filter coefficients, the common mode signal encodes local scene brightness. To account for this additional information, each PGA has a current-based common mode output, shown as the common mode tap of Fig. 8.7. Since we rely on each block of 24 optical differential pairs of Fig. 8.5(a) to provide the necessary set of filter outputs, we sum the common-mode current across all 24 amplifier channels and digitize the result with its own dedicated ADC for a 25th, spatial low-pass filter output providing a measure of scene brightness seen by the

full optical filter block.

The variable resolution differential charge-redistribution successive approximation ADC of Fig. 8.8 performs N+1 comparisons for each N-bit conversion. The first two comparisons bracket a "dead zone" around differential zero. If the filter output falls in this zone, the conversion terminates, and the output is rounded to zero. This operation has been shown to efficiently quantize image information [140]. If the input falls outside this "dead zone" the MSB is set and the conversion continues, generating a digital value with a resolution between 5 and 8 bits. Measured transfer curves of the ADC confirm a programmable, symmetric dead zone range of 0 to 650mV. Offset corrections of up to the full range of the ADC can also be programmed dynamically into each ADC to compensate for input offsets from the converter or from the preceding pixel and amplifier circuitry.

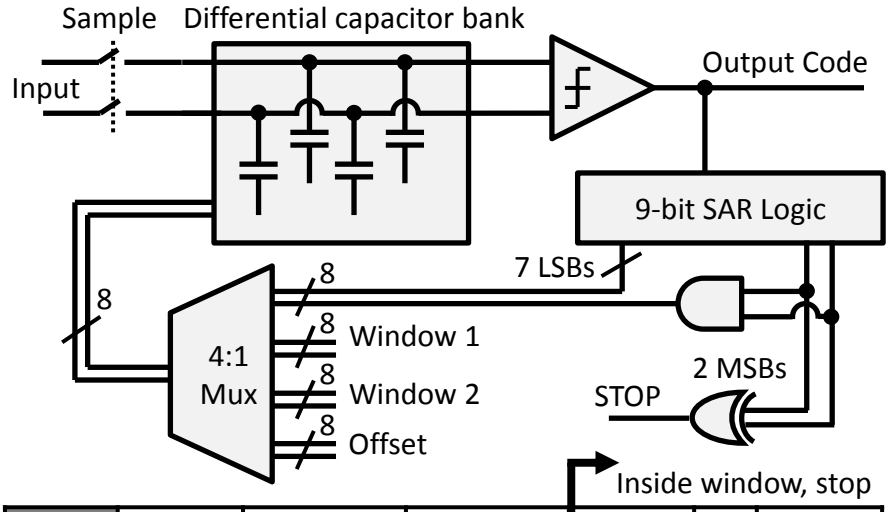

Cycle	Sample	1	2	3	....	9
Mux	Offset	Window 1	Window 2	SAR	....	SAR

Figure 8.8: Block diagram of programmable, variable-resolution SAR ADC.

A complete block diagram of the image sensor is shown in Fig. 8.9. The pixel array of the image sensor is a 96x64 array of the 24 filter blocks shown in Fig. 8.5(a),

corresponding to an array of 384x384 filters, for a total of 295,000 angle-sensitive pixels arranged in common-centroid optical differential pairs. The 25 readout paths operate in parallel, amplifying and digitizing the spatial bandpass filter and local intensity outputs simultaneously. Compared to the common-mode intensity and low spatial frequency filters, the higher frequency filters are intentionally designed with a lower maximum resolution of 7 bits, reflecting the reduced high spatial frequency content seen in natural scenes [141]. The fabricated chip (Fig. 8.10) is manufactured in TSMC's 180nm logic CMOS process, measures 25mm^2 in area and consumes 2 mW from a 1V(digital)/1.8V(analog)/3.3V(pixel) supply at a frame rate of 15fps.

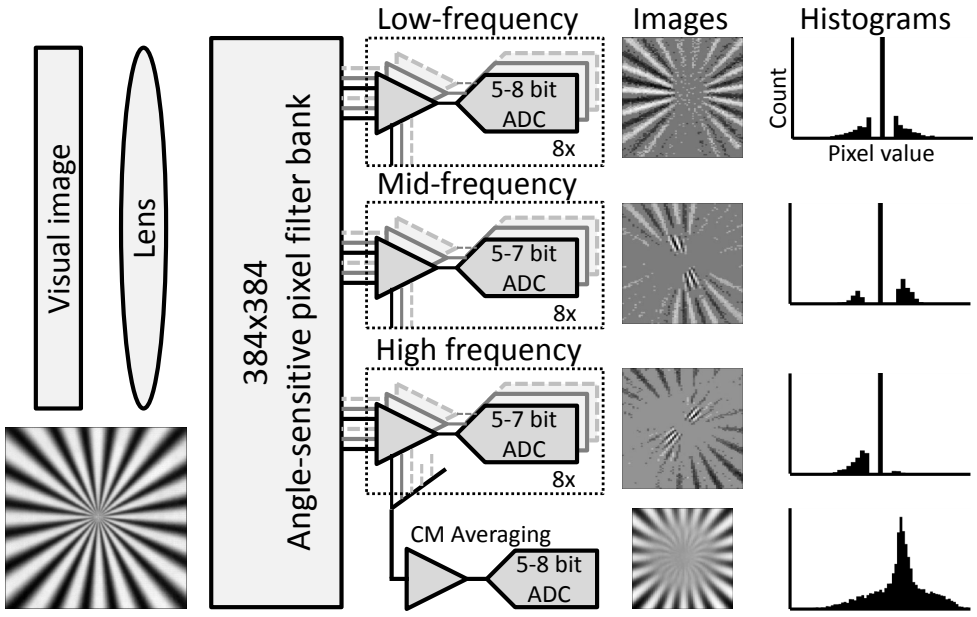

Figure 8.9: Top-level block diagram of imaging system.

8.4 Results

We demonstrated the capability of this transform based image sensor in Figure 8.11. A copy of the Lena test image was captured using a single Nikon camera

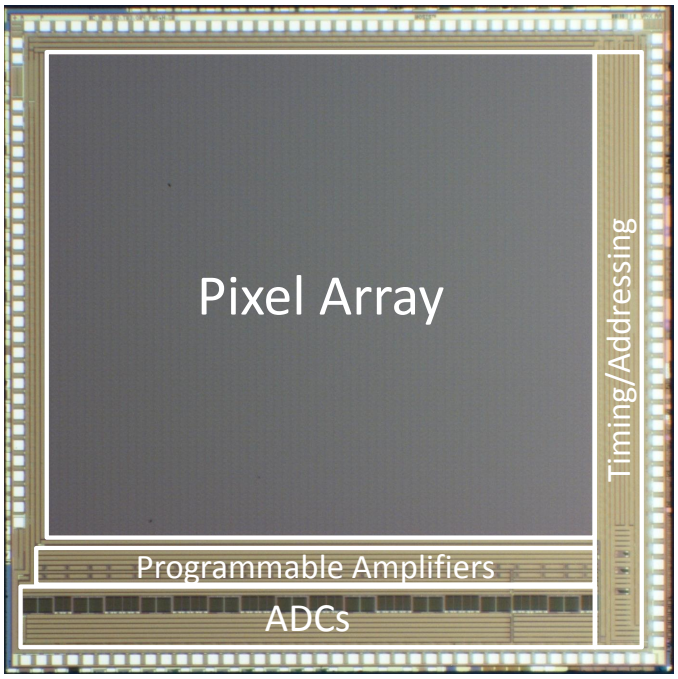

Figure 8.10: Die microphotograph.

lens (f=50mm, F#=1.8) under ambient white light scene illumination. Each of the 24 Gabor filter channels captures unique features from the scene, with three shown on the left in Fig. 8.11(a). The 25th lowpass filter channel, generated from the common mode output of the angle-sensitive pixels, captures local scene brightness as on the right in Fig. 8.11(a). Inverting these spatial transforms and summing generates an outlined version of the test image, shown second from left in Fig. 8.11(b). At a 5-bit resolution for the filter outputs, 90Kbits are required to digitize the nonzero coefficients of all 24 channels, with independently programmed "dead zones" for each channel.

When combined with the common mode channel, which requires 30Kbits at a resolution of 5 bits, we obtain the reconstructed image shown second from right in Fig. 8.11(b). The compressed image requires a total of 120Kbits of image data. In contrast, the same image, put in focus and captured by the same image sensor requires 1.2 Mbit to digitize the common mode of each individual angle-sensitive

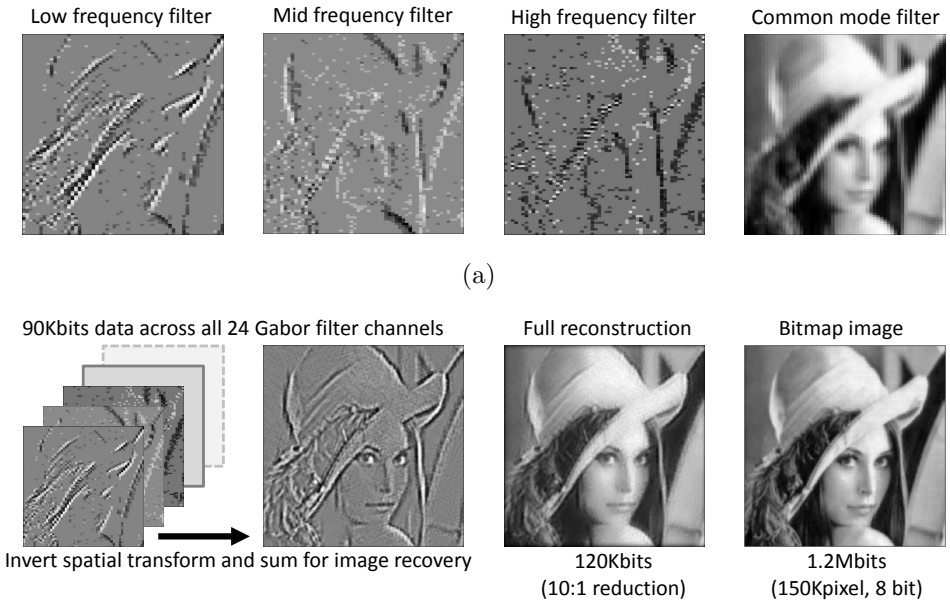

Figure 8.11: Demonstration of image sensor performing image compression. a) Representative outputs of image sensor when shown the Lena test image. Three of the 24 Gabor filter outputs, corresponding to different spatial frequencies, and the 25th common mode output, corresponding to local image brightness, are shown. b) Combining the 24 filter outputs (digitized using 90Kbits) and the common mode output (digitized with 30Kbits) generates a reconstructed image at a 10:1 data reduction compared to a raw bitmap image, while preserving significant image detail.

pixel pair to an accuracy of 8 bits. Comparing the image reconstructed from the compressed image data with the bitmap image, image data has been reduced by a factor of 10 without significant degradation in image quality.

8.5 Discussion

We have presented a CMOS image sensor which computes 2D spatial Gabor transforms in the optical domain and utilizes the resulting transform coefficients for image compression. Optical transform computation has the advantages of zero power consumption and drastically simplified system design, as we have elimi-

nated the power and cost of analog or digital circuits which must store filter coefficients and perform the requisite 2D convolution. Although we have demonstrated an image sensor back-end dedicated to image compression, other possible design choices which optimize the back-end processing for other image processing tasks, such as edge identification and feature recognition, are possible and will result in optoelectronic systems for a variety of imaging tasks.

Chapter 9
Conclusion

The work presented in this thesis provides only a first exploration of the development and design of optoelectronic CMOS image sensors employing angle-sensitive pixels. Opportunities for future advances and research remain on all fronts in these integrated systems. In particular, room for vast improvement is evident in three areas: physical device design, specialized image processing, and task-specific circuit integration.

The currently demonstrated angle-sensitive pixels have two primary disadvantages: poor quantum efficiency and wavelength sensitivity of the angular response. The two layers of metal interconnect in each pixel used to generate angular sensitivity blocks a significant fraction of incident light from the photodetector, limiting the usefulness of these devices in low-light applications. Additionally, changing the wavelength of incident illumination alters the position of the diffraction patterns used by angle-sensitive pixels and thus influences their observed angular response.

Preliminary work has shown that the sensitivity problem can be overcome using alternative pixel designs which rely on periodic gratings created from the back-end dielectric which modulate the phase, rather than amplitude, of incident light, with more complex photodiode detectors [142]. Although these devices require the post-processing of CMOS chips, the observed improvement in light sensitivity compensates for the additional cost and complexity of manufacturing. Similar post-processing steps can also address wavelength sensitivity, using for example the integrated color filters available in image sensor manufacturing to limit the wavelengths of light seen by individual angle-sensitive pixels. A more exotic approach would combine structures in CMOS dielectric with additional materials whose dispersive properties result in a phase-modulating grating where small changes

in wavelength do not alter the observed diffraction patterns, as in the design of achromatic lenses [143].

Our mathematical framework for understanding angle-sensitive pixels as angular bandpass filters is extremely general and makes no assumptions about the properties of visual scenes. Consequently, the algorithms that we have developed to process the images are agnostic to image statistics, treating an image of a human face, a building, and bandlimited white noise identically. Since typical natural scenes have strong statistical characteristics, tailoring specialized algorithms to take advantage of this knowledge for specific tasks is an obvious path to significant improvement toward simpler, more efficient methods. Along a similar line of reasoning, angle-sensitive pixel arrays to date have chosen a set of pixels whose responses form a complete angular transform basis. Although this is the best general solution, different imaging tasks likely have unique *optimal* choices of angle-sensitive pixel responses as they require distinct classes of information from a visual scene. Identifying and building the "best" pixel arrays for specific imaging problems provides another approach to improving overall system performance.

One of the primary benefits of CMOS manufacturing compatibility is the ability to integrate circuits with angle-sensitive pixel devices. All fabricated chips to date have used this capability to provide conventional, digitally controlled addressing and analog pixel outputs to simplify the hardware necessary for testing the sensors, while the light-field camera included a complete column parallel amplification and digitization chains as a demonstration of a complete digital camera chip using angle-sensitive pixels. Meanwhile, software routines were used to demonstrate relevant imaging tasks such as motion measurement or object localization from captured images recorded directly from the sensors.

In contrast, the most recent angle-sensitive image compression chip represents a

significant departure from previous design choices by integrating circuits expressly designed to take advantage of the specific optical properties of angle-sensitive pixels rather than to provide basic pixel readout functionality. This device represents an initial foray into mixed-domain optoelectronic design which fuses integrated circuits with optical structures for image sensors which integrate higher level image processing functions on chip. Research opportunities lie in generalizing this approach to other image sensors which efficiently integrate on-chip circuits to acquire images that are the result of traditionally what have been software operations, such as edge detection, feature extraction, range mapping, and motion measurement.

This thesis establishes the initial foundation for these and other research directions by demonstrating a new sensor device, the angle-sensitive pixel, and progressing through its integration with circuits and subsequent use in example applications. These structures are CMOS image sensor pixels which are sensitive to the incident angle and the intensity of the light they see, and arrays of these devices capture useful information about 3D visual scenes in a format useful for downstream image processing applications. Angle-sensitive pixels thus provide new capabilities to digital imaging at no additional cost or complexity and furthermore are an example of new design opportunities made possible by the precision lithography available in modern semiconductor manufacturing processes.

REFERENCES

[1] A. Gershun, "The light field," *Journal of Mathematics and Physics*, vol. 18, pp. 51–151, 1939.

[2] E. Adelson and J. Bergen, "The plenoptic function and the elements of early vision," in *Computational Models of Visual Processing*, M. Landy and J. A. Movshon, Eds. Cambridge, MA: The MIT Press, 1991, pp. 3–20.

[3] P. Moon and D. E. Spencer, *The Photic Field*. Cambridge, MA: The MIT Press, 1981.

[4] M. Levoy and P. Hanrahan, "Light field rendering," *Proc. ACM SIGGRAPH*, pp. 31–42, July 1996.

[5] S. Gortler, R. Grzeszczuk, R. Szeliski, and M. Cohen, "The lumigraph," in *Proc. ACM SIGGRAPH*, Jul. 1996, pp. 43–54.

[6] K. S. Shanmugam, F. M. Dickey, and J. A. Green, "An optimal frequency domain filter for edge detection in digital pictures," *IEEE Trans. Pattern Anal. Machine Intell.*, vol. PAMI-1, no. 1, pp. 37–49, jan. 1979.

[7] U.-V. Koc and K. Liu, "DCT-based motion estimation," *IEEE Trans. Image Processing*, vol. 7, no. 7, pp. 948 –965, Jul. 1998.

[8] W. Pennebaker and J. Mitchell, *JPEG: Still Image Data Compression Standard*. Norwell, Massachusetts: Kluwer Academic, 1992.

[9] A. Oppenheim, R. Schafer, and J. Buck, *Discrete-time signal processing*. Upper Saddle River, New Jersey: Prentice Hall, 1999.

[10] T. Cormen, C. Leiserson, R. Rivest, and C. Stein, *Introduction to Algorithms*, 2nd ed. Cambridge, MA: MIT Press, 2001.

[11] J. Pearl, "On coding and filtering stationary signals by discrete Fourier transforms," *IEEE Trans. Inform. Theory*, vol. 19, no. 2, pp. 229– 232, Mar. 1973.

[12] J.-L. Starck, E. Candes, and D. Donoho, "The curvelet transform for image denoising," *IEEE Trans. Image Processing*, vol. 11, no. 6, pp. 670–684, Jun. 2002.

[13] A. Bandyopadhyay, J. Lee, R. Robucci, and P. Hasler, "MATIA: a programmable 80 μw/frame cmos block matrix transform imager architecture," *IEEE J. Solid-State Circuits*, vol. 41, no. 3, pp. 663 –672, Mar. 2006.

[14] A. Nilchi, J. Aziz, and R. Genov, "Focal-plane algorithmically-multiplying CMOS computational image sensor," *IEEE J. Solid-State Circuits*, vol. 44, no. 6, pp. 1829–1839, Jun. 2009.

[15] Y. Nishikawa, S. Kawahito, M. Furuta, and T. Tamura, "A high-speed CMOS image sensor with on-chip parallel image compression circuits," in *Proc. IEEE Custom Integrated Circuits Conf. (CICC)*, Sep. 2007, pp. 833–836.

[16] W. Boyle and G. Smith, "Charge coupled semiconductor devices," *Bell Sys. Tech. J.*, vol. 49, no. 4, pp. 587–593, Apr. 1970.

[17] M. Tompsett, G. Amelio, J. Bertram, W.J., R. Buckley, W. McNamara, J. Mikkelsen, J.C., and D. Sealer, "Charge-coupled imaging devices: Experimental results," *IEEE Trans. Electron Devices*, vol. 18, no. 11, pp. 992–996, Nov. 1971.

[18] P. Dillon, A. Brault, J. Horak, E. Garcia, T. Martin, and W. Light, "Integral color filter arrays for solid state imagers," in *IEEE Int. Electron Devices Meeting (IEDM) Tech. Dig.*, vol. 22, 1976, pp. 400–403.

[19] R. Dyck and G. Weckler, "Integrated arrays of silicon photodetectors for image sensing," *IEEE Trans. Electron Devices*, vol. 15, no. 4, pp. 196–201, Apr. 1968.

[20] G. Weckler, "Operation of p-n junction photodetectors in a photon flux integrating mode," *IEEE J. Solid-State Circuits*, vol. 2, no. 3, pp. 65–73, Sep. 1967.

[21] P. Noble, "Self-scanned silicon image detector arrays," *IEEE Trans. Electron Devices*, vol. 15, no. 4, pp. 202– 209, Apr. 1968.

[22] Y. Ishihara and K. Tanigaki, "A high photosensitive IL-CCD image sensor with monolithic resin lens array," in *IEEE Int. Electron Devices Meeting (IEDM) Tech. Dig.*, vol. 29, Dec. 1983, pp. 497– 500.

[23] Y. Sano, T. Nomura, H. Aoki, S. Terakawa, H. Kodama, T. Aoki, and Y. Hiroshima, "Submicron spaced lens array process technology for a high pho-

tosensitivity CCD image sensor," in *IEEE Int. Electron Devices Meeting (IEDM) Tech. Dig.*, Dec. 1990, pp. 283–286.

[24] R. Nixon, S. Kemeny, B. Pain, C. Staller, and E. Fossum, "256×256 CMOS active pixel sensor camera-on-a-chip," *IEEE J. Solid-State Circuits*, vol. 31, no. 12, pp. 2046–2050, Dec. 1996.

[25] S. Mendis, S. Kemeny, R. Gee, B. Pain, C. Staller, Q. Kim, and E. Fossum, "CMOS active pixel image sensors for highly integrated imaging systems," *IEEE J. Solid-State Circuits*, vol. 32, no. 2, pp. 187–197, Feb. 1997.

[26] J. Nakamura, B. Pain, T. Nomoto, T. Nakamura, and E. Fossum, "On-focal-plane signal processing for current-mode active pixel sensors," *IEEE Trans. Electron Devices*, vol. 44, no. 10, pp. 1747–1758, Oct. 1997.

[27] Z. Zhou, B. Pain, and E. Fossum, "CMOS active pixel sensor with on-chip successive approximation analog-to-digital converter," *IEEE Trans. Electron Devices*, vol. 44, no. 10, pp. 1759–1763, Oct. 1997.

[28] A. Wang, P. Gill, and A. Molnar, "Light field image sensors based on the Talbot effect," *Applied Optics*, vol. 48, no. 31, pp. 5897–5905, Nov. 2009.

[29] ——, "Fluorescent imaging and localization with angle sensitive pixel arrays in standard CMOS," in *Proc. IEEE Sensors Conf.*, Nov. 2010, pp. 1706–1709.

[30] P. Gill, A. Wang, and A. Molnar, "The in-crowd algorithm for fast basis pursuit denoising," *IEEE Trans. Signal Processing*, vol. 59, no. 10, pp. 4595–4605, Oct. 2011.

[31] A. Wang and A. Molnar, "A light-field image sensor in 180 nm CMOS," *IEEE J. Solid-State Circuits*, vol. 47, no. 1, pp. 257–271, Jan. 2012.

[32] ——, "Phase-based 3D optical flow sensors for motion detection," in *Proc. IEEE Sensors Conf.*, Oct. 2011, pp. 683–686.

[33] A. Wang, S. Hemami, and A. Molnar, "Angle-sensitive pixels: a new paradigm for low-power, low-cost 2D and 3D sensing," in *Proc. SPIE Electronic Imaging*, vol. 8288, no. 828805, 2012.

[34] R. Ng, "Fourier slice photography," *ACM Trans. Graph.*, vol. 24, pp. 735–744, Jul. 2005.

[35] H. F. Talbot, "Facts relating to optical science. No. IV," *Philosophical Magazine, S.3*, vol. 9, no. 56, pp. 401–407, 1836.

[36] M. Faraday, "Thoughts on ray vibrations," *Philosophical Magazine, S. 3*, vol. 28, no. 188, pp. 345–350, 1846.

[37] E. Adelson and J. Y. Wang, "Single lens stereo with a plenoptic camera," *IEEE Trans. Pattern Anal. Machine Intell.*, vol. 14, no. 2, pp. 99–106, Feb. 1992.

[38] A. Kubota, K. Aizawa, and T. Chen, "Reconstructing dense light field from array of multifocus images for novel view synthesis," *IEEE Trans. Image Processing*, vol. 16, no. 1, pp. 269–279, Jan. 2007.

[39] B. Wilburn, N. Joshi, V. Vaish, E.-V. Talvala, E. Antunez, A. Barth, A. Adams, M. Horowitz, and M. Levoy, "High performance imaging using large camera arrays," *ACM Trans. Graph.*, vol. 24, pp. 765–776, Jul. 2005.

[40] A. Isaksen, L. McMillan, and S. J. Gortler, "Dynamically reparameterized light fields," in *Proc. ACM SIGGRAPH*, Jul. 2000, pp. 297–306.

[41] A. Veeraraghavan, R. Raskar, A. Agrawal, A. Mohan, and J. Tumblin, "Dappled photography: Mask enhanced cameras for heterodyned light fields and coded aperture refocusing," *ACM Trans. Graph.*, vol. 26, no. 3, pp. 69:1–69:12, Jul. 2007.

[42] K. Fife, A. E. Gamal, and H.-S. P. Wong, "A 3D multi-aperture image sensor architecture," in *Proc. IEEE Custom Integrated Circuits Conf. (CICC)*, Sept. 2006, pp. 281–284.

[43] M. Levoy, R. Ng, A. Adams, M. Footer, and M. Horowitz, "Light field microscopy," in *Proc. ACM SIGGRAPH*, Jul. 2006, pp. 924–934.

[44] L. Rayleigh, "On copying diffraction gratings, and on some phenomena connected therewith," *Philosophical Magazine, S.5*, vol. 11, no. 67, pp. 196–201, 1880.

[45] E. Hiedemann and M. Breazeale, "Secondary interference in the Fresnel zone of gratings," *Journal of the Optical Society of America*, vol. 49, pp. 372–375, 1959.

[46] J. Winthrop and C. Worthington, "Theory of Fresnel images: I. Plane periodic objects in monochromatic light," *Journal of the Optical Society of America*, vol. 55, pp. 373–381, 1965.

[47] W. Montgomery, "Self-imaging objects of infinite aperture," *Journal of the Optical Society of America*, vol. 57, pp. 772–775, 1967.

[48] A. Lohmann and D. Silva, "An interferometer based on the Talbot effect," *Optics Communications*, vol. 2, pp. 413–415, 1971.

[49] J. Ojeda-Castañeda and E. Sicre, "Tunable bandstop filter for binary objects: A self-imaging technique," *Optics Communications*, vol. 47, pp. 183–186, 1983.

[50] J. Lohmann, A.W. andThomas, "Making an array illuminator based on the Talbot effect," *Applied Optics*, vol. 29, pp. 4337–4340, 1990.

[51] P. Chavel and T. Strand, "Range measurement using Talbot diffraction imaging of gratings," *Applied Optics*, vol. 23, pp. 862–871, 1984.

[52] J. Leger and M. Snyder, "Real-time depth measurement and display using Fresnel diffraction and white-light processing," *Applied Optics*, vol. 23, pp. 1655–1670, 1984.

[53] N. H. Salama, D. Patrignani, L. d. Pasquale, and E. E. Sicre, "Wavefront sensor using the Talbot effect," *Optics and Laser Technology*, vol. 31, pp. 269–272, 1999.

[54] C. Siegel, F. Loewenthal, and J. E. Balmer, "A wavefront sensor based on the fractional Talbot effect," *Optics Communications*, vol. 194, no. 4-6, pp. 265–275, Jul. 2001.

[55] H. O. Carmesin and D. Goldbeck, "Depth map by convergent 3D-Talbot-interferometry," *Optik*, vol. 108, pp. 101–116, 1998.

[56] M. Testorf, J. Jahns, N. A. Khilo, and A. M. Goncharenko, "Talbot effect for oblique angle of light propagation," *Optics Communications*, vol. 129, no. 3-4, pp. 167–172, Aug. 1996.

[57] S. Teng, Y. Tan, and C. Cheng, "Quasi-Talbot effect of the high-density grating in near field," *Journal of the Optical Society of America A*, vol. 25, pp. 2945–2951, 2008.

[58] I. Smolyaninov and C. Davis, "Apparent superresolution in near-field optical imaging of periodic gratings," *Optics Letters*, vol. 23, pp. 1346–1347, 1998.

[59] K. Fife, A. E. Gamal, and H.-S. P. Wong, "A 0.5μm pixel frame transfer CCD image sensor in 110nm CMOS," in *IEEE Int. Electron Devices Meeting (IEDM) Dig.*, Dec. 2007, pp. 1003–1006.

[60] M. Chapman, C. Ekstrom, T. Hammond, J. Schmiedmayer, B. E. Tannian, S. Wehinger, and D. E. Pritchard, "Near-field imaging of atom diffraction gratings: The atomic talbot effect," *Physical Review A*, vol. 51, pp. R14–R17, 1995.

[61] S. Teng, L. Liu, J. Zu, Z. Luan, and D. Liu, "Uniform theory of the Talbot effect with partially coherent light illumination," *Journal of the Optical Society of America A*, vol. 20, pp. 1747–1754, 2003.

[62] Y. Lu, C. Zhou, S. Wang, and B. Wang, "Polarization-dependent Talbot effect," *Journal of the Optical Society of America A*, vol. 23, pp. 2154–2160, 2006.

[63] K. Fife, A. El Gamal, and H.-S. P. Wong, "A multi-aperture image sensor with 0.7 μm pixels in 0.11 μm CMOS technology," *IEEE J. Solid-State Circuits*, vol. 43, no. 12, pp. 2990–3005, Dec. 2008.

[64] B. Jang, P. Cao, A. Chevalier, A. Ellington, and A. Hassibi, "A CMOS fluorescent-based biosensor microarray," in *IEEE Int. Solid-State Circuits Conf. (ISSCC) Dig.*, Feb. 2009, pp. 436–437.

[65] J. Singer and C. Plotz, "The latex fixation test." *American Journal of Medicine*, vol. 21, pp. 888–893, 1956.

[66] S. Smole, E. Aronson, A. Durbin, S. Brecher, and R. Arbeit, "Sensitivity and specificity of an improved rapid latex agglutination test for identification of methicillin-sensitive and -resistant Staphylococcus aureus isolates." *Journal of Clinical Microbiology*, vol. 36, no. 4, pp. 1109–1112, Apr. 1998.

[67] C. Riggin, G. Beltz, C. Hung, R. Thorn, and D. Marciani, "Detection of antibodies to human immunodeficiency virus by latex agglutination with recombinant antigen." *Journal of Clinical Microbiology*, vol. 25, no. 9, pp. 1772–1773, Sep. 1987.

[68] A. Wang, P. Gill, and A. Molnar, "Angle sensitive pixels in CMOS for lensless

3D imaging," in *Proc. IEEE Custom Integrated Circuits Conf. (CICC)*, Sep. 2009, pp. 371–374.

[69] M. Lustig, D. Donoho, J. Santos, and J. Pauly, "Compressed sensing MRI," *IEEE Signal Processing Mag.*, vol. 25, no. 2, pp. 72–82, 2008.

[70] U. Gamper, P. Boesiger, and S. Kozerke, "Compressed sensing in dynamic MRI," *Magnetic Resonance in Medicine*, vol. 59, no. 2, pp. 365–373, 2008.

[71] S. Chen, D. Donoho, and M. Saunders, "Atomic decomposition by basis pursuit," *SIAM Review*, vol. 43, no. 1, pp. 129–159, 2001.

[72] R. Tibshirani, "Regression shrinkage and selection via the lasso," *Journal of the Royal Statistical Society. Series B (Methodological)*, vol. 58, no. 1, pp. 267–288, 1996.

[73] P. Ravikumar, G. Raskutti, M. Wainwright, and B. Yu, "Model selection in Gaussian graphical models: High-dimensional consistency of ℓ_1-regularized MLE," *Advances in Neural Information Processing Systems (NIPS)*, vol. 21, pp. 1329–1336, 2008.

[74] J. Bergh and J. Löfström, *Interpolation spaces : an introduction.* Berlin; New York: Springer-Verlag, 1976.

[75] R. Gribonval and M. Nielsen, "Beyond sparsity: Recovering structured representations by minimization and greedy algorithms," *Advances in computational mathematics*, vol. 28, no. 1, pp. 23–41, 2008.

[76] S. Chen and D. Donoho, "Basis pursuit," in *28th Asilomar Conference on Signals, Systems and Computers, 1994*, vol. 1, oct. 1994, pp. 41–44.

[77] S. Becker, J. Bobin, and E. Candès, "NESTA: A fast and accurate first-order method for sparse recovery," *SIAM J. on Imaging Sciences*, vol. 4, no. 1, pp. 1–39, 2009.

[78] J. Wright, Y. Ma, J. Mairal, G. Sapiro, T. Huang, and S. Yan, "Sparse representation for computer vision and pattern recognition," *Proceedings of the IEEE*, vol. 98, no. 6, pp. 1031–1044, 2010.

[79] A. Bruckstein, D. Donoho, and M. Elad, "From sparse solutions of systems of equations to sparse modeling of signals and images," *SIAM Review*, vol. 51, no. 1, pp. 34–81, 2009.

[80] M. Elad and M. Aharon, "Image denoising via sparse and redundant representations over learned dictionaries," *IEEE Trans. Image Processing*, vol. 15, no. 12, pp. 3736–3745, 2006.

[81] Y. Andreopoulos, M. V. D. Schaar, A. Munteanu, J. Barbarien, P. Schelkens, and J. Cornelis, "Complete-to-overcomplete discrete wavelet transforms for scalable video coding with mctf," in *Proc. IEEE Visual Communication and Image Processing*, 2003, pp. 719–731.

[82] B. Olshausen and D. Field, "Sparse coding with an overcomplete basis set: A strategy employed by V1?" *Vision research*, vol. 37, no. 23, pp. 3311–3325, 1997.

[83] ——, "Sparse coding of sensory inputs," *Current opinion in neurobiology*, vol. 14, no. 4, pp. 481–487, 2004.

[84] A. Beck and M. Teboulle, "A fast iterative shrinkage-thresholding algorithm for linear inverse problems," *SIAM J. on Imaging Sciences*, vol. 2, no. 1, pp. 183–202, 2009.

[85] ——, "A fast iterative shrinkage-thresholding algorithm with application to wavelet-based image deblurring," in *Proc. IEEE Intl. Conf. Acoustics, Speech and Signal Processing (ICASSP)*, Apr. 2009, pp. 693–696.

[86] D. Donoho, "Compressed sensing," *IEEE Trans. Inform. Theory*, vol. 52, no. 4, pp. 1289–1306, Apr. 2006.

[87] K. Barthel, H. Cycon, and D. Marpe, "Image denoising using fractal and wavelet-based methods," in *Proc. SPIE*, vol. 5266, 2003, pp. 10–18.

[88] J. Pawley and B. Masters, *Handbook of biological confocal microscopy*. Berlin; New York: Springer-Verlag, 2006.

[89] A. Diaspro, *Confocal and two-photon microscopy: foundations, applications, and advances*. New York: Wiley-Liss, 2002.

[90] D. Needell and J. Tropp, "CoSaMP: Iterative signal recovery from incomplete and inaccurate samples," *Applied and Computational Harmonic Analysis*, vol. 26, no. 3, pp. 301–321, 2009.

[91] D. Malioutov, M. Cetin, and A. Willsky, "Homotopy continuation for sparse

signal representation," in *Proc. IEEE Intl. Conf. Acoustics, Speech and Signal Processing (ICASSP)*, vol. 5, 2005, pp. 733–736.

[92] M. Salman Asif and J. Romberg, "Dynamic updating for ℓ_1 minimization," *IEEE J. Select. Topics Sig. Proc.*, vol. 4, no. 2, pp. 421–434, Apr. 2010.

[93] M. S. Asif. (2009) L1 homotopy. [Online]. Available: \url{http://users.ece.gatech.edu/~sasif/homotopy/index.html}

[94] E. van den Berg and M. P. Friedlander. (2007) SPGL1: A solver for large-scale sparse reconstruction. [Online]. Available: \url{http://www.cs.ubc.ca/labs/scl/spgl1}

[95] ——, "Probing the Pareto frontier for basis pursuit solutions," *SIAM J. Scientific Computing*, vol. 31, no. 2, pp. 890–912, 2008.

[96] S.-J. Kim, K. Koh, M. Lustig, S. Boyd, and D. Gorinevsky, "An interior-point method for large-scale ℓ_1-regularized least squares," *IEEE J. Sel. Topics Sig. Proc.*, vol. 1, no. 4, pp. 606–617, Dec. 2007.

[97] E. Hale, W. Yin, and Y. Zhang, "Fixed-point continuation applied to compressed sensing: implementation and numerical experiments," *J. of Computational Mathematics*, vol. 28, no. 2, pp. 170–194, 2010.

[98] ——. (2008) Fixed-point continuation (FPC) for large-scale image and data processing applications of l1-minimization. [Online]. Available: \url{http://www.caam.rice.edu/~optimization/L1/fpc/}

[99] Z. Wen and W. Yin. FPC AS, A MATLAB Solver for L1-Regularization Problems. [Online]. Available: http://www.caam.rice.edu/~optimization/L1/FPC_AS/

[100] M. Figueiredo, R. Nowak, and S. Wright, "Gradient projection for sparse reconstruction: Application to compressed sensing and other inverse problems," *IEEE J. on Sel. Topics Sig. Proc.*, vol. 1, no. 4, pp. 586–597, 2007.

[101] MathWorks. (2011) Quadratic programming :: Optimization algorithms and examples (optimization toolbox^{TM}). [Online]. Available: http://www.mathworks.com/help/toolbox/optim/ug/brnox7l.html

[102] P. Gill, W. Murray, and M. Wright, *Practical Optimization*. Academic Press, 1981.

[103] A. Wills. (2010) SPM: QPC - Quadratic Programming in C. [Online]. Available: \url{http://sigpromu.org/quadprog/}

[104] J. Tropp and A. Gilbert, "Signal recovery from random measurements via orthogonal matching pursuit," *IEEE Trans. Inform. Theory*, vol. 53, no. 12, pp. 4655–4666, Dec. 2007.

[105] T. Blumensath and M. Davies, "Stagewise weak gradient pursuits," *IEEE Trans. Signal Processing*, vol. 57, no. 11, pp. 4333–4346, Nov. 2009.

[106] B. Efron, T. Hastie, I. Johnstone, and R. Tibshirani, "Least angle regression," *Annals of statistics*, vol. 32, no. 2, pp. 407–451, 2004.

[107] W. Dai and O. Milenkovic, "Subspace pursuit for compressive sensing signal reconstruction," *IEEE Trans. Inform. Theory*, vol. 55, no. 5, pp. 2230–2249, May 2009.

[108] I. Drori and D. Donoho, "Solution of ℓ_1 Minimization Problems by LARS/Homotopy Methods," in *Proc. IEEE Intl. Conf. Acoustics, Speech and Signal Processing (ICASSP)*, vol. 3, 2006, pp. 636–640.

[109] P. Garrigues and L. Ghaoui, "An homotopy algorithm for the Lasso with online observations," *Advances in neural information processing systems*, vol. 21, pp. 489–496, 2009.

[110] A. Wang, P. Gill, and A. Molnar, "An angle-sensitive CMOS imager for single-sensor 3D photography," in *IEEE Int. Solid-State Circuits Conf. (ISSCC) Dig.*, Feb. 2011, pp. 412–414.

[111] C. Koch, J. Oehm, J. Emde, and W. Budde, "Light source position measurement technique applicable in SOI technology," *IEEE J. Solid-State Circuits*, vol. 43, no. 7, pp. 1588–1593, Jul. 2008.

[112] C. Niclass, C. Favi, T. Kluter, M. Gersbach, and E. Charbon, "A 128×128 single-photon image sensor with column-level 10-bit time-to-digital converter array," *IEEE J. Solid-State Circuits*, vol. 43, no. 12, pp. 2977–2989, Dec. 2008.

[113] C. Niclass, C. Favi, T. Kluter, F. Monnier, and E. Charbon, "Single-photon synchronous detection," *IEEE J. Solid-State Circuits*, vol. 44, no. 7, pp. 1977–1989, Jul. 2009.

[114] D. Stoppa, N. Massari, L. Pancheri, M. Malfatti, M. Perenzoni, and L. Gonzo, "A range image sensor based on 10-μm lock-in pixels in 0.18-μm CMOS imaging technology," *IEEE J. Solid-State Circuits*, vol. 46, no. 1, pp. 248–258, Jan. 2011.

[115] R. J. Walker, J. A. Richardson, and R. K. Henderson, "A 128×96 pixel event-driven phase-domain $\Sigma\Delta$-based fully digital 3D camera in 0.13 μm CMOS imaging technology," in *IEEE Int. Solid-State Circuits Conf. (ISSCC) Dig.*, Feb. 2011, pp. 410–412.

[116] S. Mandai, M. Ikeda, and K. Asada, "A 256x256 14k range maps/s 3-D range-finding image sensor using row-parallel embedded binary search," in *IEEE Int. Solid-State Circuits Conf. (ISSCC) Dig.*, Feb. 2010, pp. 404–405.

[117] K. L. Boyer and A. C. Kak, "Color-encoded structured light for rapid active ranging," *IEEE Trans. Pattern Anal. Machine Intell.*, vol. PAMI-9, no. 1, pp. 14–28, Jan. 1987.

[118] R. Philipp and R. Etienne-Cummings, "A 128 × 128 33mW 30frames/s single-chip stereo imager," in *IEEE Int. Solid-State Circuits Conf. (ISSCC) Dig.*, Feb. 2006, pp. 2050–2059.

[119] A. Veeraraghavan, A. Agrawal, R. Raskar, A. Mohan, and J. Tumblin, "Non-refractive modulators for encoding and capturing scene appearance and depth," in *Proc. IEEE Conf. Computer Vision and Pattern Recognition (CVPR)*, Jun. 2008, pp. 1–8.

[120] C.-K. Liang, T.-H. Lin, B.-Y. Wong, C. Liu, and H. H. Chen, "Programmable aperture photography: multiplexed light field acquisition," *ACM Trans. Graph.*, vol. 27, pp. 55:1–55:10, Aug. 2008.

[121] A. Stamper, T. McDevitt, and S. Luce, "Sub-0.25-micron interconnection scaling: damascene copper versus subtractive aluminum," in *Proc. IEEE Adv. Semiconductor Manufacturing Conference*, Sep. 1998, pp. 337–346.

[122] I. Ahmed, J. Mulder, and D. Johns, "A low-power capacitive charge pump based pipelined ADC," *IEEE J. Solid-State Circuits*, vol. 45, no. 5, pp. 1016–1027, May 2010.

[123] R. Wood, "On a remarkable case of uneven distribution of light in a diffraction grating spectrum," *Proceedings of the Physical Society of London*, vol. 18, pp. 269–275, 1902.

[124] L. Rayleigh, "Note on the remarkable case of diffraction spectra described by Prof. Wood," *Philosophical Magazine, S.6*, vol. 14, no. 79, pp. 60–65, 1907.

[125] T. W. Ebbesen, H. Lezec, H. Ghaemi, T. Thio, and P. Wolff, "Extraordinary optical transmission through sub-wavelength hole arrays," *Nature*, vol. 391, pp. 667–669, Feb. 1998.

[126] L. Martín-Moreno, F. J. García-Vidal, H. J. Lezec, K. M. Pellerin, T. Thio, J. B. Pendry, and T. W. Ebbesen, "Theory of extraordinary optical transmission through subwavelength hole arrays," *Phys. Rev. Lett.*, vol. 86, no. 6, pp. 1114–1117, Feb. 2001.

[127] D. Gabor, "Theory of communication. part 1: The analysis of information," *Journal of the IEEE, Part III: Radio and Communication Engineering*, vol. 93, no. 26, pp. 429–441, Nov. 1946.

[128] J. Daugman, "Complete discrete 2-D Gabor transforms by neural networks for image analysis and compression," *IEEE Trans. Acoust., Speech, Signal Processing*, vol. 36, no. 7, pp. 1169–1179, Jul. 1988.

[129] R. E. Jacobsen, S. F. Ray, G. G. Attridge, and N. R. Axford, *The Manual of Photography*, 9th ed. Elsevier Science, 2000.

[130] P. Gill, C. Lee, D. Lee, A. Wang, and A. Molnar, "A microscale camera using direct fourier-domain scene capture," *Optics Letters*, vol. 36, no. 15, pp. 2949–2951, 2011.

[131] R. Bracewell, *The Hartley Transform.* Oxford Univ. Press, 1986.

[132] R. Millane, "Analytic properties of the Hartley transform and their implications," *Proc. of the IEEE*, vol. 82, no. 3, pp. 413–428, 1994.

[133] J. Gibson, *The perception of the visual world.* Houghton Mifflin, 1950.

[134] B. K. Horn and B. G. Schunck, "Determining optical flow," *Artificial Intelligence*, vol. 17, pp. 185–203, 1981.

[135] S. Mehta and R. Etienne-Cummings, "A simplified normal optical flow measurement CMOS camera," *IEEE Trans. Circuits Syst. I*, vol. 53, no. 6, pp. 1223–1234, Jun. 2006.

[136] D. J. Fleet and A. D. Jepson, "Computation of component image velocity from local phase information," *Int. J. Comp. Vision*, vol. 5, pp. 77–104, 1990.

[137] T. Gautama and M. V. Hulle, "A phase-based approach to the estimation of the optical flow field using spatial filtering," *IEEE Trans. Neural Networks*, vol. 13, no. 5, pp. 1127 – 1136, Sep. 2002.

[138] D. J. Fleet and A. D. Jepson, "Stability of phase information," *IEEE Trans. Pattern Anal. Machine Intell.*, vol. 15, no. 12, pp. 1253–1268, Dec. 1993.

[139] J. Touryan, G. Felsen, and Y. Dan, "Spatial structure of complex cell receptive fields measured with natural images," *Neuron*, vol. 45, no. 5, pp. 781–791, Mar. 2006.

[140] G. Sullivan, "Efficient scalar quantization of exponential and Laplacian random variables," *IEEE Trans. Inform. Theory*, vol. 42, no. 5, pp. 1365–1374, Sep. 1996.

[141] G. Burton and I. Moorehead, "Color and spatial structure in natural scenes," *Applied Optics*, vol. 26, no. 1, pp. 157–70, 1987.

[142] S. Sivaramakrishnan, A. Wang, P. Gill, and A. Molnar, "Enhanced angle sensitive pixels for light field imaging," in *IEEE Int. Electron Devices Meeting (IEDM) Tech. Dig.*, Dec. 2011, pp. 8.6.1–8.6.4.

[143] M. Herzberger and N. R. McClure, "The design of superachromatic lenses," *Appl. Opt.*, vol. 2, no. 6, pp. 553–560, Jun 1963.